ABSTRACT

Title of Dissertation: Physics and Modelling of
Compressible Turbulent Boundary Layer
Han Ju Lee
Doctor of Philosophy, 2023

Dissertation Directed by: Professor M. Pino Martín
Department of Aerospace Engineering

Key findings from a research study that focuses on understanding the effect of Mach number, Reynolds number and wall temperature on compressible turbulent boundary layers (CTBL) in the hypersonic regime are presented in this dissertation. The study utilizes a comprehensive CTBL database developed using an in-house direct numerical simulation (DNS) code at the CRoCCo laboratory. The database encompasses a range of semi-local Reynolds numbers (800 to 34,000) and Mach numbers up to 12, incorporating wall-cooling.

The effects of density and viscosity fluctuations on the total stress balance are identified and used to create a new mean velocity transformation for compressible boundary layers. The role, significance and physical mechanisms connecting density and viscosity fluctuations to the momentum balance and to the viscous, turbulent and total stresses are presented, allowing the creation of generalized formulations. We identify the significant properties that thus-far have been neglected in the derivation of velocity transformations: (1) the Mach-invariance of the near-wall momentum balance for the generalized total stress, and (2) the Mach-invariance of

the relative contributions from the generalized viscous and Reynolds stresses to the total stress. The proposed velocity transformation integrates both properties into a single transformation equation and successfully demonstrates a collapsing of all currently considered compressible cases onto the incompressible law of the wall, within the bounds of reported slope and intercept for incompressible data. Based on the physics embedded in the two scaling properties, the success of the newly proposed transformation is attributed to considering the effects of the viscous stress and turbulent stresses as well as mean and fluctuating density viscosity in a single transformation form.

The Reynolds number trends of large turbulent structures in compressible turbulent boundary layers are investigated using the pre-multiplied energy spectra based on the density corrected fluctuating streamwise velocity signal. Results demonstrate the existence of friction as well as semi-local Reynolds number trend associated with large-scale structures, similar to trends observable in incompressible turbulent boundary layers (ITBL). In particular, the behavior of turbulence in the inner layer is seen to exhibit dependence based on both definitions of Reynolds numbers. On the contrary, the strength of large turbulent structures is seen to be only dependent on friction Reynolds number. This result directly contrasts with the observation of the near-wall turbulent intensity peak increasing with semi-local Reynolds number. The discrepancy is mended with a suggestion that the large turbulent scales in the log layer of which the strength increases with friction Reynolds number, are modified through the changes in local fluid properties such that the scale interaction near the wall increases as semi-local Reynolds number. In another words, closer to the wall, the CTBL flow behaves like a semi-local Reynolds number flow, while closer to the freestream, it behaves like a friction Reynolds number flow. Furthermore, the present study examines the Reynolds number dependence of the length scale between small and large

turbulent scales. The analysis highlights the inadequacy of using a univariable wavelength based on viscous, semi-local or outer length scales to differentiate small and large scales. Based on this, the use of Reynolds number-dependent length scales is recommended. Overall, the study provides valuable insights into the Reynolds number trends of large turbulent structures in CTBL, emphasizing the influence of both semi-local Reynolds number and friction Reynolds number on turbulence characteristics.

Physics and Modelling of Compressible Turbulent Boundary Layer

by

Han Ju Lee

Dissertation submitted to the Faculty of the Graduate School of the
University of Maryland, College Park in partial fulfillment
of the requirements for the degree of
Doctor of Philosophy
2023

Research Advisors:
Professor M. Pino Martín, PhD Advisor
Defense Committee:
Professor M. Pino Martín, Chair
Professor James Baeder, Co-Chair
Professor Christopher Cadou
Professor Maria Cameron
Professor Ken Yu

Dedication

To Chang Lyoul Lee and Kyoung Sook Kim for their love and prayers

Acknowledgments

Completing this dissertation would not have been possible without the invaluable support, guidance, and encouragement of numerous individuals who have played a vital role in my academic journey. I take this opportunity to express my sincere gratitude and appreciation to each of them.

Foremost, I extend my deepest gratitude to my esteemed advisor, Dr. M. Pino Martín. Your expertise, mentorship, and patience have been instrumental in shaping the direction of this research. Your insightful feedback and unwavering belief in my abilities have inspired me to strive for excellence.

I am equally grateful to my co-advisor, Dr. Owen J.H. Williams, for his valuable contributions and expert advice throughout this project. Your insightful perspectives and constructive criticism have been essential in refining the quality of this dissertation.

I would like to extend a warm thank you to my dear colleagues, Justin Shafner, Vishal Bhagwandin, and Clara Helm. Our collaborative discussions and mutual support have made the academic journey more rewarding and enjoyable. Your camaraderie has been a constant source of motivation.

To my friends who have been with me through thick and thin, I am grateful for your presence in my life. Your unwavering friendship and encouragement have kept me grounded and motivated, even during the most challenging times. Your belief in my abilities has meant the world to me.

To my beloved girlfriend, Minsun Kim, I cannot thank you enough for your love, understanding, and unwavering support. Your presence in my life has been a source of strength and inspiration. Your encouragement and belief in my capabilities have pushed me to surpass my limits, and I am forever grateful for your love.

I am indebted to my mom and dad for their unconditional love, constant encouragement, and sacrifices to provide me with the best possible opportunities. Your belief in my potential has been the driving force behind my achievements, and I owe my success to your unending support.

To all the individuals who have contributed to my academic journey in various ways, whether through intellectual discussions, emotional support, or even a simple word of encouragement, I extend my heartfelt thanks. Your contributions, no matter how small, have made a significant impact on my growth as a scholar and as a person.

With profound appreciation and humility, I acknowledge the invaluable contributions of everyone mentioned here and countless others who have been a part of my journey. Thank you for being my pillars of strength and for making this accomplishment possible.

July 2023,

Han Ju Lee

Table of Contents

Dedication ii

Acknowledgements iii

Table of Contents v

List of Tables vii

List of Figures viii

List of Abbreviations x

Chapter 1: Introduction 1
- 1.1 What is ZPG-CTBL? . . . 3
- 1.2 Why Study ZPG-CTBL: Wall-Modelled LES . . . 6
- 1.3 Scope of Current Work . . . 8

Chapter 2: Theory of Turbulent Boundary Layer 9
- 2.1 Morkovin's Hypothesis & Strong Reynolds Analogy . . . 9
- 2.2 Wall Bounded Mean Flow . . . 15
  - 2.2.1 Law of the Wall . . . 15
  - 2.2.2 Mean Velocity Transformations . . . 16
- 2.3 Wall Bounded Turbulence . . . 19
  - 2.3.1 Attached Eddy Hypothesis . . . 19
  - 2.3.2 Turbulent Structures . . . 23

Chapter 3: Simulation Details and Data Acquisition 29
- 3.1 Direct Numerical Simulation . . . 29
  - 3.1.1 Governing Equation . . . 30
  - 3.1.2 Numerical Methods . . . 31
- 3.2 Compressible Turbulent Boundary Layer Database . . . 35
  - 3.2.1 Flow Conditions . . . 35
  - 3.2.2 Computational domain and simulation set-up . . . 37

Chapter 4: Generalized Mean Velocity Transformation 42
- 4.1 Motivation . . . 42
- 4.2 Density and Viscosity Fluctuations in Compressible Boundary Layers . . . 45

4.2.1 Breakdown of the Classical Momentum Balance . . . 45
4.2.2 The Role and Mechanism of Density and Viscosity Fluctuations . . . 52
4.2.3 Generalized Favre-Averaged Momentum Balance Equation . . . 55
4.3 Total Stress Based Velocity Transformations . . . 58
4.4 Proposed new total stress-based transformation . . . 65
4.5 Discussion of Results . . . 68
4.6 Summary . . . 72

Chapter 5: Reynolds Number Trends in Large Turbulent Structures 75
5.1 Background . . . 75
5.2 Data Synthesis: Pre-multiplied Energy Spectra . . . 79
5.3 Preliminary Observation . . . 83
5.4 Large Turbulent Structures and Reynolds Number Trend . . . 89
5.4.1 Inner Length Scale . . . 90
5.4.2 Outer Length Scale . . . 94
5.4.3 Turbulent Intensity in Large Turbulent Structures . . . 96
5.5 Implication of Reynolds Number Trend . . . 97
5.5.1 The Role of Reynolds Numbers in the Inner Layer . . . 97
5.5.2 Length Scales Between Small Scale and Large Scale . . . 104
5.6 Summary . . . 107

Chapter 6: Conclusions 110
6.1 Key Results & Contributions . . . 110
6.2 Future Investigations . . . 113

Appendix A: Derivation of Thin Shear Layer Momentum Equation 114
A.1 Reynolds-Averaged TSL Equation with density fluctuation . . . 114
A.2 Favre-Averaged TSL Equation with density fluctuation . . . 115

Appendix B: Pre-multiplied Spectra 116

Appendix C: Parametric Study on Cut-off Length Scale 120

Bibliography 122

List of Tables

3.1 Boundary layer edge and wall parameters of DNS database. [1] 40
3.2 Computational domain size and grid resolution for the DNS data 40
3.3 Incompressible Channel Flow DNS Database 41
3.4 Selected parameters from compressible turbulent boundary layer DNS Database from [1, 2] 41

List of Figures

2.1 Morkovin Scaled Turbulent Kinetic Energy [2] . . . 11
2.2 Comparison of Strong Reynolds Analogy [3] . . . 14
2.3 Performance of Van Driest transformation [4] . . . 17
2.4 Performance of GFM transformation [4] . . . 18
2.5 Λ-shaped hairpin vortex [5] . . . 21
2.6 Wave number regions with different scaling [6] . . . 22
2.7 Generic representation of vortex packets [7] . . . 25
2.8 Quadrant Analysis with conventional names of bursting events [8] . . . 26

3.1 Candidate stencils S_k for the numerical flux $\hat{f}^{+}_{i+1/2}$ when r = 3 for WENO-BO method [9] . . . 33
3.2 Performance of bandwidth resolving characteristics of WENO-BO method compared to WENO-JS and 6^{th} order Padé scheme [9] . . . 34
3.3 Generic computation domain with outlet (recaling) yz plane . . . 37
3.4 Two point correlation coefficients of M5T1 and M12T5 . . . 39

4.1 Non-dimensionalized Reynolds averaged stresses . . . 46
4.2 Comparison of stresses pertaining to thermodynamic property fluctuations/Comparison of the magnitudes of the TKE terms . . . 50
4.3 Thin shear layer convection term analysis . . . 51
4.4 Comparison of Reynolds averaged stress terms pertaining to density fluctuation, viscosity fluctuation and total stress . . . 53
4.5 Comparison of Favre averaged stress terms pertaining to viscosity fluctuation, viscous stress, turbulent stress and total stress . . . 57
4.6 Comparison of GFM transformation, log layer intercept and slope using CTBL DNS data in table 3.1 . . . 59
4.7 Pre-multiplied mean shear, β_{GFM}, based on GFM transformation versus semi-local wall normal coordinate . . . 60
4.8 The ratio of the TKE production (P) and the viscous dissipation (ϵ) versus semi-local wall normal coordinate, z^* . . . 63
4.9 Proportionally accurate generalized total stress . . . 67
4.10 Comparison of the presently-proposed velocity transformation, intercept and slope of the log layer . . . 69

4.11 Pre-multiplied mean shear, β_G,based on the present mean velocity transformation versus semi-local wall normal coordinate, z^* 70

5.1 Selected contour maps of pre-multiplied energy spectra using δ scale axis normalization 81
5.2 Generic pre-multiplied spectra used by the peak search algorithm 82
5.3 Comparison of pre-multiplied energy spectra contour maps based on Re^* variation 85
5.4 Comparison of pre-multiplied energy spectra contour maps based on Re_τ variation 86
5.5 Comparison of streamwise turbulent intensity based on Re^* & Re_τ variation . . . 88
5.6 Pre-multiplied energy spectra contour map of M10T3 with semi-local length scale axis normalization 89
5.7 Wall normal location of LSP and VLSP in inner length scales 92
5.8 Wavenumber of LSP and VLSP in inner length scales 93
5.9 Wall normal location and wavenumber normalized by outer length scale 95
5.10 Pre-multiplied spectra at wall normal location of LSP & VLSP 96
5.11 Generic turbulent intensity representation of Reynolds number influence in determining large turbulent structures 100
5.12 Normalized streamwise turbulent intensity and generalized mean velocity transformation 101
5.13 Normalized streamwise turbulent intensity and modified Samie equation 103
5.14 Relative contribution of large turbulent structures based on different length scale cut-offs 105

B.1 Pre-multiplied energy spectra based on $\rho u''u''/\tau_w$ velocity signal plotted against wall normal position, z, in x-axis and streamwise wavelength, λ_x, in y-axis. Wall normal position and wavelength are normalized by the outer scale, δ. (A) M3T5 (B) M5T5 (C) M7T5 (D) M10T3 116
B.2 Pre-multiplied energy spectra based on $\rho u''u''/\tau_w$ velocity signal plotted against wall normal position, z, in x-axis and streamwise wavelength, λ_x, in y-axis. Wall normal position and wavelength are normalized by the outer scale, δ. (A) M12T5 (B) M2H (C) M6H 117
B.3 Pre-multiplied energy spectra based on $\rho u''u''/\tau_w$ velocity signal plotted against wall normal position, z, in x-axis and streamwise wavelength, λ_x, in y-axis. Wall normal position and wavelength are normalized by the viscous length scale. (A) M3T5 (B) M5T5 (C) M7T5 (D) M10T3 118
B.4 Pre-multiplied energy spectra based on $\rho u''u''/\tau_w$ velocity signal plotted against wall normal position, z, in x-axis and streamwise wavelength, λ_x, in y-axis. Wall normal position and wavelength are normalized by the viscous length scale. (A) M12T5 (B) M2H (C) M6H 119

C.1 Relative contribution of large turbulent structures using wavelength cut-off based on outer scaling at (A) λ_x/δ = 0.5 (B)λ_x/δ = 2.0 120
C.2 Relative contribution of large turbulent structures using wavelength cut-off based on outer scaling at (A) λ_x^+ = 500 (B) λ_x^+ = 1500 120
C.3 Relative contribution of large turbulent structures using wavelength cut-off based on outer scaling at (A) λ_x^* = 1500 (B) λ_x^* = 2500 121

List of Abbreviation

Acronym

AEH	Attached Eddy Hypothesis
CTBL	Compressible Turbulent Boundary Layer
ITBL	Incompressible Turbulent Boundary Layer
ZPG-CTBL	Zero-Pressure Gradient Compressible Turbulent Boundary Layer
GSRA	Generalized Strong Reynolds Analogy
HVS	Hairpin Vortex Signature
VITA	Variable Interval Time Averaging
DNS	Direct Numerical Simulation
LES	Large Eddy Simulation
SRA	Strong Reynolds Analogy
RANS	Reynolds Averaged Numerical Simulations
WMLES	Wall Modelled Large Eddy Simulation
LSM	Large Scale Motion
VLSM	Very Large Scale Motion
SS	Superstructures
LSP	Large Scale Motion Spectral Peak
VLSP	Very Large Scale Motion Spectral Peak
ISP	Near-wall Inner Spectral Peak
MVT	Mean Velocity Transformation
PIV	Particle Image Velocimetry
TSL	Thin Shear Layer
RK3	3^{rd} Order Runge-Kutta Time Marching Method
WENO-BO	Bandwidth Optimized Weighted Essentially Non Oscillatory Method
WENO-JS	Weighted Essentially Non Oscillatory Method by Jiang and Shu
VD	Van-Driest Mean Velocity Transformation
TL	Trettel-Larsson Mean Velocity Transformation
GFM	Griffin-Fu-Moin Mean Velocity Transformation
PSD	Pre-multiplied Power Spectra Energy Density

Variables & Symbols

t	time(s)
ρ	density(kg/m^3)
k	Turbulent Kinetic Energy (J/kg)
k	Thermal Conductivity(W/m K)
u_τ	friction velocity (m/s)
δ	Boundary Layer Thickness Based on Velocity (m)
u,v,w	Streamwise, Spanwise, Wall-normal Velocity (m/s)
x,y,z	Streamwise, Spanwise, Wall-normal Coordinate (m)
μ	Dynamic Viscosity (kg/m s)
T	Temperature (K)
p	Pressure (Pa)
P	Production of Turbulent Kinetic Energy
e	Total Energy per unit Mass (J/kg)
ϵ	Viscous Dissipation of Turbulent Kinetic Energy
Φ	Power Spectral Density
γ	Ratio of Specific Heat
M	Mach Number
Pr	Prandtl Number
C_p	Constant Pressure Specific Heat
C_v	Constant Volume Specific Heat
C_h	Heat Transfer Coefficient
C_f	Skin Friction Coefficient
Re_τ	Friction Reynolds Number
Re^*	Semi-local Reynolds Number
k	wavenumber
κ	von Kármán Constant
a	Speed of Sound (m/s)
f	frequency (Hz)
f	generic variable
τ	Momentum Stress
σ_{ij}	Shear Stress Tensor
S_{ij}	Strain Rate Tensor
S	Mean Shear
ζ	Thermodynamic Property Fluctuation Stress
q	Heat Flux (W/m^2)
q	Flux Approximation on WENO Stencils
θ	Momentum Thickness (m)

Subscripts

w	Wall
e	Boundary Layer Edge

Superscript

+	Normalized by Viscous Length Scaling
*	Normalized by Semi-Local Scaling
$'$	Fluctuation Based on Reynolds Averaging
$''$	Fluctuation Based on Favre Averaging
$\overline{f}$	Mean Value Based on Reynolds Averaging
$\tilde{f}$	Mean Value Based on Favre Averaging

Chapter 1: Introduction

The study of compressible turbulent boundary layers (CTBL) is a critical component of the broader field of compressible flow, which refers to fluid flow where thermodynamic properties such as density or viscosity are variables rather than constants as in the case in incompressible flow. This variation in thermodynamic properties occurs because of the high velocity in compressible flow, which is high enough to allow for energy transfer from kinetic energy to thermal energy through viscous dissipation at the wall. Furthermore, the increased dissipation of the kinetic energy at the wall can be so significant that the surface cooling might be a necessary. Thus, wall heat transfer is also a key factor to consider in CTBL. Another key trait of compressible flows is the shock waves which involve large flow property gradients across a short spatial span. These phenomena often occur in compressible flow due to the high velocity field that exceeds the speed of sound. These two distinctive characteristics have posed many engineering problems in the design of high-speed vehicles.

Despite the challenge, our understanding of compressible flow in the supersonic regime, where a Mach number is greater than 2 but less than 5 and high-temperature phenomena might not be significant, has greatly increased with continued research efforts in the last few decades and has led to the development of many sophisticated supersonic vehicles that have brought much utility both in the civilian and military space. However, although supersonic and hypersonic flow

might both be considered as the compressible flow, our knowledge in the supersonic regime does not translate directly to the hypersonic regime where the freestream Mach number is greater than 5 and thermodynamic effect as well as real gas effects become important. Therefore, a deeper understanding of compressible flow in the hypersonic regime is needed to develop hypersonic vehicles with similar maneuverability and stability as existing supersonic vehicles. With much of national interest in the development of a hypersonic vehicle, there has been a resurgence of research interest in understanding compressible flow in the hypersonic regime to develop hypersonic vehicles.

An aspect of study within the domain of compressible flow in the hypersonic regime is the investigation of compressible turbulent boundary layers. The focus of this area of research is to understand the characteristics of compressible turbulent flow confined by a wall or solid surface. The presence of a solid surface near hypersonic freestream flow gives rise to interesting phenomena, including zero pressure-gradient compressible turbulent boundary layers, shock-turbulent boundary layer interaction, and three-dimensional compressible turbulent boundary layer effect. Given that compressible turbulent boundary layers occur in extreme proximity to a physical wall and has a direct influence on the flow parameters important to the design of a hypersonic vehicle, it is essential to understand these research subjects to advance our ability to improve the flight capabilities of hypersonic vehicles. While the aforementioned phenomena are not exhaustive of all possible subjects under the study of compressible turbulent boundary layers, they serve as a starting point for the different research performed in this field. In this study, zero pressure gradient compressible turbulent boundary layer is extensively reviewed and investigated. The real gas effects, while important, are not considered in this study. In the rest of this chapter, a brief introduction as well as application of zero pressure gradient compressible

turbulent boundary layer (ZPG-CTBL) will be provided.

1.1 What is ZPG-CTBL?

A zero pressure gradient compressible turbulent boundary layer is compressible turbulent flow over a simple flat plate. With this configuration, the effect of pressure gradients in all directions becomes negligible and allows us to isolate and examine the effect of a wall on a moving fluid at hypersonic speeds. For this reason, CTBL is well understood and serves as a canonical case that describes the nature of the wall bounded compressible turbulence in its simplest form. Even with simplistic flow description, the energy exchange between the kinetic and thermal energy results in variable thermodynamic properties across the boundary layer and introduces complexities that need to be investigated to bring over understanding of CTBL to the similar level we have achieved for incompressible turbulent boundary layers (ITBL). To bridge this gap between CTBL and ITBL, one of the widely used theories to analyze CTBL is Morkovin's hypothesis. Morkovin suggested "that for moderate Mach numbers, the essential dynamics of wall-bounded shear flows will follow the incompressible pattern." [10] A following interpretation of this hypothesis by Bradshaw [11] is that within the limitation of small density fluctuation, it may be possible to correctly account for the variation of thermodynamic properties in CTBL and restore the flow statistics reported in ITBL. The current dissertation utilizes and examines the nature and the limitation of Morkovin's hypothesis in its role of analyzing CTBL flow statistics.

Much of the research in CTBL is to understand the important physics such as compressibility effects that affect the mean and turbulence profiles in CTBL. This is because a better understanding

of the physics leads to a more accurate prediction of the flow quantities and valuable corrections for ground and in-flight experiments. In particular, it is possible to develop a mean velocity transformation and a turbulence prediction model for CTBL that are generalizable to different wall and freestream conditions based on the important physics at play. Also, an investigation of these topics provides an important stepping stone that leads to the wall-modelled large eddy simulation (WMLES) which is regarded as a more accurate replacement of Reynolds Averaged Navier-Stokes (RANS) models often used in the flow simulation of a full-scale engineering applications, and more recently to guide experiments and test in the ground and in flight.

In the analysis of mean properties in CTBL, the mean velocity and the mean temperature are regarded as important variables to predict. In ITBL, the mean velocity profile is relatively well known and modelled using Law of the wall which characterizes the boundary layer in three distinct layers: the log layer, the viscous layer, and the buffer layer. In the log layer, the Reynolds stress dominates the velocity profile; In the viscous layer, the viscous stress decelerates the flow velocity to zero; In the buffer layer, stresses from viscosity and turbulence combine to account for the deceleration of the flow.

The law of the wall has been shown to exhibit a high degree of self-similarity and universality in ITBL at varying Reynolds numbers. This observation combined with hypothesis by Morkovin has led researchers to investigate the possible form of law of the wall for CTBL as a mean velocity transformation. Since then, while not entirely generalizable to different wall and freestream conditions, several mean velocity transformations [4, 12, 13] have been proposed to transform the mean velocity profile in CTBL to follow incompressible law of the wall. Such a transformation would not only support the Morkovin's hypothesis but also provide a simple analytic form which can be used to profile a mean velocity in a wall model.

The prediction of the mean temperature on the other hand is addressed by utilizing Strong Reynolds Analogy (SRA) which derives a relationship between the mean velocity profile and the mean temperature profile based on Morkovin's hypothesis and a few other assumptions which are discussed further in section 2. However, because of the unrealistic assumptions that were used to derive SRA, its use in the prediction of CTBL has been shown to be limited. Therefore, many researchers [3,14–17] have long worked on improving SRA and quantifying a temperature-velocity relationship. Different relationships have since been proposed starting with Crocco-Busemann relationship [14, 15] Walz's equation [18] and more recently proposed generalized Reynolds Analogy [3].

In the analysis of CTBL, it is important to consider not only mean quantities but also fluctuating quantities that represent turbulence. Turbulence prediction is an active area of research both in ITBL and CTBL. A prevailing theory that has enabled a near-wall turbulence prediction is the attached eddy hypothesis by Townsend [19]. He theorized that eddies are attached to the wall and grow in proportion with the distance from the wall, therefore closely linking the analysis of CTBL scale interactions. These attached large turbulent structures are shown to be responsible for a significant portion of the turbulent kinetic energy in the boundary layer and to modulate the near-wall turbulence. Understanding the behavior of these large structures is important in our ability to predict turbulence in boundary layers. Combining Morkovin's hypothesis and attached eddy hypothesis, studies of CTBL have focused on identifying comparable large-scale structures and their characteristics based on density scaled turbulence signals. Several studies have confirmed that similar large turbulent structures also exist in CTBL [2,20–24] with comparable structural characteristics as reported for ITBL. More details on the large scale structures discussed above are provided in chapter 2.

1.2 Why Study ZPG-CTBL: Wall-Modelled LES

Currently, RANS is the preferred simulation method over LES for exploring this design parameter space in any full-scale engineering design process despite the fact that LES provides a more accurate solution by resolving all the large energy containing eddies. Primary reason for this choice is that the grid requirement and, thus, the computational cost for RANS grow in proportion with largest characteristic length scales such as a diameter for pipes or a chord length for airfoils. On the other hand, LES scales with the three halfs power of the friction Reynolds number, $Re_\tau^{3/2}$, which is the ratio between the largest scale and the smallest scale that exists in the boundary layer. As one can imagine, this grid requirement for LES becomes increasingly prohibitive in high Reynolds number simulation which is the case in full-scale engineering design. However, RANS suffers from its inaccuracy particularly in non-equilibrium flows due to representing Reynolds stress (turbulence) with turbulence models. To reconcile this dilemma between RANS and LES, WMLES, which models the near-wall region while using the conventional LES elsewhere, has been suggested. Since the near-wall region is the main region where the grid size requirement grows with the friction Reynolds number, WMLES [25–27] provides an attractive approach by mitigating the disadvantages of both RANS and LES.

As the name suggests, WMLES requires an accurate description of flow statistics in the near-wall region. That is, an accurate wall model is required for WMLES. Different methodologies of approximating the near-wall region and merging the solution with LES have been suggested including hybrid LES/RANS approaches and wall stress models. Instead of using a discrete wall model, the hybrid LES/RANS model solves the RANS turbulence closure models in the near wall region with upper boundary condition (interface between LES zone) determined by the solution

from LES. On the other hand, LES with wall stress model approach solves LES all the way down to the wall where a wall model is fed with flow statistics from LES in the log layer and, in return, provides an accurate wall shear stress boundary condition at the wall for LES. This way, an accurate LES solution is ensured while keeping the grid spacing is kept large enough to retain the computational efficiency. The wall shear stress LES approach would benefit the most from an increased accuracy of the wall model. Moreover, its performance in the prediction of complex configurations and non-equilibrium effects would linearly grow with a more accurate wall model, necessitating studies of an accurate wall model under various wall/freestream conditions.

With advancement of WMLES, one of the areas in addition to non-equilibrium flow that would benefit from a more accurate flow prediction is turbulent mixing. Turbulent mixing is important in combustion process especially in supersonic combustor which is a vital component in the development of hypersonic vehicle. In particular, stabilization of a flame in supersonic flow conditions is challenging due to a short residence time of fluid particle, preventing the fuel from reacting with the oxidizer. Since WMLES resolves the turbulent energy transport, the mixing process between the fuel and the oxidizer can be predicted more accurately. Moreover, another key physics to predict in order to stabilize a flame is the near-wall chemical kinetics. Due to the sensitivity of chemical kinetics to temperature, accurately capturing the near wall viscous heating coupled with chemical kinetics is important. An improvement of WMLES will enable to reliably examine such physics in a computationally efficient manner and explore the parametric space in the design of supersonic combustor among many other applications.

1.3 Scope of Current Work

The present dissertation seeks to investigate physical dynamics and models of compressible turbulent boundary layer in the hypersonic flow regime. While it is not necessary to read the manuscript in the order presented, readers who are interested in a brief theoretical review/background of CTBL are recommended to proceed to Chapter 2. The first part of this study included in Chapter 3 presents a CTBL dataset that is developed using an in-house CRoCCo code as well as details of the numerical schemes used in the code. The dataset includes CTBL cases with Mach number ranging from 3 to 12 and wall cooling ranging from an adiabatic wall to highly cooled wall. In Chapter 4, several compressibility effects are newly discovered and analyzed using thin shear layer momentum equations based on the CTBL dataset presented in Chapter 3. According to the physics presented, a new mean velocity transformation model is presented and shown to perform well under a wide range of wall and freestream conditions that are relevant to hypersonic CTBL. Finally, Chapter 5 discusses the Reynolds number dependent behavior of the large scale motions in the logarithmic layer of CTBL to examine several ramifications of the Reynolds number dependence of large scale motions from the perspective of near-wall turbulent modelling.

Chapter 2: Theory of Turbulent Boundary Layer

This section provides general overview of important theories and models that are being used or examined in the study of CTBL. While it is not the goal of this section to provide complete review of all the topics pertinent to CTBL, it provides details of research topics and references relevant to the present dissertation that may serve as a starting point for the readers who are interested in performing studies in CTBL.

2.1 Morkovin's Hypothesis & Strong Reynolds Analogy

Bradshaw's interpretation [11] of Morkovin's hypothesis [10] laid a foundational theory that connects incompressible and compressible boundary layers. It hypothesized that the effect of compressibility in CTBL when the thermodynamic property fluctuation is not significant does not change the essential turbulent time/length scale from that of ITBL. In addition to this hypothesis, assumptions of constant total stress in the near wall region, equivalence of turbulent kinetic energy production and dissipation and similarity of turbulent length scale by using either the inner unit scale or external length scale makes it possible to derive a scaling law suitable for velocity fluctuation and turbulent kinetic energy for CTBL shown in Eq 2.1.

$$\frac{\overline{\rho}k}{\rho_w u_\tau^2} = f(y/\delta, Re_c) \tag{2.1}$$

where $\rho, k, u_\tau, \delta, Re_c$ are density, turbulent kinetic energy, frictional velocity, boundary layer thickness and characteristic Reynolds number, respectively. This density correction also introduces a local friction velocity, $u^* = \sqrt{\rho_w/\overline{\rho}}u_\tau$ which allows for a similar scaling form in CTBL, $\overline{u'u'}/(u^*)^2$, as the incompressible form, $\overline{u'u'}/u_\tau^2$. In a sense, Eq 2.1 is a restatement of the theory that an essential dynamics of turbulence does not change between the incompressible and compressible turbulence under a weak density fluctuation condition. Therefore, a simple mean density correction to CTBL statistics will restore the behavior of ITBL turbulence statistics at a similar wall normal location and characteristic Reynolds number. Note that Reynolds-averaged quantities are denoted by an overbar, $\overline{f}$, with a single prime denoting a fluctuation relative to this average, f'. Similarly, Favre averaged quantities are denoted by tilde, $\tilde{f}$, and fluctuations from this average are, f''. The variable f represents a flowfield variable such as the streamwise, spanwise or wall-normal velocities which we denote as u, v and w, respectively.

Several experiments [28–30] and simulation studies [22–24, 31] have been published that support this scaling law derived from Morkovin's hypothesis and demonstrated the validity of Morkovin's hypothesis. A good demonstration of Eq. 2.1 is shown in Fig. 2.1 which compares incompressible turbulent intensities at varying Re_τ and a density scaled turbulent intensities at varying mach and semilocal Reynolds number, Re^* where a self-similar Reynolds number trend for both ITBL and CTBL results is observed. Note $Re_\tau = \rho_w u_\tau \delta/\mu_w$, $Re^* = Re_\tau\sqrt{\rho_e/\rho_w}/(\mu_e/\mu_w)$ and $z^* = zu_\tau\sqrt{\overline{\rho}_w/\overline{\rho}}/(\overline{\mu}/\overline{\rho})$ denote a friction Reynolds number, a semilocal Reynolds number and semilocal wall normal distance, respectively. Moreover, μ denotes viscosity and the subscripts 'w' and 'e' will denote wall or boundary layer edge quantities.

As suggested, relationships such as Eq. 2.1 based on Morkovin's hypothesis is bound to breakdown when there exists higher level of thermodynamic property fluctuation. The limit to

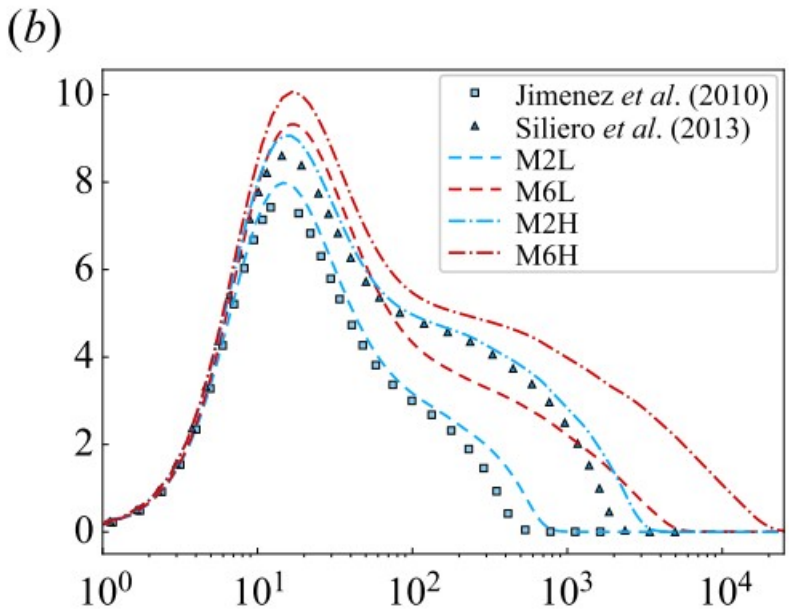

FIGURE 2.1. Favre-averaged streamwise turbulent kinetic energy scaled according to Morkovin's hypothesis, $\frac{\overline{\rho}}{\rho_w}\frac{\widetilde{u''^2}}{u_\tau^2}$, as a function of semilocal wall normal distance, z^*. [2] Note that both y-axis and x-axis label have been cut off from sampling.

which the validity of Morkovin's hypothesis breaks down is reported to be when M' is larger than 0.3 where M' denotes fluctuating Mach number and thus, is a representative quantity of density and pressure fluctuation. The primary reason for this turbulent Mach number limit is that a higher level of thermodynamic property fluctuation is expected to affect the turbulent time/length scales. A general consensus is that this value is reached around freestream Mach number of 4 or 5 [10, 32]. Furthermore, this limit has an significant implication in the validity of SRA discussed hereafter which is another direct result of Morkovin's hypothesis.

SRA is one of the first attempts to relate the velocity field to the temperature field in CTBL with several modified versions of SRA following afterwards [16, 17, 33, 34]. While its derivation detail is included in [10], SRA relations which are derived under assumption of constant Pr and

constant total enthalpy are shown in Eq. 2.2 and Eq. 2.3 for reference.

$$\frac{\sqrt{\overline{T'^2}}}{\overline{T}} = (\gamma - 1)M^2 \frac{\sqrt{\overline{u'^2}}}{\overline{u}} \tag{2.2}$$

$$R_{uT} = \frac{-\overline{u'T'}}{\sqrt{\overline{u'^2}}\sqrt{\overline{T'^2}}} = constant \tag{2.3}$$

where R_{uT} is the correlation coefficient between velocity fluctuation and temperature fluctuation, M is the Mach number, T is the temperature, γ is the ratio of specific heat. Under Morkovin's hypothesis and SRA, Pr_t, which is the ratio of turbulent transport of energy and momentum, is assumed to be Mach invariant and is not affected significantly by the compressibility. The main result of Eq. 2.2 is that once the variance of the velocity fluctuation is known, that of temperature fluctuation can also be found and vice versa.

In addition to the fluctuating quantity, Crocco [14] and Busemann [15] independently developed a temperature-velocity relationship shown in Eq. 2.4 for CTBL by examining a similarity solution between the momentum and energy transport equation under two assumptions, $Pr = 1$ and total enthalpy is constant.

$$\frac{\overline{T}}{T_e} = \frac{T_w}{T_e} + \frac{T_{0e} - T_w}{T_e} + \frac{T_e - T_{0e}}{T_e}\left(\frac{\overline{u}}{u_e}\right)^2, T_{0e} = Te + r\frac{u_e^2}{2C_p} \tag{2.4}$$

While this relationship was developed a few decades before Morkovin's hypothesis, it invokes similar assumptions as Morkovin's hypothesis to relate mean temperature and mean velocity. For this reason, Crocco relation is often considered along with SRA. However, while the assumption of constant Pr has generally been verified to be valid, the assumption of constant enthalpy has been shown to be invalid in several studies [16, 22] and thus contributed to the

breakdown of SRA and Crocco relation especially for cooled-wall condition. This breakdown is clearly demonstrated in Fig. 2.2a where CTBL isothermal DNS cases fail to follow SRA relation in Eq. 2.2. Since then, several modified SRA and Crocco relations [3, 16–18, 33, 34] have been proposed including the widely known Walz's equation [18] and more recent Generalized SRA [3] (GSRA). Waltz's equation is shown to agree well for adiabatic CTBL by accounting for the deviation Pr from unity by modifying the recovery factor, r, in Eq. 2.4 to 0.9. GSRA generalizes the results of Waltz's equation and SRA by Huang et al. [17] by asserting that it is the local recovery enthalpy that keeps constant, not the total enthalpy. The relations of GSRA which are shown in Eq. 2.5 and Eq. 2.6 have been shown to agree well for cold wall CTBL cases [22]. The result of GSRA relations by Zhang et al. [3] is shown in Fig. 2.2b and it shows that GSRA vastly improves in its prediction of isothermal DNS data over SRA results shown in Fig. 2.2a. A similar improvement in the prediction of the relationship between mean velocity and mean temperature for isothermal CTBL cases is also observed when the relation by GSRA is used over Crocco-busemann relationship. Note that s in Eq. 2.7 is the Reynolds analogy factor defined as $s = 2C_h/C_f$ where C_h is the heat transfer coefficient and C_f is the skin friction coefficient.

$$\frac{\sqrt{\overline{T'^2}}/\overline{T}}{(\gamma-1)M^2\sqrt{\overline{u'^2}}/\overline{u}} = \frac{1}{Pr_t(\partial\overline{T}_t)/\partial\overline{T}-1)} \tag{2.5}$$

$$\frac{\overline{T}}{T_e} = \frac{T_w}{T_e} + \frac{T_r - T_w}{T_e} f\left(\frac{\overline{u}}{u_e}\right) + \frac{T_e - T_r}{T_e}\left(\frac{\overline{u}}{u_e}\right)^2 \tag{2.6}$$

where

$$f\left(\frac{\overline{u}}{u_e}\right) = (1 - sPr)\left(\frac{u}{u_e}\right)^2 + sPr\left(\frac{\overline{u}}{u_e}\right) \tag{2.7}$$

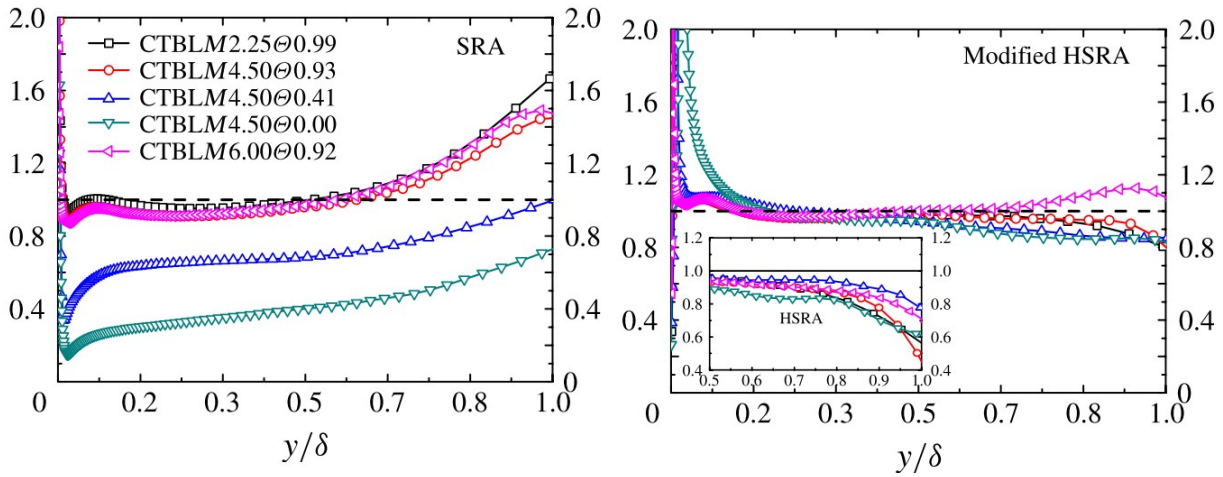

FIGURE 2.2. Comparison between the DNS of CTBLs and the theoretical relations of (a) SRA in Eq. 2.2 and (b) GSRA in Eq. 2.5 [3]. Note Zhang et al. [3] referred to GSRA as 'Modified HSRA'

In summary, Morkovin's hypothesis provides a link between ITBL and CTBL by assuming that the main physics of both ITBL and CTBL remain similar to each other when density fluctuation is weak. In doing so, it suggests that a scaling by mean density to incompressible variables would restore the flow profiles of CTBL to follow the ITBL characteristics. This is not perfect as Morkovin's hypothesis often assumes infinite Reynolds number or an inviscid condition. However, it provides an reasonable prediction performance for CTBL even for cases with relatively low Reynolds number. Moreover, the Strong Reynolds Analogy derived from Morkovin's hypothesis provides relationship between velocity and temperature for both mean and fluctuation component. Several modified versions of SRA have been proposed over the years with GSRA [35] suggested to be the best performing model.

2.2 Wall Bounded Mean Flow

To understand the mean flow in CTBL, one must comprehend the law of the wall from ITBL, which serves as the velocity profile reference for comparison of mean velocity transformation form in CTBL. Thus, this section will first cover the law of the wall and then discuss on various state-of-art mean velocity transformations used for CTBL, providing a detailed description of each transformation.

2.2.1 Law of the Wall

As introduced in section 1, law of the wall is of great importance in ITBL in that it provides self-similar and invariant velocity profiles in ITBL. It is comprised of the inner layer and the outer layer which scales with $z_\tau = \overline{\mu}_w / \left(\overline{\rho}_w u_\tau\right)$ and δ, respectively. More specifically, the inner layer includes the viscous layer, buffer layer and the logarithmic layer. In the viscous layer, the effect of turbulence and convection is minimal and the viscous stress dominates to satisfy the simplified momentum equation shown in Eq. 2.8. Under the zero-pressure gradient flow assumption, the streamwise pressure term can be neglected and Eq. 2.8 can be integrated to derive Eq. 2.9 where $+$ denotes variables normalized by wall quantities such as u_τ, z_τ . This relationship has been shown to hold at $z^+ < 5$.

$$\frac{\partial}{\partial z}\left(\overline{\mu}\frac{\partial \overline{u}}{\partial z}\right) = -\frac{d\overline{p}}{dx} \tag{2.8}$$

$$u^+ = \frac{\overline{u}}{u_\tau} = \frac{z}{z_\tau} = z^+ \quad , \quad z^+ < 5 \tag{2.9}$$

In the log layer where turbulence or Reynolds stress is a dominant form of stress, there also exists a logarithmic law shown in Eq. 2.10 where κ is the von Ḱarmán constant and C is the

additive constant.

$$u^+ = \frac{1}{\kappa} ln\left(z^+\right) + C \tag{2.10}$$

It was first proposed by Prandtl based on the mixing length hypothesis which assumes a linear variation of distance in which a lump of turbulent eddy transfers momentum. This relationship is shown to agree well with experiments and numerical simulations from $z^+ > 30 \sim 50$ up to $z/\delta < 0.15 \sim 0.2$. Despite its accurate description of velocity profile in ITBL, however, the mixing length theory has received much criticism in recent studies for its inaccurate description of turbulence [36]. Therefore, an attention has been given to Millikan's overlap argument [37] which does not invoke any description of turbulence, but rather it only asserts that at large Reynolds number, there must be a region of overlap where both inner scale and outer scale are valid. Millikan's proposal successfully recovers a logarithmic relationship identical to Eq. 2.10 proposed by Prandtl and provides theoretical background behind the equation.

In summary, law of the wall in ITBL describes the near wall behavior of mean velocity profile extremely well and has the theoretical background as well as the empirical and numerical evidence. Together with Morkovin's hypothesis, it is hypothesized that law of the wall form of ITBL exists in CTBL as well when mean velocity profile in CTBL is properly scaled. Therefore, law of the wall serves as a reference relation against any mean velocity transformation models developed for CTBL which are discussed in the next section.

2.2.2 Mean Velocity Transformations

Over the past few decades, various forms of MVT for CTBLs have been proposed [12, 13, 35, 38–40]. These efforts to develop a mean velocity transformation rely on Morkovin's

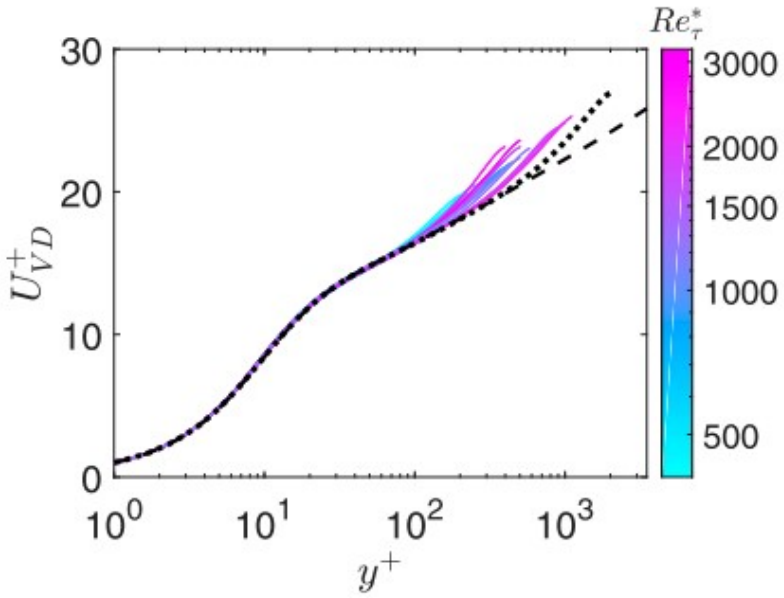

FIGURE 2.3. Van Driest transformation applied to adiabatic CTBL cases from [4]. In their notation, U^+_{VD} is the transformed velocity and y^+ is wall normal distance normalized by z_τ. Colored lines denote CTBL cases at varying Re^* and black lines denote incompressible law of the wall.

hypothesis that it is possible to correct the mean velocity of CTBL with fluid properties and obtain a similar mean velocity behavior as classical law of the wall in ITBL. One of the first successful attempts for developing mean velocity transformation was by Van Driest [12] where the mathematical form of Van Driest transformation is given in Eq. 2.11. U^+_{VD} refers to the mean velocity transformed by the Van Driest transformation. The Van Driest transformation has shown success in scaling adiabatic CTBLs [22,41–43] as demonstrated in Fig. 2.3 where CTBL adiabatic cases with ranging Re^* all agree with incompressible law of the wall. However, several studies reported its limitation in its apparent failure in scaling of cold wall cases leading to increases in the log-law intercept with increasing heat transfer [13,31,40,44,45].

$$U^+_{VD} = \int_0^{u^+} \left(\frac{\overline{\rho}}{\rho_w}\right)^{1/2} du^+ \tag{2.11}$$

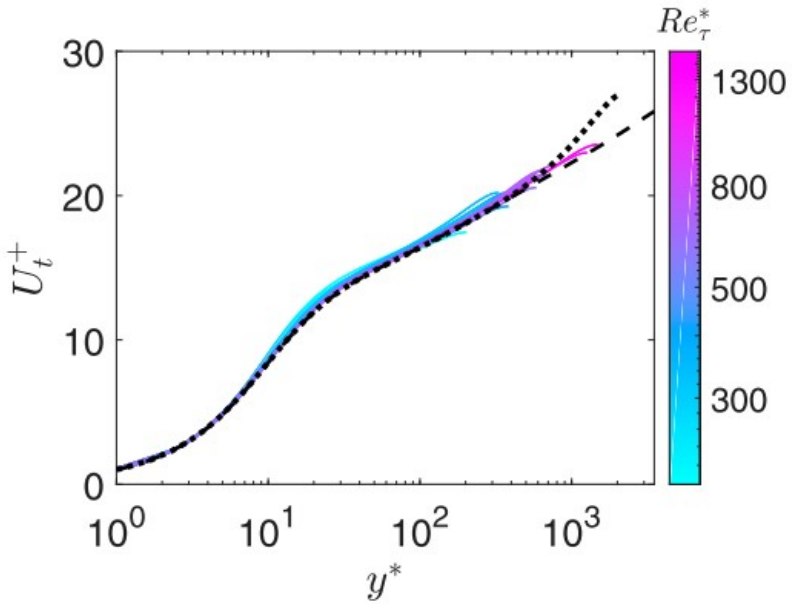

FIGURE 2.4. Total stress based transformation by Griffin et al. [4] applied to both adiabatic and isothermal wall DNS cases with ranging Re^*. In their notation, U_t^+ denotes transformed velocity by GFM transformation and y^* denotes the semilocal wall normal distance. Colored lines denote CTBL cases at varying Re^* and black lines denote incompressible law of the wall.

The most successful MVT that accounts for the near-wall viscosity gradient was independently developed by Trettel and Larsson [13] and Patel et al. [40]. Its mathematical form is given in Eq. 2.12 where U_{TL}^+ denotes the mean velocity transformed by the transformation by Trettel and Larsson [13] and Patel et al. [40]. However, despite their initial success in isothermal CTBL cases [23, 46] with low semi-local Reynolds, Re^*, the scaling remains unsuccessful for cases with increasing Re^* where multiple studies [4, 45] report a large scatter in the log-layer intercept and the slope for such cases.

$$U_{TL}^+ = \int_0^{u^+} \left(\frac{\overline{\rho}}{\rho_w}\right)^{1/2} \left(1 + \frac{1}{2}\frac{1}{\overline{\rho}}\frac{d\overline{\rho}}{dz}z - \frac{1}{\overline{\mu}}\frac{d\overline{\mu}}{dz}z\right) du^+ \tag{2.12}$$

To improve upon the existing models, Griffin, Fu & Moin [4] recently developed a total stress based MVT (GFM) that employs a combination of the viscous stress transformation of

Trettel and Larsson [13] and the quasi-equilibrium assumption based transformation of Zhang et al. [35]. They employ a total stress-based functional form to combine these two transformations, such that each is applied in their region of applicability; Trettel and Larsson [13] in the viscous layer and Zhang et al. [35] further from the wall. Initial explorations of the mean velocity profiles transformed by the GFM approach have shown promising collapse and improvement over earlier MVTs for both adiabatic and isothermal CTBL cases as shown in Fig. 2.4. To examine this model further, the details of GFM model are further discussed in section 4.3.

2.3 Wall Bounded Turbulence

Wall bounded turbulence can be analyzed mainly in two ways. The first approach is by examining the magnitude of different turbulence quantities by ensemble averaging them similar to streamwise turbulent kinetic energy in Fig. 2.1. Another approach is directly examining the turbulent structures using various imaging techniques and frequency domain analysis to examine the turbulence. In this section, theories and recent results using the latter approach are presented and discussed.

2.3.1 Attached Eddy Hypothesis

Wall bounded turbulence is another active area of research that is worth our attention. In particular, many studies have been conducted to examine the behaviors of turbulent intensities and near-wall turbulent structures of turbulent boundary layer flows based on Townsend's attached eddy hypothesis [19]. This theory provides a simplistic description of near wall turbulence

structure which portrays the main characteristic eddies to be essentially attached to the wall in an organized manner. In interpretation of his theory, he suggested that the main eddies near the wall are self-similar and their size scale with the distance from the wall. Also, he proposed that the wall normal motion of the eddies is restricted while motions parallel to the wall is amplified due to the wall blocking effect. From this, Townsend deduced that the variance of the velocity fluctuations in streamwise and spanwise direction can be shown to be dependent on the distance from the wall as shown in Eq. 2.13, Eq. 2.14. He also demonstrated that the variance of the wall normal fluctuation would be a constant as shown in Eq. 2.15. Many experimental studies [47–50] as well as numerical studies [51, 52] have supported Townsend's equations.

$$\frac{\overline{u'u'}}{u_\tau^2} = B_1 - A_1 \log\left(z/\delta\right) \tag{2.13}$$

$$\frac{\overline{v'v'}}{u_\tau^2} = B_2 - A_2 \log\left(z/\delta\right) \tag{2.14}$$

$$\frac{\overline{w'w'}}{u_\tau^2} = B_3 \tag{2.15}$$

Following Townsend's attempt to predict turbulent intensity, Perry and Chong [5] proposed a spectral scaling law for deriving the Townsend's equations. In the spectrum of wavenumbers, k_i, representing the eddies of different sizes in $i = 1, 2, 3$ direction, Perry and Chong followed Townsend's assumption that eddies parallel to the wall follow similar scaling laws to each other while eddies normal to the wall exhibits an independent behavior. In particular, for the motion of eddies parallel to the wall, i.e. $\overline{u'^2}$ and $\overline{v'^2}$, they divided the wavenumber space into 5 distinctive zones as shown in Fig. 2.6. There are three zones denoted by 'outer-flow' scaling, 'inner-flow' scaling and Kolmogoroff scaling in Fig. 2.6, each representing the energy spectrum zone

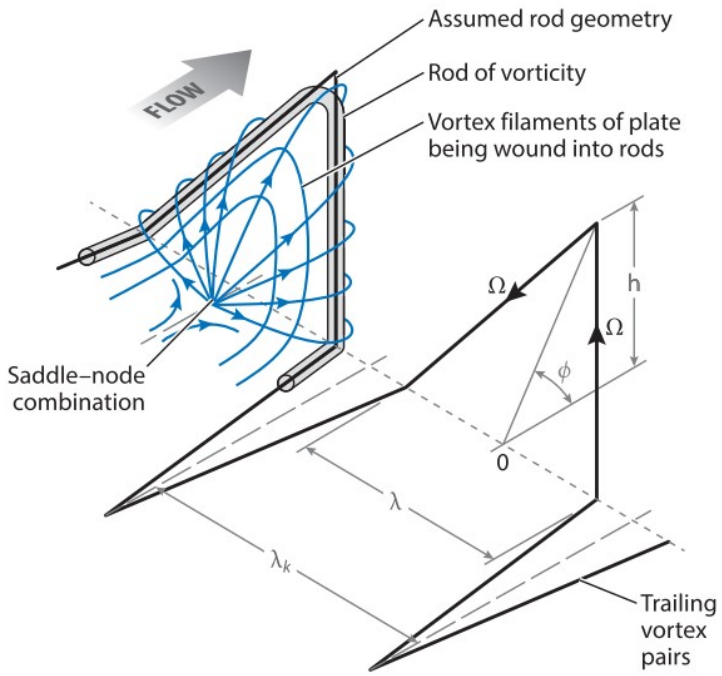

FIGURE 2.5. Λ-shaped hairpin vortex [5]

governed by the large,intermediate and small wavenumbers, respectively. In each zone, eddies of size δ,y,η with decreasing size in order are the main eddies responsible for the energy spectrum,Φ, in large,intermediate and small wavenumbers, respectively. Note that η denotes the Kolmogorov length scale which is the smallest length scale of turbulence before dissipation by viscous effect. The remaining two regions denoted by Overlap region I and II in Fig. 2.6 arise because nature is in continuum and eddies of different sizes must have a overlapping region where different eddy sizes cast their influence over the similar energy spectrum. Therefore, the overlap region I is affected by eddies of size δ and y while the overlap region II is affected by eddies of size y and η. In addition to confirming Townsend's equations, Perry and Chong derived k^{-1} and $k^{-5/3}$ scaling laws given by Eq. 2.16 and Eq. 2.17, respectively, by performing dimensional analysis in each overlap region

$$\frac{\Phi_{11}\left(k_1 y\right)}{u_\tau^2} = \frac{A_1}{k_1 \delta} \tag{2.16}$$

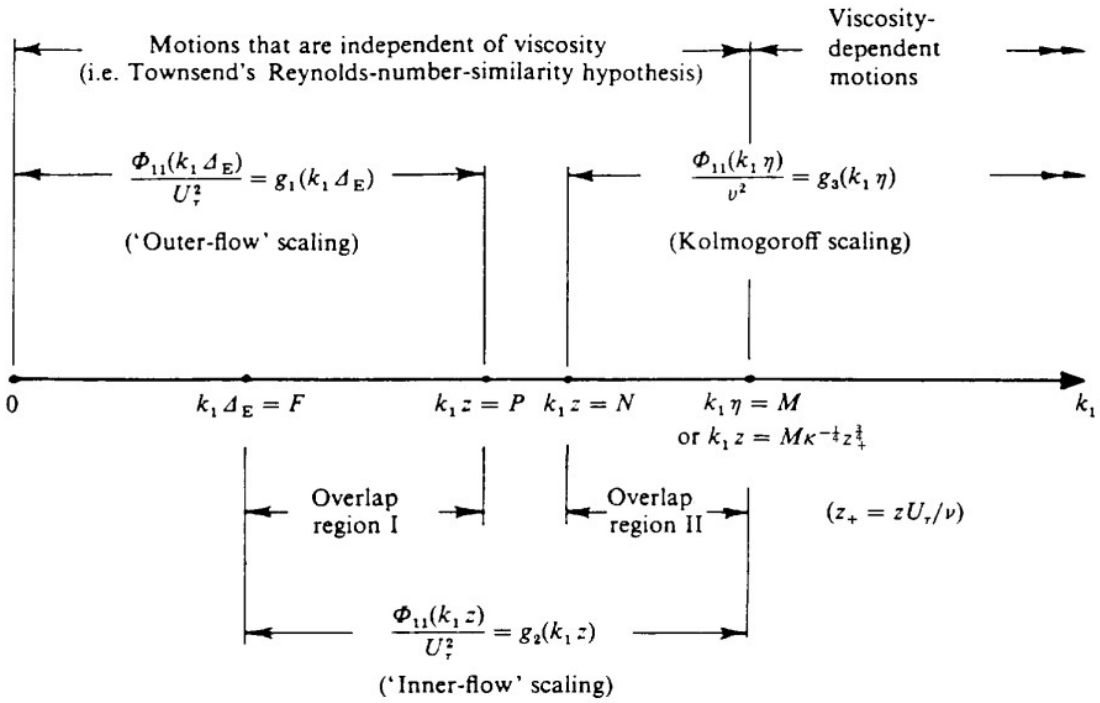

FIGURE 2.6. Wave number regions with different scaling [6]

$$\frac{\Phi_{11}\left(k_1 y\right)}{u_\tau^2} = \frac{K_0}{\kappa^{2/3}\left(k_1 y\right)^{5/3}} \tag{2.17}$$

where Φ_{11} represents the power spectral density in streamwise direction. Since the proposal of k^{-1} and $k^{-5/3}$ spectral scaling laws, a few studies [49, 53–55] have confirmed the relationships at least partially with the latter being more readily verified than the other. However, Perry and Chong [5] suggested that k^{-1} scaling law is expected to be only observable at very high Reynolds number and k^{-1} scaling law still remains to be verified. Finally, for eddies normal to the wall, there is no overlap region I because of the wall blocking effect and there only exhibits the $k^{-5/3}$ law.

Additionally, Perry and Chong [5] proposed that turbulent boundary layer consists of trains of Λ-shaped physical turbulence structures varying in size that are attached to the wall as depicted in Fig.2.5. While representing the turbulent boundary layer with Λ-shaped turbulence

structure was first conceptualized by Theodorsen [56], it was Perry and Chong's work [5] that first made a use of the structure in a turbulence intensity prediction model. These structures are reported to be responsible for a significant portion of turbulent kinetic energy and to provide physical understanding of turbulent energy cascade from the outer layer to the near-wall layer.

Following Morkovin's hypothesis, the above attached eddy hypothesis developed for ITBL is also extended to CTBL by accounting for the variation of mean density in the analysis of energy spectrum [10]. Smits and Dussauge [10] derived k^{-1} scaling law by performing similar dimensional analysis as done in ITBL studies(but with density corrected velocity scales). With regard to the $k^{-5/3}$ scaling law, they noted that the Kolmogorov velocity and length scale will vary due to temperature gradient and may result in a different scaling law. However, it was shown that $k^{-5/3}$ scaling law will remain intact as long as friction Mach number, $M_\tau = u_\tau/a_w$, remains below 1. In agreement with this analysis, Spina experimentally observed the $k^{-5/3}$ scaling behavior for CTBL when the density scaled energy spectrum is used [57]. However, similar to ITBL studies, the k^{-1} scaling law is expected to only show at higher Reynolds number flow. Given that there is a general lack of experimental or high fidelity simulation data at high Reynolds number in CTBL, the observation of k^{-1} scaling law remains to be illusive.

2.3.2 Turbulent Structures

An adaptation of attached eddy hypothesis to depict near wall turbulence naturally suggests that there exists turbulent structures ranging in size that scale with the distance from the wall. In line with this theory, the forementioned Λ-shaped hairpin vortex, quasi-streamwise vortex, near-wall streamwise velocity streaks, large scale motion and very large scale motion, listed in an order

of increasing size, have been identified in turbulent boundary layers. These structures are also reported to account for significant amount of the near-wall turbulent kinetic energy production. Therefore, the topology and role of these turbulent structures that have been reported in the past few decades are reviewed in this section.

As previously noted, Λ-shaped hairpin vortex was first proposed by Theodorsen [56] and was later adopted to Townsend's attached eddy hypothesis by Perry and Chong [5] as the basic turbulent structure populating the inner (viscous layer) and outer (logarithmic layer) region of turbulent boundary layers. Focusing our attention to the inner region for now, several experimental works also observed the existence of long streamwise velocity streaks with streamwise length of approximately 1000 wall units(+) and spanwise length of 100 wall units in the near wall region [58–60]. These velocity streaks are important in that these velocity streaks are closely linked with quasi-streamwise vortices to constitute a near-wall self sustaining turbulence cycle which is reported to be at least partially responsible for the near-wall turbulent kinetic energy peak. This closed-loop cycle was proposed by Jiménez and Pinelli where velocity streaks are formed by the streamwise vortices which are then generated by the breakdown of the streaks [61]. Adrian et al. [62] then characterized the quasi-streamwise vortices to be a portion of Λ-shaped hairpin vortex and coined the term 'Hairpin Vortex Signature' (HVS), thereby linking the quasi-streamwise vortices and streamwise streak to attached eddy hypothesis as well.

However, as Pirozzli et al. [63] noted, there exists discrepancy between the streamwise length of the velocity streak ($\sim$1000 wall unit) and the typical length of HVS ($\sim$150 wall unit). To bridge this gap, Adrian et al. [62] demonstrated that HVS often occur in 'vortex packets' consisting of multiple HVSs aligned in the streamwise direction within the same velocity streak. A typical vortex packet consisting of multiple HVSs is shown in Fig. 2.7. Note that an individual

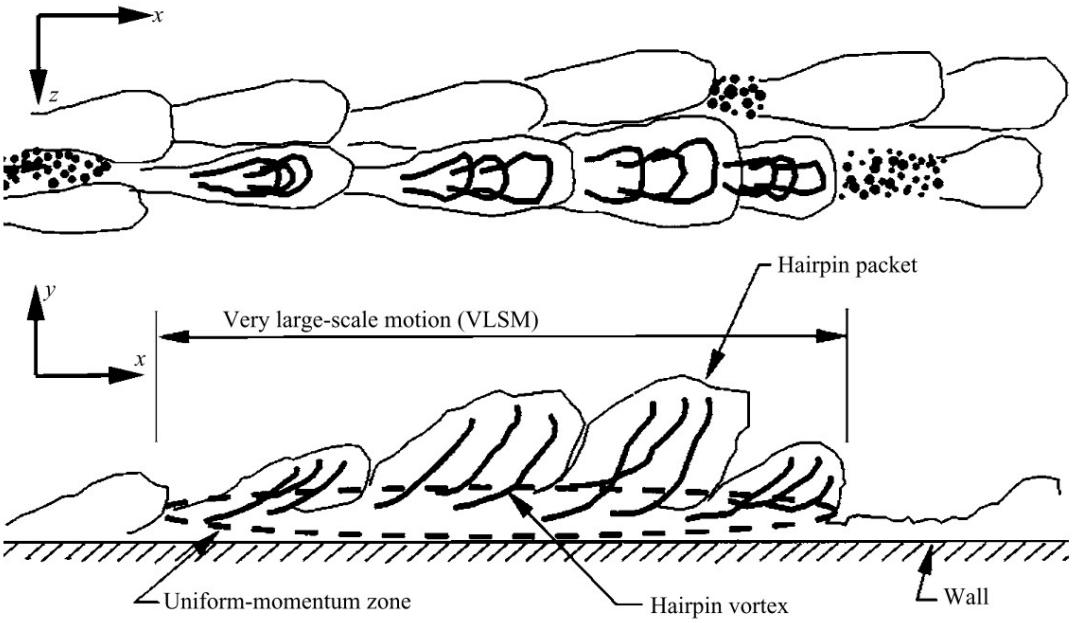

FIGURE 2.7. Generic representation of vortex packets [7]

HVS is identical to the Λ-shaped hairpin vortex shown in Fig. 2.5. Adrian et al. [62] also suggested that the uniform momentum zones [64] which are commonly observed in turbulent boundary layers can be explained by the existence of quasi-streamwise vortices (tails of HVS) aligning in streamwise direction as shown in Fig. 2.7, providing further evidence.

Furthermore, this conglomerate of structures are shown to be of importance in generation of near-wall turbulent stresses. In particular, since Kline et al. [58] introduced that the velocity streaks discussed so far undergoes a period of bursting and is responsible for the turbulence production, several studies [65–67] have been conducted to detect the bursting phenomena and structures involved. For example, the variable interval time averaging technique by Blackwelder and Kaplan [67], which detects the region where variance of velocity fluctuation over a short interval is above a predetermined threshold, has been used to identify the HVS in Fig. 2.7 [62]. A quadrant analysis by Lu and Willmarth [65] is also extensively used to detect the bursting phenomenon. The quadrant analysis involves classifying quadrant plane of the streamwise(u')

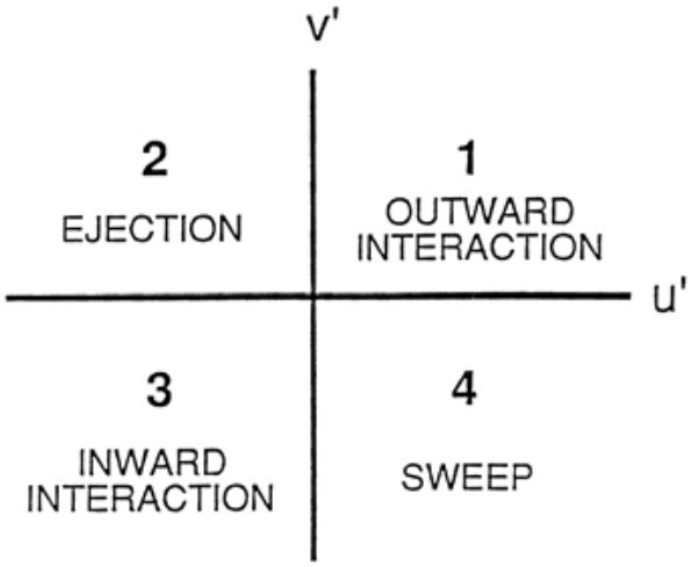

FIGURE 2.8. Quadrant Analysis with conventional names of bursting events. Note wall normal velocity fluctuation is denoted by v' here. [8]

and wall-normal(w') velocity fluctuation as shown in Fig. 2.8 where Q1 (outward interaction) has $u' < 0$, $w' > 0$, Q2 (ejection) has $u' < 0$, $w' > 0$, Q3 (inward interaction) has $u' < 0$, $w' < 0$ and Q4 (sweep) has $u' < 0$, $w' > 0$. An observation of the signs pertaining velocity components in each quadrant hints that Q2 (ejection) and Q4 (sweep) are important events that correspond to the turbulent kinetic energy production($-\overline{u'w'}\ d\overline{u}/dz$) and the bursting event reported by Kline et al. [58].

Large scale turbulent motions in the logarithmic layer have also been of great interest since they provide physical understanding of turbulent energy cascade from the outer layer to the near-wall layer. Similar to the inner layer, the outer layer and logarithmic layer are also populated by the vortex packets and streaks consisting of individual hairpin vortices [62]. Consistent with attached eddy hypothesis, various models subsequently predicted that the size of vortex packets can grow either by merging with each other [68] or by self-regeneration [69]. In addition, several studies [62, 69, 70] suggested that these vortex packets contributed significantly to the turbulent

stresses and related transport processes in the logarithmic layer.

Consistent with observations regarding the existence of vortex packets, large scale motion (LSM) has been found to consist of a packet of hairpins with their streamwise length extending up to 2-3δ at a typical 20 degrees inclination angle [62, 71]. Furthermore, studies have also observed even larger structures consisting of packets of hairpin vortices aligned together in the streamwise direction forming what is referred to as 'superstructures' (SS) [72] in the case of boundary layer or 'VLSM' in the case of pipe flows [7]. To examine the size of SS in the boundary layers, Hutchins et al. used the spanwise hot-wire rake and reported the length of SS to extend up to 20 δ. In addition, they demonstrated that SS meanders substantially in the spanwise direction [73]. Similar to SS, VLSM in pipe flow was shown to extend to 20R with a similar meandering characteristics [74]. Hutchins and Marusic [72] experimentally analyzed these large-scale structures using pre-multiplied streamwise energy spectra, $k_x\phi_{u'u'}$ with Re_τ 2800 to 17000. With boundary layer dataset with a large range of Reynolds number available to them, they reported a Reynolds number dependent outer spectral peak position which represents the wavelength of SS. In a more recent study by Vallikivi et al. [49], the pipe data [48, 75] and the boundary layer data [76] with Re_τ approximately ranging from 3000 to 70000 were compared using pre-multiplied streamwise energy spectra to quantify the VLSM(or SS) and LSM characteristics and found a comparable Reynolds number dependent trend of outer spectral peak to the trend reported by Hutchins and Marusic [72].

Following Morkovin's hypothesis, it is then expected that similar turbulent structures exist in both inner and outer layers of CTBL as well. Lian et al. [22] used instantaneous mass flux fluctuations to visualize the near-wall streaks at varying freestream Mach number, M_e, from the incompressible range to M_e of 12. Pirozzoli et al. [63] also highlighted by performing a DNS

study at $M_e = 2$ that near-wall alternating velocity streaks in buffer layer has characteristic length of 1000 wall units similar to ITBL. Also, they demonstrated that the the locations of quasi-streamwise vortices and hairpin structures coincide with the low momentum streaks zone as has been observed by Ringuette and Martin who studied turbulent structures at $M_e = 3$ [20]. Furthermore, several studies [20, 63] devised a vortex detection algorithm based on swirling strength, λ_{ci} (see [63] for definition), to visualize vortex packets near the wall and confirmed that the packets are comparable to packets identified in ITBL studies [62, 69], thereby providing a further support for Morkovin's hypothesis.

Large-scale turbulent structures similar to the ones observed in aforementioned incompressible studies have been reported to exist in compressible wall bounded flow in number of studies [2, 20, 21, 23, 24, 77, 78]. Duan et al. [78] performed DNS simulation of compressible boundary layers at $Re_\tau \simeq 500$ with Mach number ranging from 3 to 12 and visualized large-scale structures by utilizing the numerical schlieren. Ganapathisubramani et al. [77] experimentally examined using PIV at $M_e = 2$ and observed velocity streaks spanning over 8δ in streamwise direction at $z/\delta = 0.16$, representative of large turbulent structures. They noted that the these long velocity streaks are consistent with VLSM reported by Kim and Adrian [7]. More recently, several CTBL studies [2, 21, 23, 24], despite basing on different velocity fluctuation signals, also reported a presence of the outer peaks in logarithmic layer in pre-multiplied spectra with their wavelengths around $1 \sim 2\delta$ and $3 \sim 10\delta$, indicative of LSM and VLSM, respectively. Based on these findings, the attached eddies are shown to exist in CTBL flow as well regardless of the Reynolds number.

Chapter 3: Simulation Details and Data Acquisition

For the present dissertation, DNS data obtained using the CRoCCo code [1] has been primarily used to probe the compressible turbulent boundary layer. The database has been analyzed with various post-processing methods. In what follows, details of simulation is discussed.

3.1 Direct Numerical Simulation

Direct numerical simulation is an important tool in examination of turbulent flow in detail as it can resolve the largest scale to the smallest scale that exist in the flow field without resorting to any modelling. A use of DNS is especially useful in the analysis of CTBL because CTBL is populated by turbulent motions with a large range of length/time scales that are relevant to the transport of turbulence. Moreover, with an increasing computational power, DNS is continuously pushed to simulate more computationally stringent but physically relevant conditions to help us understand important physics in CTBL that are not easily observable in experiments. Despite this advantage, using DNS to solve CTBL in a full-scale engineering application is challenging as the grid size requirement grows as $Re_L^{9/4}$ for a full three dimensional simulations. Moreover, ensuring a high order of accuracy, high bandwidth resolution and low numerical dissipation is especially difficult because there exist additional compressible effects such as shocks that requires a use of shock-capturing schemes while remaining computationally efficient. To alleviate this problem, a

highly parallelized and high fidelity DNS code has been developed at CRoCCo laboratory that uses 4th order bandwidth optimized weighted essentially non-ocscillatory spatial scheme [79,80] for convection term, 4th order central scheme for diffusion term and 3rd order low storage Runge-Kutta time marching method [81].

3.1.1 Governing Equation

The governing equations used for DNS are the conventional mass, momentum and energy equation with perfect gas assumptions provided in Eq.3.1, Eq.3.2 and Eq. 3.3. Note that an Einstein notation has been used in this section for a concise representation of the governing equations where the definitions of u and x are the velocity and physical coordinate in the direction determined by the indices, i,j and k.

$$\frac{\partial \rho}{\partial t} + \frac{\partial}{\partial x_j}\left(\rho u_j\right) = 0 \tag{3.1}$$

$$\frac{\partial \rho u_i}{\partial t} + \frac{\partial}{\partial x_j}\left(\rho u_i u_j\right) = \frac{\partial}{\partial x_j}\left(-p\delta_{ij} - \sigma_{ij}\right) \tag{3.2}$$

$$\frac{\partial \rho e}{\partial t} + \frac{\partial}{\partial x_j}\left(\rho e u_j\right) = \frac{\partial}{\partial x_j}\left(-p u_j + u_j \sigma_{ij} - q_j\right) \tag{3.3}$$

where σ_{ij} is the shear stress tensor shown in Eq. 3.4,

$$\sigma_{ij} = 2\mu S_{ij} - 2/3\mu\delta_{ij}S_{kk} \tag{3.4}$$

where $S_{ij} = (\partial u_i/\partial x_j + \partial u_j/\partial x_i)/2$ is the strain rate tensor. μ is determined by either power law or Sutherland law [82] depending on the flow conditions. Heat flux, q_j is determined by Fourier

law, given by $q_j = -k\,\partial T/\partial x_j$ where k is the thermal conductivity. $e = C_v T + 1/2 u_i u_i$ is the total energy per unit mass where C_v is the specific heat at constant volume.

3.1.2 Numerical Methods

The methods used to numerically represent the governing equation provided in section 3.1.1 are 4^{th} order weighted essentially non-oscillatory bandwidth optimized (WENO-BO) scheme [79, 80] for a convection term, 4^{th} order central difference scheme for a diffusion term and low storage 3^{rd} order Runge-Kutta (RK3) method [81] for time marching. While the implementation and the theory of 4^{th} order central difference scheme and RK3 time marching scheme are straightforward and are, therefore, not discussed here, WENO-BO scheme requires a detailed review because the convection term, that WENO-BO scheme treats, is often times the most difficult term to accurately predict. This difficulty mainly arises from the hyperbolic nature of the convection equation which requires the numerical scheme to respect the direction of information propagation from the domain of influence. Also, because of possible discontinuities due to shocks, a numerical scheme must be non-dispersive while remaining non-dissipative to prevent both oscillations and inaccuracy. WENO-BO [79, 80] addresses these problems by improving upon the 3rd order WENO method by Jiang and Shu (WENO-JS) [83].

The details of WENO-BO scheme are described hereafter. First consider the one dimension wave equation,

$$\frac{\partial u}{\partial t} + \frac{\partial}{\partial x} f(u) = 0 \tag{3.5}$$

Representing Eq. 3.5 on a discretized grid involves approximating u in a semi-discretized format as shown in Eq. 3.6.

$$\frac{\partial \hat{u}_i}{\partial t} = -\frac{1}{\Delta}\left(\hat{f}_{i+1/2} - \hat{f}_{i-1/2}\right) \tag{3.6}$$

where $\hat{u}_i$ and $\hat{f}_i$ are the numerical approximation of u and $f(u)$ at i^{th} grid point. Note $i + 1/2$ is an interface between i and $i + 1$. $\hat{f}(u)$ accent has been used to denote discrete prediction of the continuous function, $f(u)$. Also, because the information of this wave equation travels along the characteristics of the equation especially at high speed flows such as CTBL, the convection terms in Eq. 3.1, Eq. 3.2 and Eq. 3.3 are transformed into decoupled forms of equation in characteristic space which are solved in a discretized form in Eq. 3.6.

Each flux at the interface follow similar mathematical treatment to Steger and Warming [84] where the flux is reconstructed by summing flux component associated with the positive and negative directions of wave propagation, f_i^+ and f_i^-, respectively as shown in Eq. 3.7.

$$\hat{f}_i = \hat{f}_i^+ + \hat{f}_i^- \tag{3.7}$$

WENO-BO [9] is then used to form the flux, $\hat{f}_i^+$ or $\hat{f}_i^-$ by summing weighted contributions from several different candidate stencils as shown in Eq. 3.8. A sample stencil used in WENO-BO method is shown in Fig. 3.1 where 4 stencils are used compared to 3 stencils in WENO-JS, completing symmetric representation of candidate stencils and, thus, resulting in a less dissipative scheme than WENO-JS.

$$\hat{f}_{i+1/2}^+ = \sum_{k=0}^{r-1} \omega_k q_k^r \tag{3.8}$$

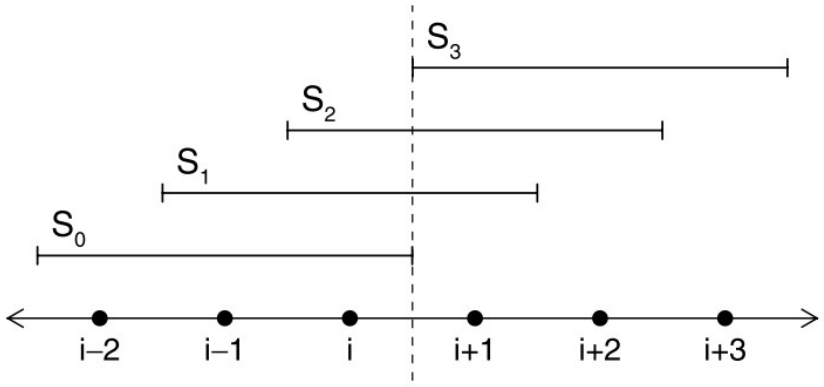

FIGURE 3.1. Candidate stencils S_k for the numerical flux $\hat{f}^+_{i+1/2}$ when r = 3 for WENO-BO method [9]

where q^r_k is the flux approximation on k^{th} stencil and the weights assigned to the stencil is ω_k. r is the number of grid points used to construct each stencil and $r = 4$ is used for WENO-BO method in CRoCCo code. Also, note that r determines the theoretical order of accuracy for WENO method of interest. An individual flux approximation from each stencil, q^r_k, is calculated from Eq. 3.9.

$$q^r_k|_{i+1/2} = \sum_{l=0}^{r-1} a^r_{kl} f(u_{i-r+k+l+1}) \tag{3.9}$$

where a^r_{kl} is stencil coefficient and is provided in [9]. The weights are determined by Eq. 3.10

$$\omega_k = \frac{\alpha_k}{\sum_{k=0}^{r-1} \alpha_k} \tag{3.10}$$

where α_k is determined in Eq. 3.11.

$$\alpha_k = \frac{C^r_k}{(\epsilon + IS_k)^p} \tag{3.11}$$

where ϵ is a small number to prevent division by zero and p is a sensitivity coefficient to

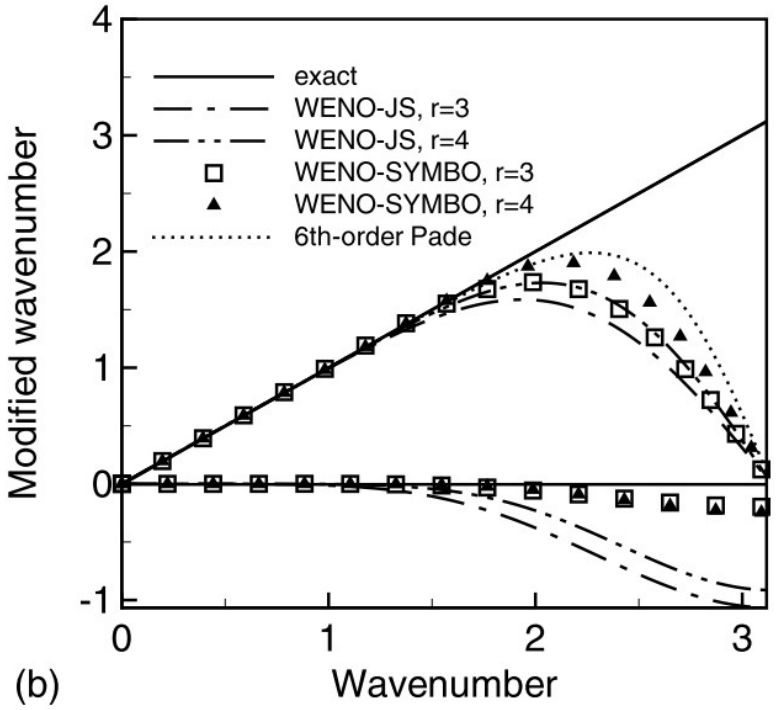

FIGURE 3.2. Performance of bandwidth resolving characteristics of WENO-BO method compared to WENO-JS and 6^{th} order Padé scheme [9]

modify the response of WENO method to smoothness measurement, IS_k. C_k^r is the optimal weights designated by different WENO methods. For details of the smoothness measurement calculation or coefficients related to the WENO-BO model, refer to Martin et al. [9]. As may be inferred from Eq. 3.11, the smoothness of the flow profile is measured to decrease the magnitude of the weights, ω_k, in the region of discontinuity so that the stencils in such region do not contribute to the flux formation causing an unwanted oscillation. This particular implementation of smoothness WENO-BO [9] is identical to the treatment in WENO-JS [83]. However, as mentioned above, WENO-BO makes a modification to WENO-JS by adding a 4^{th} stencil making the collection of stencils symmetric. A characteristic of central(symmetric) schemes is that they are less dissipative and similar effect is achieved by adding a 4^{th} in WENO-BO method. A second modification in WENO-BO is in the calculation of optimal weights, C_k^r where WENO-BO opts to maximize the bandwidth resolving characteristics unlike WENO-JS which opts for a higher order accuracy. These two modifications made in WENO-BO improve the scheme so that it reduces the phase errors as well as dissipative amplitude errors as seen in Fig. 3.2.

3.2 Compressible Turbulent Boundary Layer Database

3.2.1 Flow Conditions

The direct numerical simulation CTBL database [1] developed by CRoCCo code is summarized in Table 3.1. All simulations employ low-enthalpy, non-reacting conditions typical of ground test facilities. The working fluid is callorically perfect air for all cases except for M10T3 which utilizes callorically perfect Nitrogen(N_2). The boundary layer edge Mach number, M_e ranges from 3 to 12 to highlight the Mach number effects. The semi-local friction Reynolds number,

Re^*, ranges from 800 to 34000, approximately, to highlight Reynolds number effects in compressible turbulent boundary layer flow. While a number of cases are adiabatic, the $\overline{T}_w/\overline{T}_r$ ratio, as well as the wall heat transfer rate, $B_q = q_w/(\overline{\rho}_w C_p u_\tau \overline{T}_w)$, range from 0.2 to 1.0 and from 0 to -0.17, respectively, where q is the surface heat flux, C_p is the heat capacity at constant pressure and $\overline{T}$ is the mean temperature. The wall temperature $\overline{T}_w$ is given as a fraction of the adiabatic recovery temperature $\overline{T}_r = \overline{T}_e(1 + 0.9M_e^2(\gamma - 1)/2)$, where γ is the ratio of specific heats. The friction Reynolds number at wall conditions, Re_τ varies between 475 and 825. All values of Reynolds number listed in Table 3.1 are measured at the outlet plane of the computational domain. The locations of the data collection outlet plane x_o/δ are provided in table 3.2 where δ is the thickness of the boundary layer at 99% of the freestream velocity measured at the outlet plane.

The incompressible channel flow DNS database of Lee & Moser [52] and Bernardini & Pirozzoli [85] with Re_τ ranging approximately from 1000 to 5200 is listed in table 3.3 to be used as reference IBTL cases.

For the analysis provided in Chapter 5, two additional Reynolds numbers, Re_τ and Re^* are defined in table 3.4. While they use the same notation compared to their counterparts, Re_τ and Re^*, included in table 3.1, the momentum based boundary layer thickness is used to define Re_τ and Re^* in table 3.4. Furthermore, high Re_τ cases, M2H and M6H, from Cogo et al. [2] are analyzed together with the CTBL database in Lee et al. [1] in Chapter 5 to perform a parametric study on the effect of different forms of Reynolds numbers on large scale motions. Note that the CTBL database in Lee et al. [1] is the database included in table 3.1.

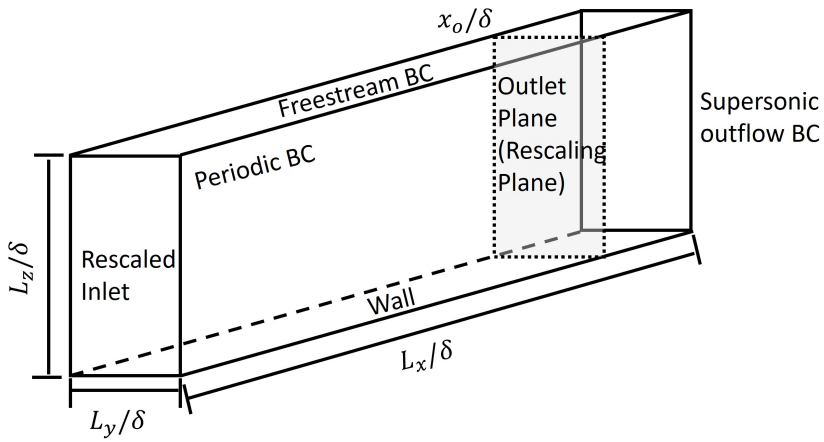

FIGURE 3.3. Generic computation domain with outlet (recaling) yz plane

3.2.2 Computational domain and simulation set-up

The boundary conditions and initialization procedures used to create the high-fidelity CRoCCo Lab CTBL database for this study are documented and have been verified in previous studies [9, 79, 86, 87].

The computational domain size, grid resolution, and simulation duration of the datasets are provided in Table 3.2. A typical computational domain used in the simulation without the auxiliary domain is shown in Fig. 3.3. The outer dimensions of the computational boxes are given in units of δ measured at the outlet plane. All runs use spanwise periodicity. The domain width varies among the runs but ranges between 5 and 10δ. All cases use the recycle/rescale method of Xu & Martin [87] to assign the inflow boundary conditions where the rescaling plane is shown in Fig. 3.3. Note that the rescaling plane and outlet plane for statistics sampling are identical. Large-scale structures are artificially introduced at the inlet due to the recycle/rescaling method, requiring domains that are long enough for the flow to become decorrelated with from the inflow. For most cases, the domain was approximately 20 to 30 times the outlet boundary layer

thickness. For M7T5-L and M12T5-L an extended domain length of approximately 40 δ was employed in two stages, first from $x = 0$ to approximately 20δ in M7T5* and M12T5* (which we refer to as auxiliary cases), and then from about roughly 20δ to 40δ in M7T5-L and M12T5-L.

To assess the adequacy of the domain size, a two point correlation coefficient of the streamwise, spanwise and normal velocity components, as well as the temperature and density at $z/\delta = 0.2$, is plotted for both M5T1 and M12T5 which are the cases with the lowest and the highest Re^*, respectively. The streamwise and spanwise correlation coefficients in figure 3.4 drop to near 0 at locations with a large enough separation, suggesting that the domains are sufficiently long. Similar results were observed for other cases.

Grid resolutions are listed in Table 3.2 relative to the wall-referenced inner viscous length scale $z_\tau = \overline{\mu}_w/\overline{\rho}_w u_\tau$ as indicated by the '+' superscript. The computational grids are made with constant spacing in the streamwise and spanwise directions (Δx^+ and Δy^+). Geometric stretching is used in the wall-normal direction where $z_k^+ = z_2^+(\chi^{k-1} - 1)/(\chi - 1)$ and k indicates the wall-normal grid index so that the finest resolution is at the wall surface. The first grid point away from the wall is z_2^+ and the factor χ determines the rate of stretching. The grid resolution of the DNS runs has been shown to be sufficient for the current DNS computational method and at the given flow conditions in previous publications. In particular see Martin *et al.* [86], Duan *et al.* [22, 79, 88, 89].

For the statistical analysis, time-domain signals of primitive flow variables are collected from the outlet plane, x_o/δ, of each run. The total sample time in outer time units $t(\overline{u}_e/\delta)$ is provided in Table 3.2. No statistics are presented from the auxiliary boundary layer runs (M7T5* and M12T5*).

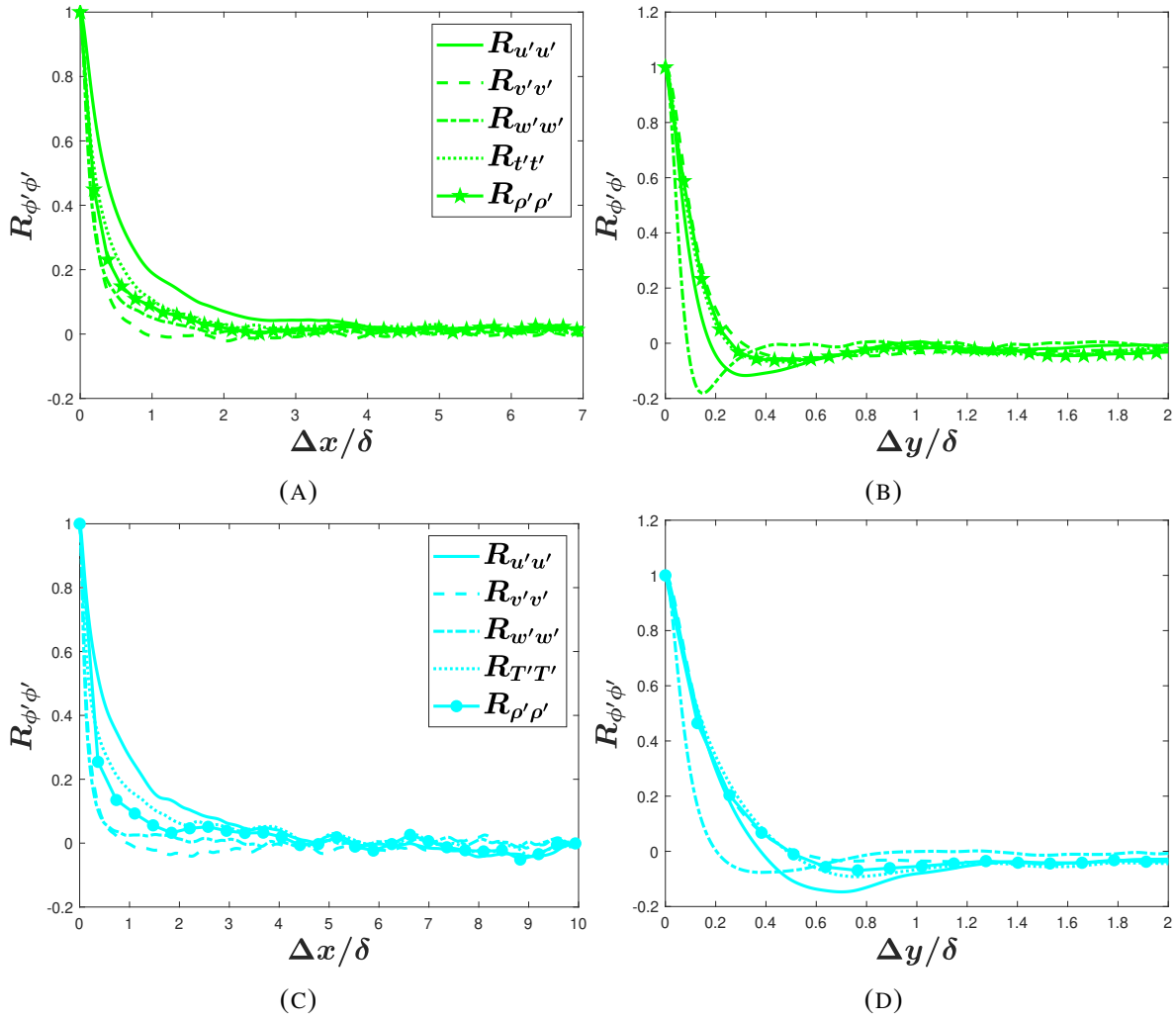

FIGURE 3.4. Two point correlation coefficient, $R_{\phi'\phi'}$, for streamwise, spanwise and wall-normal velocity as well as temperature and density components at $z/\delta = 0.2$. (A) Streamwise M5T1 (B) Spanwise M5T1 (C) Streamwise M12T5 (D) Spanwise M12T5

TABLE 3.1. Boundary layer edge and wall parameters of DNS database. [1]

Case	Viscosity Law	M_e	$\overline{u}_e$ m/s	$\overline{T}_e$ K	$\overline{T}_w/\overline{T}_r$	$-Bq$	Re_τ	Re^*	u_τ $m \cdot s^{-1}$	$\overline{\rho}_w$ $kg \cdot m^{-3}$	$\overline{\rho}_e$ $kg \cdot m^{-3}$	line&symbol
M3T5	Power	3.0	882.5	220	1.0	0.0	530	1650	44.5	0.0366	0.0917	
M5T5	Power	4.9	1472	225	1.0	0.0	470	3870	81.5	0.0182	0.0968	
M7T5-L	Power	6.9	2069	224	1.0	0.0	550	9450	115.9	0.00969	0.0926	
M12T5-L	Power	11.7	3612	236	1.0	0.0	550	33990	213.1	0.0038	0.1015	
M5T3	Power	4.9	1477	222	0.5	0.05	610	2350	68.0	0.0324	0.0950	
M5T1	Power	5.0	1498	223	0.2	0.17	830	800	48.4	0.0973	0.0951	
M10T3	Keyes(N2)	9.1	1410	58.6	0.5	0.11	491	4827	63.0	0.0079	0.0403	

TABLE 3.2. Computational domain size and grid resolution for the DNS data [1]. Datasets with case name ending in '-L' are long-box runs with the domain length extended utilizing starred (*) auxiliary simulations at their inlet. All other cases use the rescaling method of Xu & Martin [87] for inflow assignment. The $\sim$ indicates the cumulative sampling distance once auxiliary simulation distances are taken into account.

Case	N_x	N_y	N_z	δ mm	L_x/δ	L_y/δ	L_z/δ	Δx^+	Δy^+	z_2^+	χ	$t\overline{u}_e/\delta$	x_o/δ
M3T5	1820	880	110	9.3	28.7	5.7	7.5	8.3	3.4	0.32	1.063	143	26.8
M5T5	1820	880	110	16.6	27.2	5.4	8.1	7.1	2.9	0.26	1.061	134	26.1
M7T5*	1780	1160	110	39.8	21.1	5.6	6.12	6.6	2.7	0.26	1.061	134	20.2
M7T5-L	1580	1080	116	39.8	21.0	5.6	7.6	7.4	2.9	0.28	1.061	110	40.2 $\sim$
M12T5*	1640	1300	110	125.8	20.4	5.4	5.8	6.8	2.4	0.28	1.060	110	19.0
M12T5-L	1640	1240	116	125.8	20.4	5.4	7.2	6.8	2.4	0.29	1.060	142	38.7$\sim$
M5T3	2032	1080	106	9.0	25.4	5.1	8.4	7.6	2.9	0.32	1.069	199	24.0
M5T1	2080	1648	110	2.5	19.5	5.8	7.3	7.7	2.9	0.29	1.069	190	18.5
M10T3	1920	1680	112	17.8	30.3	10.2	10.7	7.8	2.9	0.31	1.065	93	29.0

TABLE 3.3. Incompressible Channel Flow DNS Database

Case	Re_τ	line&symbol	Reference
LM5200	5186	—— ■	Lee & Moser (2015) [52]
LM2000	1994	- - - - ♦	Lee & Moser (2015) [52]
LM1000	1000	····· ★	Lee & Moser (2015) [52]
BOP4100	4079	-·-·-· ●	Bernardini and Pirozzoli (2014) [85]

TABLE 3.4. Selected parameters from compressible turbulent boundary layer DNS Database from [1, 2]. M_e is the freestream Mach Number. B_q is wall heat transfer rate. Re_τ is the friction Reynolds number, Re^* is the semi-local Reynolds number, $Re_{\tau,\rho u}$ is the momentum boundary layer thickness based friction Reynolds number, and $Re^*_{\rho u}$ is is the momentum boundary layer thickness based semi-local Reynolds number. References for color of lines and symbols are included.

Case	M_e	$-B_q$	Re_τ	Re^*	$t\overline{u}_e/\delta$	$\Delta t\overline{u}_e/\delta$	Color	Ref
M3T5	3.0	0.0	663	2078	143	0.0085		[1]
M5T5	4.9	0.0	648	5297	134	0.0055		[1]
M7T5	6.9	0.0	849	14529	134	0.0154		[1]
M12T5	11.7	0.0	869	54254	142	0.0135		[1]
M10T3	9.1	0.11	691	6790	93	0.0065		[1]
M2H	2.0	0.019	2375	4743	63	0.0064		[2]
M6H	5.86	0.014	2293	24092	63	0.0089		[2]

Chapter 4: Generalized Mean Velocity Transformation

4.1 Motivation

Hypersonic flow is an area of interest that has received much attention by the fluid mechanics community in recent years as we move towards space travel and hypersonic civilian transport vehicles. In particular, a mean velocity transformation for turbulent boundary layer flow that accounts for variations in thermodynamic variables and compressiblity has been sought. The main driver behind such efforts was the suggestion by Morkovin in 1962 "that for moderate Mach numbers, the essential dynamics of these shear flows will follow the incompressible pattern." [10] Based on this hypothesis, it has been hoped that a correct accounting for variation of thermodynamic properties will restore the incompressible law of the wall for wall-bounded compressible flow.

Over the past few decades, various forms of mean velocity transformations (MVT) for CTBLs have been proposed. [12, 13, 35, 38–40], from the pioneering work of Van Driest [12], to the recently proposed viscous stress based transformation by Trettel and Larsson [13], each have had their own limitations. The Van Driest transformation has shown success in scaling adiabatic CTBLs [22, 41–43] with reported weakness in scaling of iso-thermal cases leading to increases in the log-law intercept with increasing heat transfer [13, 31, 40, 44, 45]. The most successful MVT that accounts for the near-wall viscosity gradient was independently developed by Trettel

and Larsson [13] and Patel et al. [40]. However, despite their initial success in isothermal CTBL cases [23,46] with low semi-local Reynolds, Re^*, the scaling remains unsuccessful for cases with increasing Re^* where multiple studies [4, 45] report a large scatter in the log-layer intercept and the slope for such cases.

Recently, Griffin, Fu & Moin [4] developed a total stress based MVT that employs a combination of the viscous stress transformation of Trettel and Larsson [13] and the quasi-equilibrium assumption based transformation of Zhang et al. [35]. They employ a total stress-based functional form to combine these two transformations, such that each is applied in their region of applicability; Trettel and Larsson [13] in the viscous layer and Zhang et al. [35] further from the wall. In their transformation, the quasi-equilibrium model is extended to employ the semi-local wall-normal coordinate, z^*, which was proposed by Huang et al. [17] and has shown to be effective in collapsing turbulence statistics in CTBLs within the near-wall region [4, 13, 22, 40, 44, 45, 88, 90]. Initial explorations of the mean velocity profiles transformed by the GFM approach have shown promising collapse and improvement over earlier MVTs. However there are questions about the breadth of applicability of the quasi-equilibrium hypothesis on which the GFM transformation is partially based. A follow up paper by Bai et al. [91] extended this exploration for a broad range of cases, including high enthalpy turbulent boundary layers, flows at supercritical pressure and boundary layers with pressure gradients, with mixed results, suggesting additional physics must be incorporated under these conditions. The intercept and the slope of GFM transformation as well as the quasi-equilibrium assumption are further examined in the present study for a broader set of semi-local Reynolds numbers.

A few studies have derived MVTs from the momentum equation perspective and this approach deserves further attention. The transformation by Zhang et al. [35] is derived from the

turbulent kinetic energy equation and Wu et al. [39] examined the total stress from the momentum equation perspective to derive their MVT, for example. The latter study, however, relies on Prandtl's mixing length hypothesis [92] for the prediction of the Reynolds stress and requires *a priori* information of the onset locations for the buffer and log layers. Such requirements make the use of their transformation difficult to apply in practice. While relying on the Mach-invariance of the total stress in the momentum equation may be more practical, data show Mach dependence and the breakdown of the near wall momentum balance for CTBLs, as classically described. Namely, for high Re^* number and high Mach number, the turbulent stress is greater than the wall shear stress under Reynolds averaging, albeit slightly [22, 42, 45, 88]. While density fluctuations can be accounted for by employing Favre averaging, this result suggests viscosity fluctuations might need to be considered to appropriately achieve Mach-invariance of the total stress and to derive MVT from the momentum equation perspective.

The current chapter makes use of the CRoCCo CTBL database in table 3.1, which is used to scrutinize the effects of Mach and Reynolds numbers on CTBL flows. These effects are examined in the context of the thin shear layer momentum approximation, which we modify from its classical form to represent the data across the parameter space. After the relative importance of density and viscosity fluctuation effects is analyzed, we integrate the new findings into a mean velocity transformation that enables the collapse of data across a wide range of CTBL conditions.

4.2 Density and Viscosity Fluctuations in Compressible Boundary Layers

4.2.1 Breakdown of the Classical Momentum Balance

To probe influences of compressibility on thermodynamic property fluctuations within compressible turbulent boundary layers, we begin by examining the Reynolds-averaged, thin shear layer (TSL) stream-wise momentum equation. While it is customary to use Favre-averaged equations in compressible flow, the use of the Reynolds-averaged equation provides insights into the influence of fluid property variations in compressible turbulence that are rarely remarked upon. We begin by employing the classical assumptions that the stream-wise derivatives are negligible, the fluctuations of thermodynamic variables are small, the pressure gradient across the boundary layer is small and the magnitude of convection terms are negligible near the wall. Under these conditions, the momentum equation reduces to,

$$1 \simeq \frac{\overline{\mu}}{\tau_w}\frac{\partial \overline{u}}{\partial z} - \frac{\overline{\rho u'w'}}{\tau_w} = \tau^+_{V-R} + \tau^+_{T-R} \tag{4.1}$$

where the superscript "+" denotes the non-dimensionalization by wall quantities, and τ^+_{V-R} and τ^+_{T-R} are the non-dimensional Reynolds-averaged viscous and turbulent stresses, respectively. The classical momentum balance described by Eq.4.1 is expected to hold near the wall for zero pressure gradient boundary layers if Morkovin's hypothesis is valid; that is, the density and viscosity fluctuations are negligible and the consideration of only mean density and mean viscosity is sufficient to restore the classical near wall momentum balance observed in ITBLs.

The stress balance and the magnitude of its classic viscous and turbulent contributions

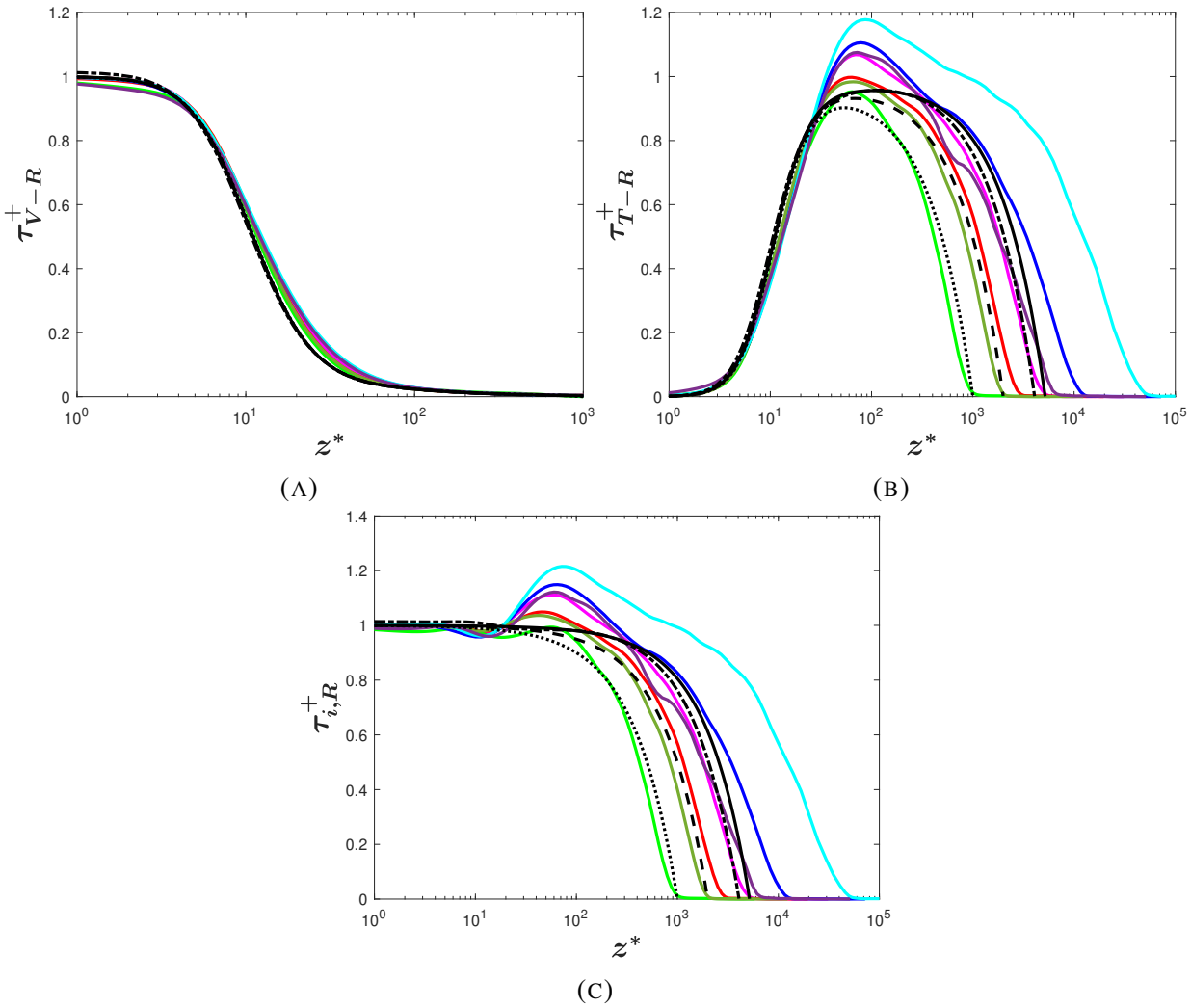

FIGURE 4.1. Non-dimensionalized (A) viscous stress, τ^+_{V-R}, (B) turbulent stress, τ^+_{T-R}, (C) total stress, $\tau^+_{i,R}$, are plotted against the semi-local wall normal coordinate, z^*. Corresponding stresses from ITBL flow references are included for comparison. References for lines colors and styles as well as references for the database are included in Table 3.1 and 3.3

is considered in Fig. 4.1 where $\tau^+_{i,R} = \tau^+_{V-R} + \tau^+_{T-R}$ denotes the non-dimensionalized total stress. The subscript 'R' is used to denote the use of Reynolds-averaging. As expected for the incompressible cases, the classical momentum balance holds in the near-wall region, where the incompressible total stress in Fig. 4.1c is seen to be very close to one. In contrast, the balance is not observed for many CTBL datasets, which is most clearly demonstrated by the turbulent shear stress achieving magnitudes of up to 1.2 times the wall shear stress (see Fig. 4.1b). This overshoot in the wall shear stress has been observed in a number of previous compressible wall-bounded studies [22, 42, 45, 88], suggesting a violation of the underlying assumptions inherent in the classical near-wall momentum balance described by Eq.4.1.

Extending the TSL Reynolds averaged momentum equation to include terms involving density and viscosity fluctuations, we can arrive at Eq. 4.2. The details of the derivation of TSL Reynolds averaged momentum equation with thermodynamic property fluctuation is included in Appendix A.

$$1 = \tau^+_{V-R} + \tau^+_{T-R} + \left(\frac{-\overline{u}\overline{\rho' w'} - \overline{w}\overline{\rho' u'} - \overline{\rho' u' w'}}{\tau_w}\right) + \left(\frac{\overline{\mu' \frac{\partial u'}{\partial z}}}{\tau_w}\right) \tag{4.2}$$

which involves three additional non-dimentionalized density fluctuation terms and one more viscosity fluctuation term. In particular, $\overline{w}\overline{\rho' u'}$ and $\overline{u}\overline{\rho' w'}$ are of special interest. The magnitude of the two terms is compared in Fig. 4.2 relative to the wall shear stress for the M5T1 and M12T5 cases. These cases have been selected as they are representative of the range of these terms in this dataset. The $\overline{u}\overline{\rho' w'}$ term is seen to be much larger than $\overline{w}\overline{\rho' u'}$ and can even be as large as three times the wall shear stress at $z^* = 100$. However, we also observe in Fig. 4.2a that $\overline{w}\overline{\rho' u'}$ accounts for 2% to 10% of wall shear stress for M5T1 and M12T5 case, respectively, and cannot

be neglected as has traditionally been assumed (see Spina et al. [32]).

The large magnitude of $\overline{u}\overline{\rho' w'}$ shown in Fig. 4.2b is challenging, however, because it is so large in some parts of the layer that its inclusion as a term in the near-wall stress balance of Eq. 4.2 would cause the right hand side of Eq. 4.2 to increase significantly above the value of the wall shear stress outside of the near-wall region; significantly different behavior and trends than observed in Fig 4.1. However, Fig. 4.2c reveals that $\overline{u}\overline{\rho' w'} d\overline{w}/dx$, a corresponding turbulent kinetic energy (TKE) term to $\overline{u}\overline{\rho' w'}$, is orders of magnitude smaller than $\overline{w}\overline{\rho' u'} d\overline{u}/dz$, a corresponding TKE term to $\overline{w}\overline{\rho' u'}$, suggesting that despite the large magnitude of $\overline{u}\overline{\rho' w'}$ in Eq.4.2, its role in the transport of turbulent kinetic energy is limited and thus, its role in the transport of turbulent momentum is limited as well. The above TKE transport argument closely follows that of Spina et al. [32]. In support of the $\overline{u}\overline{\rho' w'}$ term's limited role in the transport of turbulent momentum, Spina et al. [32] observed that terms important to the production of turbulent kinetic energy are two orders of magnitude greater than the TKE production term due to $\overline{u}\overline{\rho' w'}$. In addition, they interpreted $\overline{u}\overline{\rho' w'}$ as the "mean rate of transfer of turbulent mass flux" across a plane normal to the z-direction and asserted that this fictitious stress term does not involve the transport of turbulent momentum across the same plane. Based on these discussions, the role of $\overline{u}\overline{\rho' w'}$ in the turbulent momentum transport is determined to be minimal despite its large magnitude.

Another approach to examine the treatment of $\overline{u}\overline{\rho' w'}$ explores the near-wall momentum equation prior to neglecting convective terms, as seen in Eq. 4.3 (essentially a precursor to Eq.

4.2.)

$$\underbrace{\frac{d}{dz^*}\left[\frac{\overline{\rho}\,\overline{u}\,\overline{w}+\overline{u}\overline{\rho' w'}}{\tau_w}\right]}_{\simeq 0} = \frac{d}{dz^*}\left[\left(\overline{\mu}\frac{d\overline{u}}{dz} - \overline{\rho}\overline{u'w'} + \left(-\overline{w}\overline{\rho' u'} - \overline{\rho' u' w'}\right) + \left(\overline{\mu'\frac{\partial u'}{\partial z}}\right)\right)/\tau_w\right] \quad (4.3)$$

The left hand side of Eq. 4.3 is plotted in Fig. 4.3a. It can be observed that, for both M5T1 and M12T5 cases, which are representative of the range of this term in this dataset, the left hand side of Eq. 4.3 remains close to zero through much of the layer. Moreover, it can be shown that the difference between $\overline{\rho}\,\overline{u}\,\overline{w}+\overline{u}\overline{\rho' w'}$ and $\overline{\rho}\tilde{u}\tilde{w}$ is shown to be minimal (Fig. 4.3b), suggesting that $\overline{\rho}\,\overline{u}\,\overline{w}+\overline{u}\overline{\rho' w'}$ is similar to the Favre averaged convection term, which is neglected in the near-wall TSL form of the Favre momentum equation. Following Morkovin, Spina et al. [32] also suggested that it is possible to refactor $\overline{u}\overline{\rho' w'}$ and $\overline{\rho}\,\overline{u}\,\overline{w}$ as a product of the average instantaneous mass flux and a strain, and separate the terms important to the turbulent momentum transport. Our analysis mimics this approach. We note that $\overline{u}\overline{\rho' w'}$ would not have appeared in Eq, 4.2 if the refactoring operation of Spina et al. was performed prior to applying near-wall assumptions. However, we have chosen to discuss the mathematical treatment of $\overline{u}\overline{\rho' w'}$ and $\overline{\rho}\,\overline{u}\,\overline{w}$ to examine the effect of compressiblity arising from the density fluctuation when employing Reynolds averaging. In contrast, we choose to retain $\overline{w}\overline{\rho' u'}$. Spina et al. [32] neglected this term by arguing that its magnitude within the momentum equation was small in many cases. We have demonstrated in Fig. 4.2a that $\overline{w}\overline{\rho' u'}$ is non-negligible for our dataset, which includes high Mach and Re* cases and thus choose to retain the term going forward.

The result is Eq.4.4, which now involves two non-dimentionalized density fluctuation terms

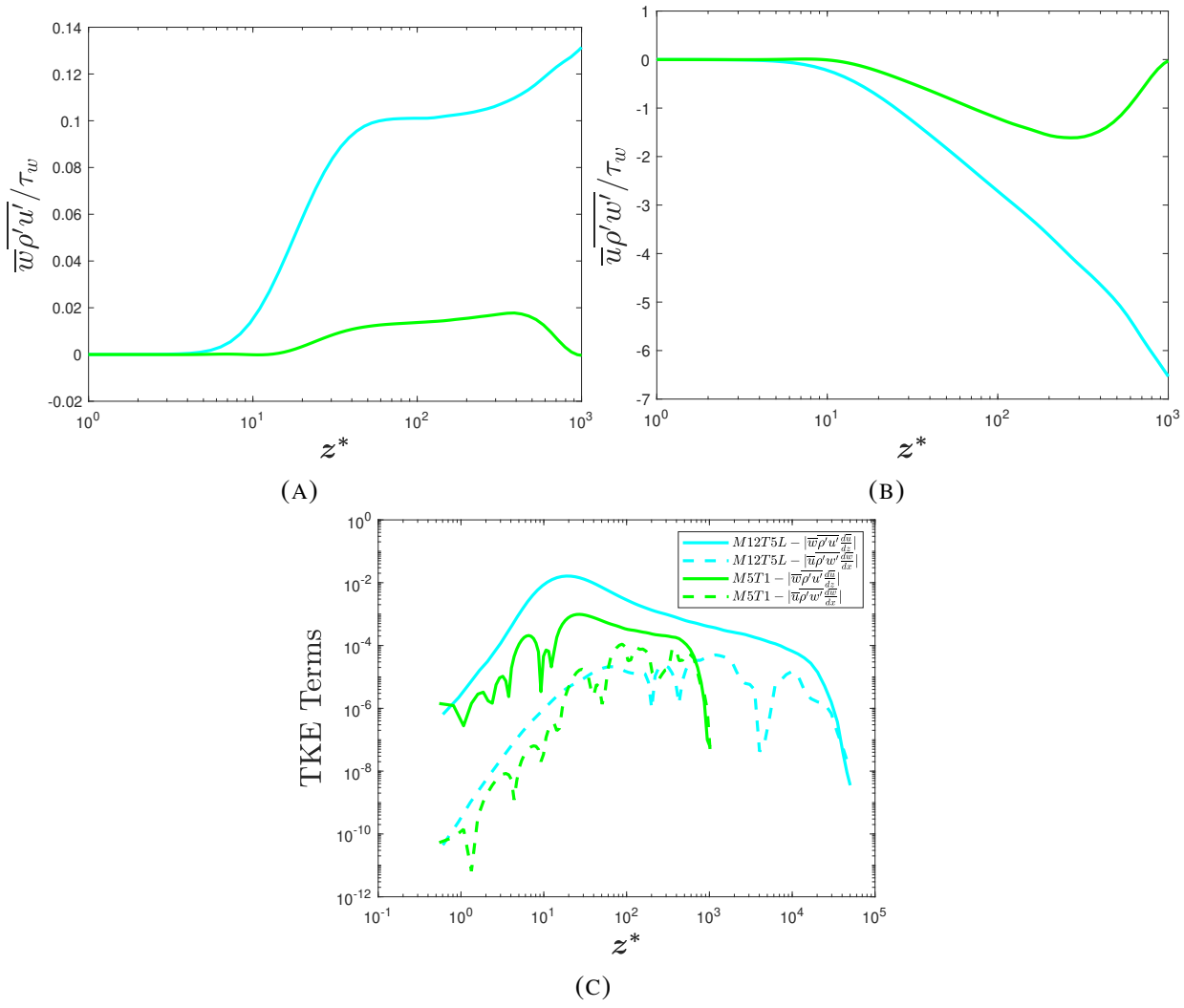

FIGURE 4.2. Comparison of (A) $\overline{w}\overline{\rho' u'}/\tau_w$ and (B) $\overline{u}\overline{\rho' w'}/\tau_w$ for M5T1 and M12T5. (C) Comparison of the magnitudes of the TKE terms corresponding to $\overline{w}\overline{\rho' u'}$ and $\overline{u}\overline{\rho' w'}$. All TKE terms are normalized by $\overline{\rho} u_\tau^{*3}/z_\tau^*$ where $u_\tau^* = u_\tau\sqrt{\rho_w/\overline{\rho}}$ and $z_\tau^* = \overline{\mu}/\overline{\rho} u_\tau\sqrt{\rho_w/\overline{\rho}}$. References for line colors and symbols are included in Table 3.1.

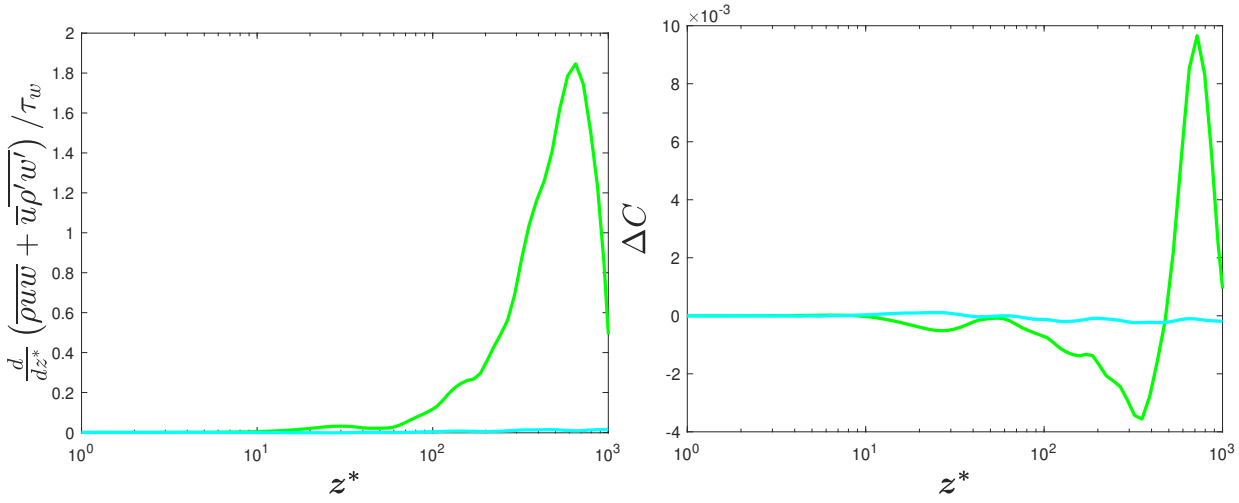

(A) (B)

FIGURE 4.3. (A) Left hand side of Eq.4.3, $\frac{d}{dz^*}\left[\overline{\rho u w}+\overline{u}\overline{\rho' w'}\right]/\tau_w$. (B) Difference between $\overline{\rho}\tilde{u}\tilde{w}$ and $\overline{\rho}\,\overline{u}\,\overline{w}+\overline{u}\overline{\rho' w'}$ normalized by τ_w, where $\Delta C = \overline{\rho}\tilde{u}\tilde{w}/\tau_w - \left(\overline{\rho}\,\overline{u}\,\overline{w}+\overline{u}\overline{\rho' w'}\right)/\tau_w$. References for line colors are included in Table 3.1.

and one viscosity fluctuation term that we group as $\zeta^+_{\rho-R}$ and $\zeta^+_{\mu-R}$, respectively.

$$1 = \tau^+_{V-R} + \tau^+_{T-R} + \left(\underbrace{\frac{-\overline{w}\overline{\rho' u'} - \overline{\rho' u' w'}}{\tau_w}}_{\zeta^+_{\rho-R}}\right) + \left(\underbrace{\frac{\overline{\mu' \frac{\partial u'}{\partial z}}}{\tau_w}}_{\zeta^+_{\mu-R}}\right) \tag{4.4}$$

Terms included in $\zeta^+_R = \zeta^+_{\rho-R} + \zeta^+_{\mu-R}$ represent the influence of fluctuating thermodynamic properties on the total streamwise stress balance in the Reynolds-averaged momentum equation. These terms are explored in Fig. 4.4. Interestingly, the magnitude of ζ^+_R exceeds 4% for all cases considered in this study, including those at Mach 3, suggesting that thermodynamic property fluctuations should be considered in the analysis of the near-wall momentum balance of most CTBLs. Noticeably, the magnitude of the first peak in Fig. 4.4a, which is located at the lower edge of the log layer, indicates that ζ^+_R ranges from 4% to 22% of the wall shear stress for this dataset. The magnitude of $\zeta^+_{\mu-R}$ in Fig. 4.4b is a non-negligible proportion of this, with $\zeta^+_{\mu-R}$

ranging from -1.5% to 2.5% in the viscous layer. Note that the magnitude of the density and viscosity fluctuation effect will depend on the averaging method used and, as we will see in a subsequent section, the viscosity fluctuation proportion of the total stress is larger under Favre averaging. Not surprisingly, when the total stress with the thermodynamic property fluctuations, $\tau_R^+ = \tau_{V-R}^+ + \tau_{V-R}^+ + \zeta_R^+$, is plotted as shown in Fig. 4.4d, the near-wall momentum balance expected from the incompressible theory is restored, supporting an inclusion of $\overline{w}\overline{\rho' u'}$ while not including $\overline{u}\overline{\rho' w'}$.

We thus conclude that density and viscosity fluctuations must be considered for an accurate statement of momentum balance. This influence is reduced for hypersonic datasets at low Reynolds numbers or with significant heat transfer. At low Reynolds numbers the viscous stress is a greater contribution of the total stress in the near-wall region, leading to peak turbulent stresses, τ_{T-R}^+, that are less likely to exceed the wall shear stress, masking the fluctuating density and viscosity influences. We shall see below that employing Favre averaging effectively accounts for density fluctuations but not those of viscosity. Another consequence is that $\overline{\rho}\overline{u'w'}$ and $\overline{\mu}\partial\overline{u}/\partial z$ are not equal to $\overline{\rho u' w'}$ and $\overline{\mu \partial u/\partial z}$, respectively, as is often assumed, because fluctuations in the thermodynamic properties are not negligible.

4.2.2 The Role and Mechanism of Density and Viscosity Fluctuations

The role of $\zeta_{\rho-R}^+$ is evaluated by first considering the turbulent shear stress, τ_{T-R}^+. It is well known that τ_{T-R}^+ results in mixing. When the wall-normal velocity fluctuation, w', is positive, lower momentum from closer to the wall is brought into a higher-momentum region further from the wall. This often causes a negative streamwise velocity fluctuation, resulting in a negative

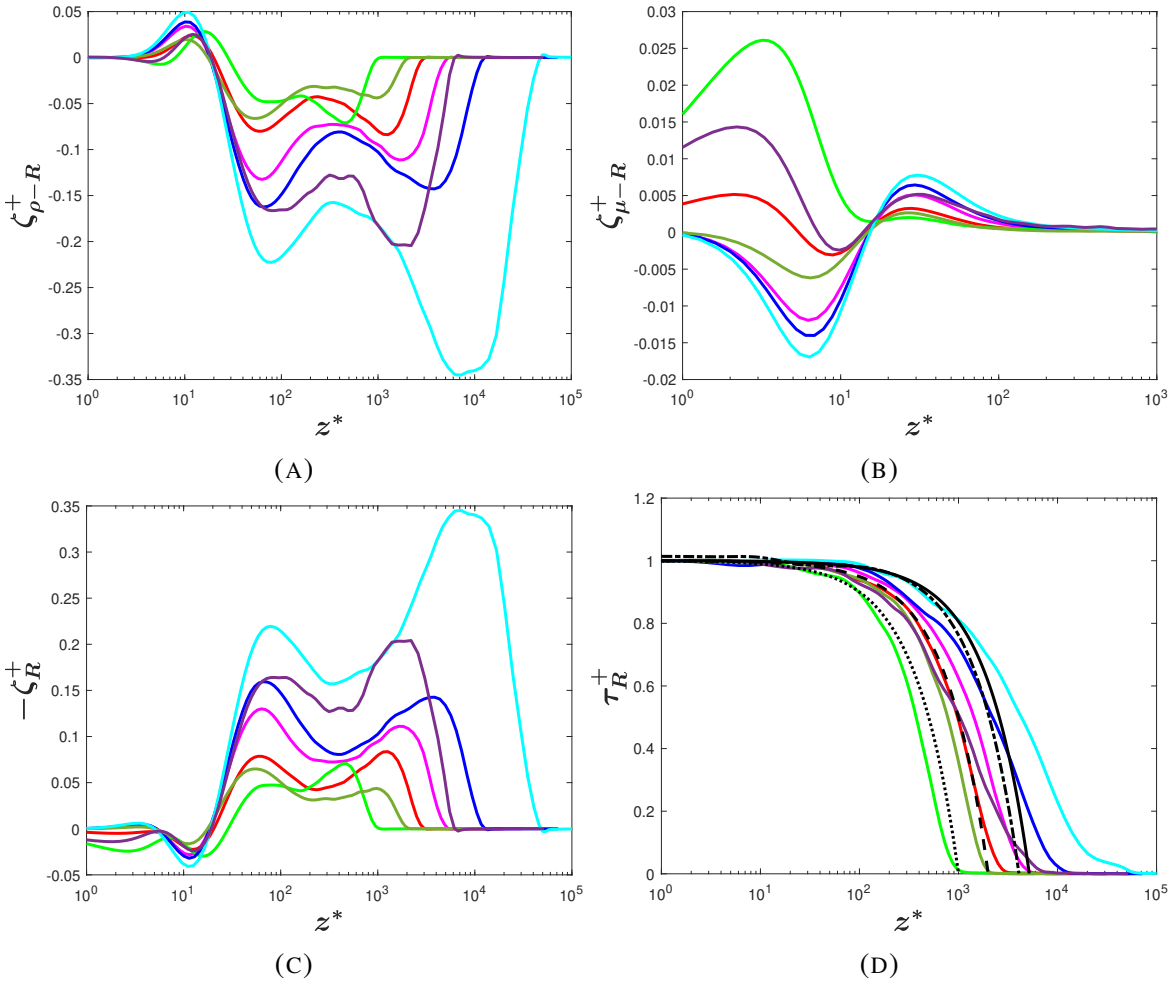

FIGURE 4.4. (A) Sum of density fluctuating term, $\zeta^+_{\rho-R}$, (B) Sum of viscosity fluctuating terms, $\zeta^+_{\mu-R}$, (C) Sum of the density and viscosity fluctuation terms, ζ^+_R, versus semi-local wall normal coordinate, z^*. (D) Density and viscosity fluctuation corrected Reynolds-averaged total stress, τ^+_R. References for line colors and styles as well as references for the database are included in table 3.1.

$\overline{u'w'}$, on average. The opposite occurs for the case of negative w', and thus the resulting τ^+_{T-R} is also negative. On the other hand, the role of the density fluctuation term, $\zeta^+_{\rho-R}$, is the opposite, on average. Plotted in Fig.4.4a, negative $\zeta^+_{\rho-R}$ suggests that the net effect of $\overline{w}\overline{\rho'u'} + \overline{\rho'u'w'}$ is positive in the bulk of the buffer layer and the log layer, and thus $\zeta^+_{\rho-R}$ counteracts the influence of the turbulent mixing. The suggested interpretation is therefore that the fluid inertia opposes the turbulent mixing.

While the role of density fluctuations is consistent for all CTBL cases, we find that the role of the viscosity fluctuation terms is different for adiabatic and non-adiabatic cases. For adiabatic cases, Fig. 4.4b demonstrates that $\zeta^+_{\mu-R}$ is negative, and that the main effect of the viscosity fluctuations is to oppose the turbulent mixing. For the cold wall cases, $\zeta^+_{\mu-R}$ is positive for $z^* < 5$, which indicates that $\zeta^+_{\mu-R}$ enhances viscous deceleration, thus counteracting the effect of density fluctuations before dropping to zero in the log layer.

Before continuing our analysis, we note that the compressibility influences of pressure fluctuations as well as dilatational velocity fluctuations on hypersonic boundary layer dynamics have also been examined and become a source of great interest in recent years [93, 94]. The study of Duan et al. [93] focuses on the role of the pressure fluctuation in an interaction with freestream acoustic field, for example. And the study of Yu et al. [94] examines the effect of dilatational velocity fluctuations on the wall shear stress. Our data suggests that pressure fluctuation magnitudes vary significantly across the current datasets. While linkages undoubtedly exist between pressure, density and viscosity fluctuations, we choose to restrict the current exploration to the influences of thermodynamic variable fluctuations on the near-wall stress balance, leaving additional interesting avenues of study involving pressure for future study.

4.2.3 Generalized Favre-Averaged Momentum Balance Equation

The growing influence of density fluctuations with higher Mach numbers is known but not usually discussed in this context. It is also one reason that Favre averaging has been preferred for compressible flows. It involves scaling a quantity of interest by the instantaneous density (i.e. $\tilde{f} = \overline{\rho f}/\overline{\rho}$). As a result, the Favre-averaged implementation accounts for fluctuations in density since,

$$\overline{\rho}\widetilde{u''w''} = \overline{\rho u''w''} = \overline{(\overline{\rho} + \rho')\, u''w''}. \tag{4.5}$$

We can therefore write the the near-wall Favre-averaged momentum equation, employing thin shear layer assumptions and including all fluctuations in thermodynamic properties as

$$1 = \frac{\left(\overline{\mu}\frac{\partial \tilde{u}}{\partial z} - \overline{\rho}\widetilde{u''w''}\right)}{\tau_w} + \left(\underbrace{\frac{\overline{\overline{\mu}\frac{\partial u''}{\partial z}} + \overline{\mu'\frac{\partial u''}{\partial z}}}{\tau_w}}_{\boldsymbol{\zeta_\mu^+}}\right) = \left(\underbrace{\tau_V^+ + \zeta_\mu^+}_{\tau_{VG}^+}\right) + \tau_T^+. \tag{4.6}$$

In this equation, $\overline{\mu}\frac{\partial \tilde{u}}{\partial z}/\tau_w$ is the conventional form of the Favre-averaged viscous stress, τ_V^+, $\overline{\rho}\widetilde{u''w''}/\tau_w$ is the conventional form of the Favre-averaged turbulent stress, τ_T^+, and ζ_μ^+ is the influence arising from viscosity fluctuations. Note that we have employed Reynolds averaging decomposition for the viscosity, as is most common. However, using Favre-averaged decomposition of viscosity, following Spina et al. [32], does not change our conclusions as long as all terms, including terms arising from the viscosity fluctuations, are accounted for. The details of the derivation of Eq. 4.6 are included in Appendix A. In the following analysis, we define τ_{VG}^+ to be equal to $\tau_V^+ + \zeta_V^+$ where the subscript G is used to denote its generality. While viscosity fluctuations are not normally considered in the conventional Favre-averaged momentum equation due

to the use of the Strong Reynolds Analogy [10], we demonstrate that viscosity fluctuations have a non-negligible influence on the near-wall momentum balance in Fig. 4.5a and are larger than the corresponding viscous fluctuation term within the Reynolds-averaged equation.

The conventional Favre-averaged stress terms, including thermodynamic fluctuations, are plotted in Fig. 4.5. For all cases, the Favre-averaged total stress ,defined as $\tau^+ = \tau^+_{VG} + \tau^+_T$ in Fig. 4.5d, remains equal to the wall shear stress (i.e. a value of 1 when nondimensionalized) in the inner layer, deviating at higher z^* for higher Re^*, as is the case for ITBLs. Critically, for all CTBL cases considered, we observe a level of Mach-invariance in the total stress, τ^+, that is enforced by the near-wall momentum balance. This result suggests the possible use of the generalized total stress balance for the derivation of a generalized MVT. The comparison of Favre and Reynolds-averaged turbulent shear stresses (τ^+_T in Fig. 4.5d and τ^+_{T-R} in Fig. 4.1b) reveals significant improvements due to the consideration of density fluctuations inherent in the use of Favre-averaging. The resulting turbulent shear stresses are seen to behave quite similarly to the incompressible profiles of Modesti and Pirozzoli [46]. Best comparisons are seen to occur when the compressible Re^* is matched to the incompressible Re_τ (i.e. M5T1 is compared to LM1000, M3T5, M3Ad, and M5T3; M5T5 is compared to LM2000, M10T3, and M7T5-L; and M12T5-L is compared to LM5200). For all cases, the turbulent stress remains below, but close to, a value of one, consistent with the incompressible theory.

The magnitude of ζ^+_μ in Fig. 4.5a indicates that τ^+_{VG} in Fig. 4.5b would deviate significantly from the wall shear stress and the ITBL trend for $z* < 5$ if viscosity fluctuations were not taken into account. Moreover, the role of viscosity fluctuations remains unchanged, as discussed in section III-B in relation to $\zeta^+_{\mu-R}$. The increased magnitude of ζ^+_μ, however, suggests that ζ^+_μ is even more critical to the overall stress balance under the Favre-averaging definition. Interestingly,

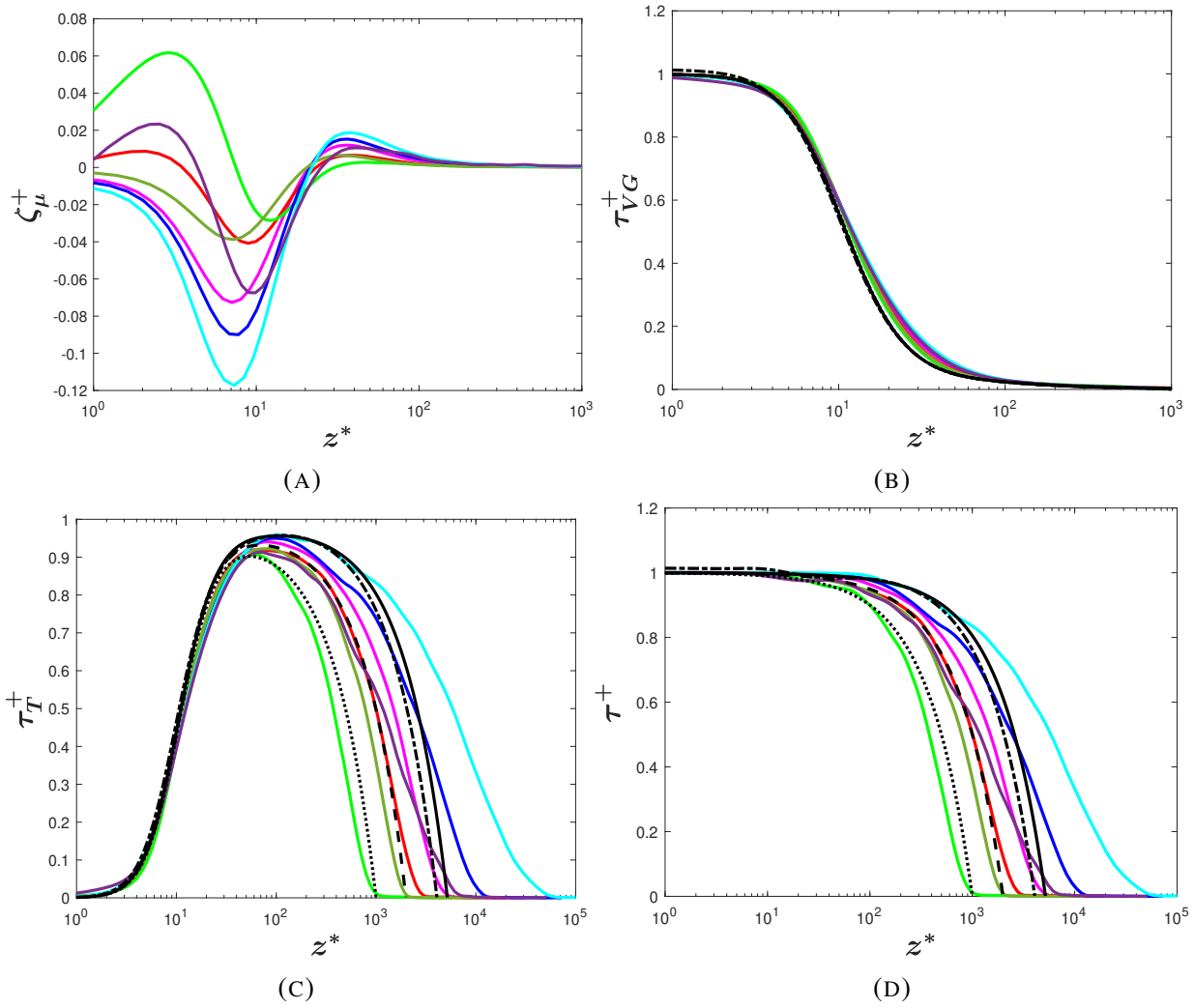

FIGURE 4.5. Non-dimensional, Favre-averaged (A) viscosity fluctuation terms, ζ_μ^+ (B) viscous stress, $\tau_{VG}^+ = \tau_V^+ + \zeta_\mu^+$ (C) Turbulent Stress,τ_T^+, and (D) total stress,τ^+ are plotted against the semi-local wall normal coordinate, z^*. Corresponding stresses from ITBL flow references are plotted for comparison. References for line colors and styles as well as references for the database are included in table 3.1 and 3.3.

for both ζ_{μ}^{+} and $\zeta_{\mu-R}^{+}$, the effect of viscosity fluctuations can remain relevant up to $z^{*} = 30$ (especially for adiabatic cases) before dropping to smaller values outside of the buffer layer. Given the discussion above, it is perhaps not surprising that accounting for density and viscosity fluctuations restores the expected characteristics of the total stress which exhibits good collapse across the ITBL and CTBL data as shown in Fig.4.5d.

The stress characteristics discussed above will be used to formulate a new MVT for CTBLs and a few observations important to the following derivation must be reiterated. When all thermodynamic properties important to zero pressure gradient CTBLs are accounted for, namely the mean property gradients as well as density and viscosity fluctuations, the Mach-invariance of the total stress, τ^{+} is enforced by the near wall momentum balance. Moreover, for CTBLs, the degree of Mach-invariance for the viscous and turbulent stresses is significantly improved with the new formulations, indicating that the relative contributions from the viscous and turbulent stresses to the total stress remain relatively Mach-invariant in the inner layer. These important observations suggest that there are two types of Mach invariance embedded within τ^{+}, namely: (1) the Mach-invariance of the generalized near-wall total stress formulation and (2) the Mach-invariance of the relative contributions from the generalized viscous and turbulent stresses to the total stress formulation.

4.3 Total Stress Based Velocity Transformations

In recent months, a new MVT based on total stress has been proposed by Griffin, Fu & Moin [4]. Mean velocity profiles based on their transformation are shown in Fig. 4.6a, exhibiting a good collapse to the incompressible law of the wall. Success of this transformation is attributed

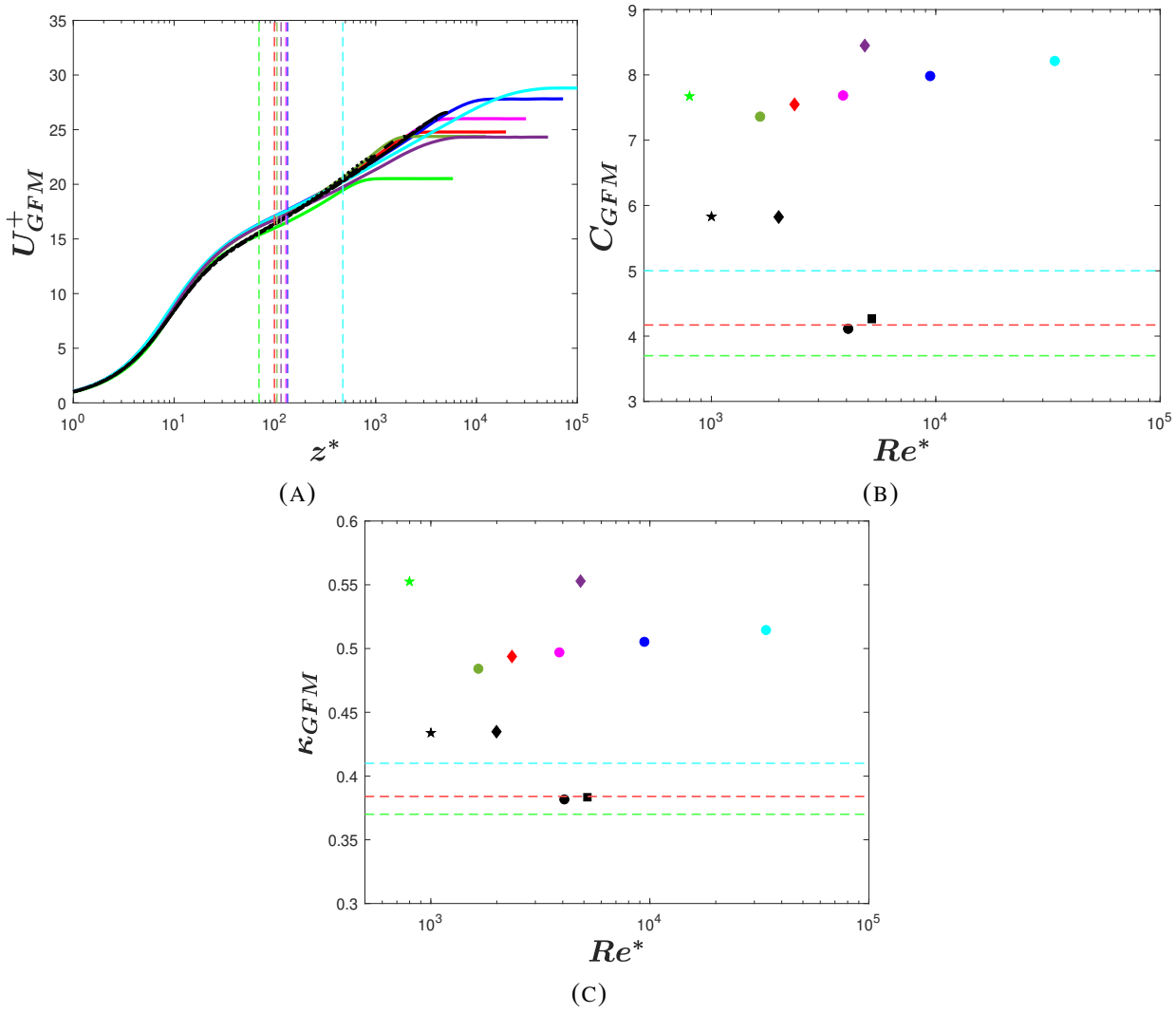

FIGURE 4.6. (A) GFM velocity transformation versus semi-local wall normal coordinate, z^*. (B) Intercept and (C) Von Kármán Constant, κ, of GFM profiles as a function of semi local Reynolds Number, Re^*. Classical incompressible law of the wall velocity profiles, intercepts and κ of the log layer calculated from the incompressible channel flow database are included for comparison. References for colors and styles of lines and symbols as well as references for the CTBL and ITBL database are included in table 3.1 and 3.3 unless otherwise noted hereafter. The vertical dashed lines in (A) indicate the wall normal coordinate at which the intercept and κ were calculated (Colors match the corresponding CTBL cases with the reference to the colors in table 3.1). The horizontal dashed lines in (B) and (C) indicate variability in the intercept and κ, respectively, reported in [95], [dashed cyan line-superpipe, dashed red line- boundary layer, dashed green line-channel].

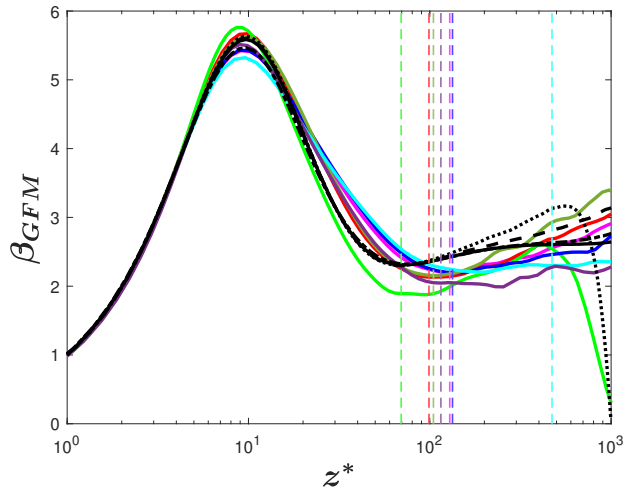

FIGURE 4.7. Pre-multiplied mean shear, β_{GFM}, based on GFM transformation versus semi-local wall normal coordinate. Pre-multiplied mean shear of LM5200 and BOP4100 is calculated from the classical incompressible law of the wall velocity profile and plotted as incompressible reference for comparison. The references for line colors and styles as well as the references for the database are included in table 3.1 and 3.3 unless otherwise noted hereafter. The vertical dashed lines indicate the wall normal coordinate at which the log layer parameters were calculated (Colors match the corresponding CTBL cases with the reference to the colors in table 3.1). The dashed grey lines are publicly available CTBL database of Zhang et al. [45].

to the use of a total-stress-based balance to combine the viscous stress-based transformation by Trettel & Larsson [13] and the quasi-equilibrium-based transformation of Zhang et al. [35] at locations where the assumptions underlying each transformation are valid. The mathematical form of the total-stress-based transformation can be derived from the total stress representation of the mean shear, resulting in,

$$\tau^+ = S_t^+ \left(\frac{\tau_V^+}{S_{TL}^+} + \frac{\tau_T^+}{S_{eq}^+} \right) \tag{4.7}$$

where $S_{TL}^+ = \overline{\mu}^+ \partial \tilde{u}^+ / \partial z^+$ denotes non-dimensinalized mean shear transformed according to Trettel & Larsson [13] and $S_{eq}^+ = (1/\overline{\mu}^+) \partial \tilde{u}^+ / \partial z^*$ denotes the non-dimensionalized mean shear of Zhang et al. [35] generalized by Griffin, Fu & Moin [4] to semilocal wall units, z^*. This result

can then be rearranged to obtain,

$$S_t^+ = \frac{\tau_T^+ S_{eq}^+}{\tau^+ + S_{eq}^+ - S_{TL}^+}. \tag{4.8}$$

Once calculated, the resulting transformed, non-dimensional shear stress, $S_t^+ = \partial U_{GFM}^+ / \partial z^*$, can the be integrated to obtain the transformed velocity velocity profile, U_{GFM}^+. Note that they employ Favre averaged variables, accounting for density but not viscous fluctuations.

In the study of Griffin et al. [4], they utilize a CTBL database with Re^* approximately ranging from 200 to 4900 and Mach number ranging from 2 to 14. They present the integrated error of the transformed mean velocity profile relative to the conventional incompressible log-law. The database of the current study allows us to test the GFM transformation over a wider range of Re^*, including a range of diabatic conditions (see table 3.1). Following Griffin et al. [4], comparisons are made with the incompressible cases of Lee & Moser [52] and Bernardini and Pirozzoli [85] (see Table 3.3). The LM5200 ITBL was used by Griffin et al. [4] for their incompressible law of the wall baseline.

In contrast to Griffin et al. we choose to examine the influence of the transformation on the variation in slope and intercept of the log layer. These parameters are determined using the pre-multiplied mean shear as suggested by Lee & Moser [52], given by $\beta = z^* dU_t^+ / dz^*$, where U_t^+ is a transformed mean velocity of interest. If there is a logarithmic layer, the pre-multiplied mean shear will have a plateau, or constant-valued region. To determine the location of the plateau (or best approximation to a plateau should a plateau not fully exist) $d\beta/dz^*$ is calculated from $z^* = 30$ to $z/\delta = 0.2$, where δ is the wall normal coordinate at the location where mean velocity is 99% of the freestream value. The z^* location at the minimum value of $d\beta/dz^*$ is used as

the "characteristic location" for the log layer and the location at which a slope and intercept are calculated. This location is thus not dependent on the chosen bounds of the search.

The log layer intercept and slope for the current CTBL database under the GFM transformation are shown in Fig. 4.6b and Fig. 4.6c, where C is the intercept and κ is 1/slope or the Kármán constant. The calculated "characteristic locations" of the logarithmic portion of each profile are also shown in Fig. 4.6a. Also shown are reference ITBL log-law characteristics and the variability of ITBL slope and intercept reported in the literature by Nagib & Chauhan [95]. The slope and intercept derived from the GFM transformation of the current compressible datasets lie outside the range of values commonly reported for ITBLs for higher Reynolds numbers. Both κ and intercept are seen to be larger under this transformation. The slope and intercept are also larger than the low Reynolds number incompressible cases of cases of Lee and Moser [52]. In an attempt to improve the GFM transformation results, we have tested a version of the transformation where τ^+_{VG} was used to replace τ^+_V, in an effort to account for the influence of viscosity fluctuations on the near-wall stress balance. This test did not show an appreciable improvement to slope or intercept values and thus viscous fluctuations are not the source of the observed disparity between the incompressible log-law and GFM transformed results. A further examination of the pre-multiplied mean shear, which is plotted in Fig. 4.7, suggests that the collapse for the GFM mean velocity profile in Fig. 4.6a is observed because Mach-invariance of the pre-multiplied mean shear is somewhat satisfactory up to $z^* = 20$ in the middle of the buffer layer. However, the Mach-invariance of β_{GFM} quickly deteriorates in the region at $z^* > 20$ where the quasi-equilibrium model starts to represent the turbulent stress. This incomplete Mach-invariance extends to the plateau region, where it is expected to show the most logarithmic behavior, resulting in incorrect intercepts and slopes within the log layer region. This observation, which points to the log layer

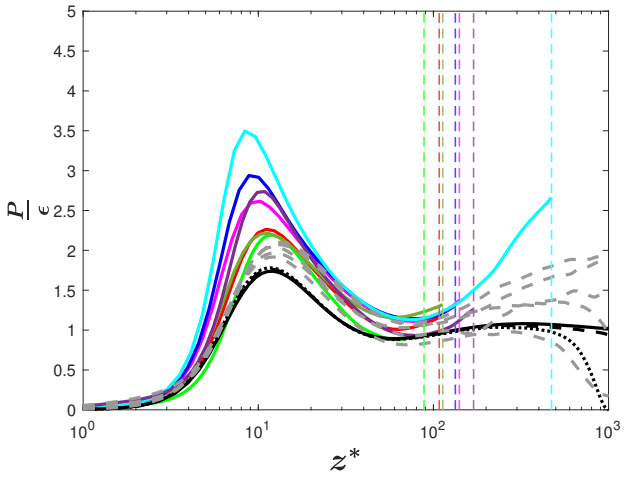

FIGURE 4.8. The ratio of the TKE production (P) and the viscous dissipation (ϵ) versus semi-local wall normal coordinate, z^*. The vertical dashed lines indicate the wall-normal coordinate at which the log layer parameters were calculated. Grey dashed lines are CTBL data from Zhang et al. [45]. References for line colors and styles as well as the references for the database are included in table 3.1 unless otherwise noted.

as the source of the error, is perhaps an explanation as to why the use of τ^+_{VG} showed negligible improvement. While higher Re^* cases show larger regions of logarithmic behavior, it is unclear if the correspondence of slope and intercept with incompressible data will improve significantly for the CTBLs at some combination of high Re^* or Re_τ. Despite this, we should note that the GFM transformation does provide a better collapse of the compressible profiles than most previously proposed MVTs.

We further examine the reasons for the above variability of slope and intercept by exploring the validity of the assumptions undertaken in the derivation of the transformation by Zhang et al. [35], namely the Mach-invariance of (1) the Favre-averaged enstrophy, (2) the near-wall turbulent stress profile, and (3) of the ratio of the Favre-averaged turbulent kinetic energy production and viscous dissipation terms. For brevity in this section, Einstein notation is used to express the terms pertaining to the TKE equation, where the definition of v is the velocity in the direction determined by the indices, i,j and k.

While not shown here, it is confirmed that the Mach-invariance of the Favre-averaged enstrophy suggested by Lagha et al. [42] holds for the current CTBL cases. Recall also that the turbulent stress in Fig. 4.5c is Mach-invariant in the log layer when employing Favre averaging. Finally, we explore the ratio of the Favre-averaged TKE production and the Favre-averaged viscous dissipation, mathematically given by

$$P = \overline{\rho} \widetilde{v_i'' v_j''} \frac{\partial \widetilde{v}_i}{\partial x_j} \tag{4.9}$$

$$\epsilon = \overline{\mu \left(\frac{\partial (\tilde{v} + v'')_i}{\partial x_j} + \frac{\partial (\tilde{v} + v'')_j}{\partial x_i} - \frac{2}{3} \delta_{ij} \frac{\partial (\tilde{v} + v'')_k}{\partial x_k} \right) \frac{\partial v_i''}{\partial x_j}}. \tag{4.10}$$

Similar to the Favre-averaged turbulent stress, the Favre averaged TKE production term accounts for density fluctuations by Favre-averaging definition, and the TKE dissipation is defined to include viscosity fluctuations by explicitly using the instantaneous viscosity. The ratio of the TKE production (P) and viscous dissipation (ϵ) terms is plotted in Fig. 4.8. The Mach-invariance deteriorates in the viscous and buffer layers where it is not expected hold [35], while the Mach-invariance improves in the log layer where collapse is more expected. Despite this, an observation of the P/ϵ ratio from our CTBL datasets as well as the CTBL data from Zhang et al. [45] suggests that it remains unclear whether the quasi-equilibrium assumption exhibits sufficient Mach-invariance to form the basis for a velocity transformation in the log layer region.

4.4 Proposed new total stress-based transformation

In an effort to develop a generalized MVT for CTBL, we revisit the total stress representation in Eq. 4.7 by Griffin, Fu & Moin [4]. They represent the total stress in terms of mean shear quantities, S_t^+, S_{TL}^+ and S_{eq}^+. By construction, S_t^+ will exhibit the characteristics of either S_{TL}^+ in the near-wall limit, or of S_{eq}^+ in the log layer. More importantly, Eq. 4.7 preserves the magnitude of the total stress prescribed by the viscous and the turbulent stresses. Therefore, we propose several modifications to Eq. 4.7 to utilize the scaling properties of τ^+ identified earlier: (1) the near-wall Mach-invariance of the τ^+ magnitude dictated by the momentum balance and (2) the Mach-invariance of the relative contributions from the generalized viscous and turbulent stresses to τ^+ .

The validity of the first property was demonstrated by Figure 4.5d. Therefore, both viscous stress and turbulent stress in Eq. 4.7 are replaced with τ_{VG}^+ and τ_T^+, respectively as shown in Eq. 4.11. Also, note that the mean shear form of viscous stress, S_V^+, is the same as the viscous stress such that $S_V^+ = \tau_{VG}^+$ and we make use of this simplification in a similar manner to the GFM transformation. The second scaling property of τ^+ is enforced by replacing S_{eq}^+ by S_P^+, the details of which will be discussed subsequently. The resulting equation is shown in Eq. 4.11 where the generalized mean shear, S_G^+, can be integrated with respect to the semilocal wall unit, z^*, from the wall to the freestream to obtain the transformed velocity, $U_G^+ = \int S_G^+ dz^*$.

$$\tau^+ = S_G^+ \left(\frac{\tau_{VG}^+}{S_V^+} + \frac{\tau_T^+}{S_P^+} \right) = S_G^+ \left(1 + \frac{\tau_T^+}{S_P^+} \right) \tag{4.11}$$

Before solving for S_G^+, an expression must be found for for S_P^+ which includes the Mach-invariance of the relative contributions from the generalized viscous and turbulent stresses. We begin by defining R_V and R_T to be the ratio of the viscous and turbulent stresses to the total stress respectively.

$$\begin{aligned} R_V &= \tau_{VG}^+/\tau^+ \\ R_T &= \tau_T^+/\tau^+ \end{aligned} \tag{4.12}$$

The Mach-invariance in the relative contributions of τ_{VG}^+ and τ_T^+ to τ^+ is first ensured by multiplying R_V and R_T by the viscous and turbulent stress terms,

$$\begin{aligned} \tau_{V,P}^+ &= R_V \tau_{VG}^+ \\ \tau_{T,P}^+ &= R_T \tau_T^+ \end{aligned} \tag{4.13}$$

where $\tau_{V,P}^+$ and $\tau_{T,P}^+$ provide an accurate proportional representation of each stress to the total stress at any wall-normal coordinate location. This mathematical treatment decouples the viscous friction, τ_{VG}^+, and turbulent mixing, τ_T^+, effects. Also, note in Fig. 4.9 that τ_P^+, defined as $\tau_P^+ = \tau_{V,P}^+ + \tau_{T,P}^+$, is seen to remain close to Mach-invariant in the near-wall region, as designed. The proportional total stress, τ_P^+ is seen to vary with Mach number in the outer layer region, as its value is reduced after its second peak. Also plotted here is the generalized form of the total stress, τ^+, for comparison.

Provided with an accurate proportional representation of each stress from Eq. 4.13, we can now define a proportional mean shear, S_P^+. We start by assuming that law of the wall for compressible turbulent boundary layer exists, ie, $dU_G^+/dz^* = \tau_{VG}^+$ in the viscous layer and

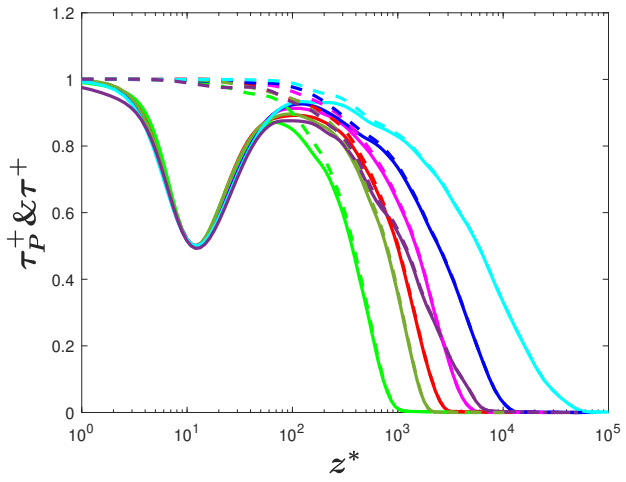

FIGURE 4.9. Solid line indicates proportionally accurate generalized total stress,τ_P^+, and dashed line indicates generalized total stress, τ^+ plotted for comparison. References for lines colors as well as references for the database are included in table 3.1.

$dU_G^+/dz^* = \sqrt{\tau_T^+}/kz^*$ in the turbulent layer. It might be assumed that the sum of the viscous and log-layer shear forms would describe the mean shear at a given wall-normal location. However, to ingrain the stress-proportionality property into the mean shear form, the viscous and turbulent stresses are replaced by $\tau_{V,P}^+$ and $\tau_{T,P}^+$, resulting in equation 4.14.

$$S_P^+ = R_V \boldsymbol{\tau}_{VG}^+ + \frac{\sqrt{R_T(\boldsymbol{\tau}_T^+)}}{\kappa z^*}, \tag{4.14}$$

Note that in the respective layer where each stress dominates, the value of the each stress term approaches 1, thus restoring a similar incompressible law of the wall form, $d\overline{u}^+/dz^+ = 1$ or $\overline{\mu_w} d\overline{u}/dz = \tau_w$ in the viscous layer and $d\overline{u}^+/dz^+ = 1/kz^+$ or $d\overline{u}/dz = \sqrt{\tau_w/\overline{\rho}_w}/kz$ in the turbulent layer.

While the mathematical treatment of the second term in Eq. 4.14 is the same as that of the mixing length hypothesis in that the turbulent stress is also square-rooted and divided by the mixing length, κz^*, the present study does not endorse the mixing length hypothesis. Rather,

this mathematical treatment was derived based on the assumption that law of the wall exists for compressible turbulent boundary layer. For the velocity transformation and for all cases in this study, we use the value of 0.381 for κ from LM5200 in table 3.3, as reported in Lee & Moser [52].

Finally, with S_P^+ derived, which provides the information regarding the proportional contribution of the stresses to the total stress, equation 4.11 can now be rearranged to solve for the mean shear, S_G^+, enforcing the correct magnitude of the total stress such that

$$S_G^+ = \frac{\tau^+}{1 + \tau_T^+ / S_P^+}. \tag{4.15}$$

Thus, the mean shear, S_G^+, in Eq.4.15 provides a newly proposed transformation that preserves the two scaling properties of τ^+ as described in the beginning of the section. Moreover, by the definition of each constituting term and by construction, this transformation includes the effects of mean density and viscosity variation, density and viscosity fluctuations, and viscous and turbulent stress balances.

4.5 Discussion of Results

The transformed mean velocity profiles for CTBL according to Eq. 4.15 are shown in Fig. 4.10a. Also included here is ITBL data that follows the classical law of the wall. The proposed transformation is seen to collapse all of the CBTL velocity profiles (supersonic and hypersonic, adiabatic and non-adiabatic) to the classical incompressible result. In addition to the qualitative examination of the mean velocity profile, both the log-law intercept and slope for all CTBL and ITBL data are extracted in a similar manner to the earlier analysis of the GFM transformation. The characteristic location of the log layer was found using the first

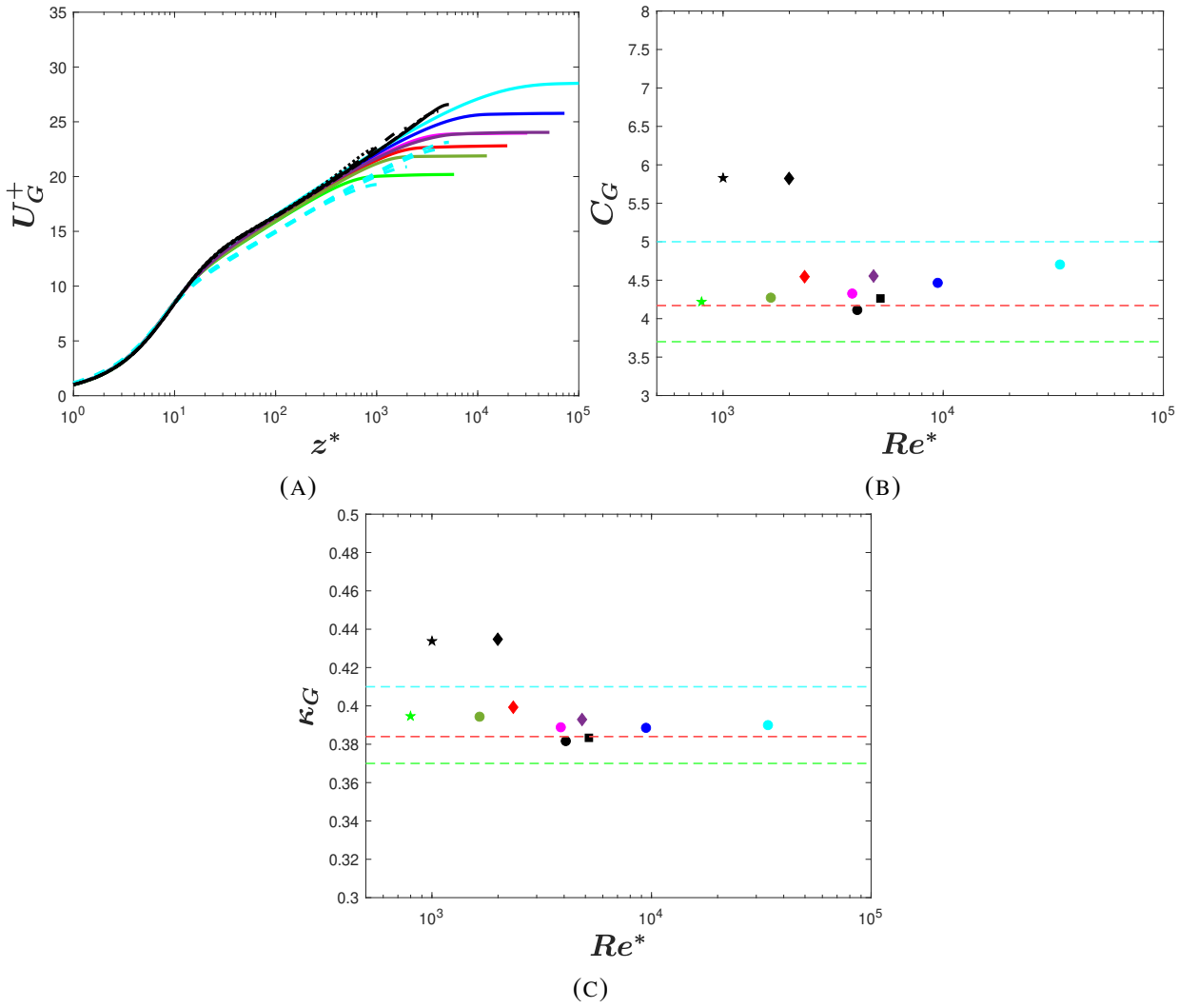

FIGURE 4.10. (A) The presently-proposed velocity transformation versus semi-local wall normal coordinate, z^*. (B) Intercept and (C) von Kármán constant, κ, of the log layer plotted against semi-local Reynolds number. The ITBL flow data listed in table 3.3 are transformed using a conventional law of the wall and are plotted for comparison in (A),(B) and (C). References for line colors and styles and symbols as well as references for the database are included in table 3.1 and 3.3 unless noted otherwise hereafter. Dashed cyan lines in (A) denote the velocity profiles of the ITBL flow data transformed by the proposed MVT. Horizontal lines in (B) and (C) denote variability in the intercept and κ, respectively, reported in Nagib and Chauhan [95], (dashed cyan line, superpipe), (dashed red line, boundary layer) and (dashed green line, channel).

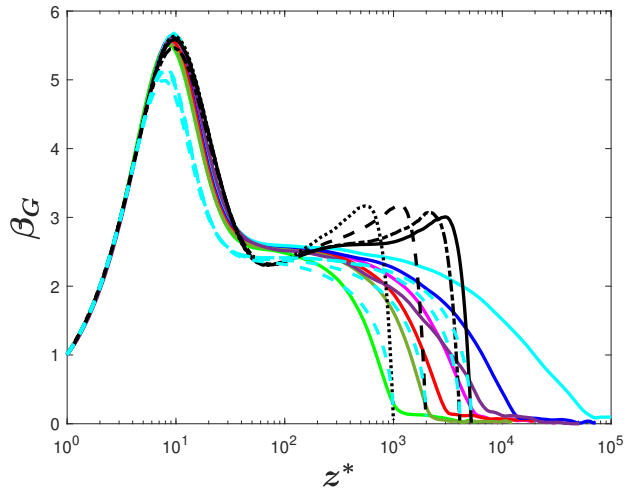

FIGURE 4.11. Pre-multiplied mean shear, β_G,based on the present mean velocity transformation versus semi-local wall normal coordinate, z^*. The pre-multiplied mean shear is calculated for ITBL cases (see table 3.3) using the conventional law of the wall for comparison. References for line colors and styles as well as references for the database are included in table 3.1 and 3.3 unless noted otherwise hereafter. Dashed cyan lines indicate the pre-multiplied mean shear of the ITBL cases transformed by the proposed MVT.

order derivative of the pre-multiplied mean shear profile ($\beta_G = z^* dU_G^+/dz^*$, see Fig. 4.11). Note that slope and the intercept of the ITBL data in Fig. 4.10b and Fig. 4.10c are calculated from the classical law of the wall profiles. With an exception of low Re_τ incompressible cases, which exhibit an expected Reynolds number dependency, the slope and the intercept for CTBL cases in Fig. 4.10b and Fig. 4.10c show a very small variability when compared to highest Reynolds number ITBL cases (LM5200 [52] and BOP4200 [85]). The slope and intercept of the CTBL datasets all lie within the bounds of high Reynolds number values seen for incompressible flow [95]. The proposed transformation accounts for the relative contributions of viscous and turbulent stresses directly, thus it also accounts for one of the main sources of low-Reynolds number dependence on the classical law of the wall.

To quantitatively compare the scatter in the log law intercept and slope for the proposed and GFM transformations, we use the coefficient of variation (CoV), which is defined as the standard

deviation divided by the mean of the data of interest. Higher CoV values indicate larger scatter. The intercept and κ value for LM5200 [52] and BOP 4100 [85] are also considered to measure the scatter with a reference to ITBL cases. Incompressible cases with lower Reynolds numbers, namely LM1000 [52] and LM2000 [52], are excluded as they deviate from the other cases, likely due to their low Reynolds number and insufficient separation of scales. The log law intercept CoV values for the proposed transformation in Fig. 4.10b and for the GFM transformation in Fig. 4.6b are calculated to be 0.0381 and 0.0549, respectively, representing an approximately 50% reduction in scatter. The κ-based CoV values for the proposed and GFM transformations are calculated to be 0.0117 and 0.0559, respectively. It should be noted that, in addition to the reduction in scatter observed for the proposed transformation, the intercept and κ values overlap the incompressible range considerably better.

The pre-multiplied mean shear is computed from the new MVT, β_G, and plotted in Fig. 4.11. As noted earlier, the slope and intercept were calculated where $d\beta_G/dz^*$ is minimum in the log region. This is used as a method to find a region that best approximates a plateau in β that is not dependent on assumed bounds of such a region. Lee & Moser [52] report that the plateau spans from z^+ of 350 to $z/\delta = 0.16$, and the average value of $\partial\beta/\partial z^+$ is 6.46e-5 for the LM5200 case. To compare the plateau region across CTBL cases, averages of $\partial\beta_G/\partial z^*$ from $z^* = 60$ $z/\delta = 0.15$ are calculated. With an exception of M5T1, which does not exhibit a plateau region, potentially due to low Reynolds number, the average of $\partial\beta_G/\partial z^*$ for all CTBL cases ranges from 1.16e-3 to 5.87e-4. Thus the average values of $\partial\beta_G/\partial z^*$ are comparable to the value calculated from the plateau observed in LM5200.

The proposed MVT can also be applied to transform the ITBL cases by setting thermodynamic fluctuation quantities to zero and setting the mean thermodynamic properties to the wall value.

The proposed MVT results in mean velocity profiles that collapse the high Reynolds number ITBL cases (LM5200 and BOP4100) with a logarithmic layer starting around z^* of 60 as shown in Fig. 4.10a. This logarithmic layer can also be confirmed by the existence of the plateau region in β_G for LM5200 and BOP4100, as shown in Fig. 4.11 where the average values of $\partial\beta_G/\partial z^+$ from $z^+ = 60$ to $z/\delta = 0.15$ are 2.46e-4 and 2.22e-4, respectively. Despite this success, differences are observed between the incompressible classical log law and the ITBL cases transformed according to the proposed MVT. While the slope of the semi-log region of the MVT-transformed ITBL profiles is very similar to the classical result, differences can be observed in the log layer intercept values (see Fig. 4.10a). The reasons for the differences between the proposed MVT and the classical log-law for incompressible cases is not immediately apparent, however we partially attribute it to observed differences in the value of τ^+_{VG} in the viscous sublayer for CBTL and IBTL cases, as shown in Fig. 4.5b. Provided that an even more successful scaling of the CTBL and ITBL viscous stress is possible in the viscous sublayer, the proposed MVT might be expected to produce a scaled mean velocity profile for both CTBL and ITBL with the same intercept.

4.6 Summary

In this study, a generalized total stress-based velocity transformation that takes density and viscosity fluctuations into account has been derived by identifying important characteristics of wall-bounded flows at high Mach and Reynolds numbers. It is demonstrated that the influence of density and viscosity fluctuations are important and must be considered when scaling the

turbulent shear stresses of all CTBL cases considered in this study. When employing Reynolds averaging, fluctuating viscosity or density-related terms exceeded 5% of the wall shear stress for all cases. In some cases these terms exceeded 20% of the wall shear stress. Employing the full Favre averaged momentum equation effectively accounts for the influence of density fluctuations on the near wall stress balance but viscosity fluctuation terms were seen to be as large as 12% of the wall shear stress in the buffer region.

When the influences of the density and viscosity fluctuations on the viscous and turbulent stresses are fully accounted for by including all relevant terms in the near-wall momentum equation, two scaling properties have been identified, namely, (1) the Mach-invariance of the near-wall momentum balance for the generalized total stress and (2) the Mach-invariance of the contributions from the generalized viscous and turbulent stresses to the total stress. A new generalized mean velocity transformation, which considers the effects of mean density gradient, both viscous and turbulent stresses, and the effect of density and viscosity fluctuations, has been derived by accounting for these two scaling properties.

The proposed velocity transformation is seen to provide an accurate representation of the logarithmic layer. For a wide range of Mach numbers, Reynolds numbers and heat transfer, the scatter in the intercept and slope of the new transformation are within the bounds found for incompressible flows. The new transformation is successful because it accounts for the density and viscosity fluctuation effects in both the viscous and turbulent stresses as well as the relative contributions of the viscous and turbulent stresses to the near-wall momentum balance. For this reason, no Reynolds number dependence was observed in the slope and intercept of transformed velocity profiles under the new transformation. It was successful in collapsing velocity profiles for all compressible cases described in this study.

Despite this success, it should be noted that the proposed transformation requires knowledge of the effects of fluctuations in the thermodynamic variables on the viscous and turbulent stresses, which will limit its use in some situations in the near-term. Additionally, the intercept of incompressible flow data when transformed according to the proposed MVT, was found to be shifted relative to the conventional log-law. This is attributed to a small remaining scatter between the incompressible and compressible viscous stress profiles, the source of which is still uncertain. This leads to a shift in the premultiplied shear stress profiles. Further study is needed to explore this effect as both viscous and density fluctuations have been accounted for in the current formulation.

While the transformation of Griffin et al. [4] has shown promising and improved collapse of the mean velocity profiles, the use of the quasi-equilibrium model [35] to describe the turbulence in the log layer is not strictly accurate, with moderate scatter in the ratio of production and dissipation in the log-layer.Examination of the underlying assumptions in the derivation of the GFM transformation suggest its remaining challenges may be due to insufficient Mach invariance of the turbulent stresses and the ratio of production and dissipation as traditionally formulated.

The success of the proposed MVT can be attributed to considering the influence of density and viscosity fluctuations and the mean property gradients in both the viscous and turbulent stresses. Two scaling properties, namely, the proportionality and the Mach-invariance of the generalized total stress, are identified and integrated into the newly proposed MVT.

Chapter 5: Reynolds Number Trends in Large Turbulent Structures

5.1 Background

Over the last few decades, many studies have been conducted to examine the behaviors of turbulent intensities and near-wall turbulent structures in ITBL flows since Townsend's 'attached eddy hypothesis' was proposed [19]. In his model, Townsend predicted the size of the attached eddies parallel to the wall to scale with the distance from the wall and the larger eddies above to impart their presence to the small eddies closer to the wall. That is, he predicted that the near-wall velocity fluctuation is the result of superposition of induced fluctuations at every wavenumber(or length) above. In line with the Townsend's hypothesis, friction Reynolds number, Re_τ, dependent growth of near-wall turbulent intensities has been observed [50–52, 96–98] and the growth has been attributed to the influence of the large eddies in the log layer growing with Re_τ [72]. Subsequently, researchers have examined the behavior of these large scale turbulent eddies as well as the amplitude modulation of near-wall small eddies by the bigger eddies [72, 99] in an effort to better understand and predict the near-wall turbulence.

A few note-worthy features of large turbulent structures such as large scale motion or very large scale motion have been observed and characterized in studies involving ITBL. The structural sizes of LSM have been examined using the pre-multiplied spectra analysis of velocity fluctuations in several studies [71, 100, 101]. They reported the streamwise and spanwise lengths of

LSM extending up to 2-3δ and 1-1.5δ, respectively. More importantly, VLSM has also been identified and characterized in ITBL. Hutchins and Marusic [73] used the spanwise hot-wire rake and reported the length of VLSM to extend up to 20 δ. In addition, they demonstrated that VLSM meanders substantially in the spanwise direction [73]. Turbulent kinetic energy contained in VLSM has also been measured with approximately 40% $\sim$ 50% of turbulent kinetic energy being generated from long wavelength with longer than 3 times the outer length scale in both boundary layers and pipes [71, 100]. Hutchins and Marusic [72] experimentally analyzed these large-scale structures using pre-multiplied streamwise energy spectra with Re_τ 2800 to 17000 and reported that the characteristic locations of VLSM both in wall normal direction and in wavenumber space scale with Re_τ. In more recent studies at Princeton, several experiments [48, 75, 76] extended Re_τ ranging from 3000 to 70000 and demonstrated a similar VLSM trend exists even at higher Reynolds number for both pipes and boundary layers.

Understanding of the Reynolds number dependent behavior of large turbulent structures observed in ITBL studies provides a groundwork on building a robust and accurate near-wall turbulence prediction model by providing a necessary variables such as cut-off wavelength between the small turbulent scales and large turbulent scales. Thus, characterizing large turbulent structures in compressible turbulent boundary layer is a necessary component in developing a near-wall turbulence prediction model similar to the models developed in ITBL studies [102, 103]

Over the years, a number of studies have revealed large-scale structures in CTBL [2, 20, 21, 23, 24, 78, 104] similar to the ones observed in aforementioned incompressible studies. For example, Ringuette et al. [20] identified large coherent structures with similar inclination angles as ITBL studies [62, 105] in Mach 3 CTBL based on mass-flux fluctuation, $(\rho u)'$, correlation despite an order of difference in Reynolds number. Several studies on CTBL [2, 21, 23], despite

basing on different velocity fluctuation signals, also reported a presence of VLSM in pre-multiplied spectra with their wavelengths around $2 \sim 10\delta$. An important theory that connects the compressible and incompressible turbulent boundary layer is the Morkovin's hypothesis [10] which postulates that the essential turbulence dynamics of the compressible flow follow the incompressible flow pattern. Based on this theory, the existence of a similar large turbulent structure behavior in CTBL as in ITBL is perhaps not surprising. However, the Reynolds number dependent trend of large turbulent structures observed in several ITBL studies [75, 76, 99] is yet to be verified in CTBL flows.

To properly address this gap in our understanding of the large-scale structures in CTBL, a few recent papers [1, 2, 21, 23, 24] that examine CTBL with a wide range of Re_τ and Re^* have been published which can provide a necessary high Reynolds number data set to examine the Reynolds number effects on large turbulent structures. In particular, as noted in ITBL studies, the Re^* dependent near-wall turbulent intensity peak growth, which is considered a result of large turbulent structure growth scaling with Reynolds numbers, is observed in several studies [2, 23, 45]. In particular, using a CTBL dataset with varying Re^* and a relatively constant $Re_\tau \simeq 500$, Williams et al. [106] confirmed that the logarithmic growth of the near-wall turbulent intensities peak similar to the Re_τ dependent turbulent intensity behavior in ITBL is indeed a Re^* dependent behavior. This result suggests that Re^* is an important parameter in the determination of the behavior of large turbulent structures in CTBL. However, it is still unclear how Re^* determines the behavior of large turbulent structures as the conventional consensus suggests that Re_τ determines the behavior of large turbulent structures in both ITBL and CTBL.

The lack of unilateral agreement on a single form of Reynolds number to characterize large turbulent motions in CTBL in a similar manner as ITBL is perhaps expected since both Re_τ

and Re^* represent important physics to consider in characterizing CTBL. The intrinsic natures of CTBL are that (1) it is comprised of wide range of length scales and (2) it is heavily influenced by thermodynamic property effect. That is, Re_τ, which measures the ratio of the smallest physical scale and the largest physical scale in CTBL, describes the former property in a sense and Re^*, which measures the influence of thermodynamic property gradient on the range of length scales in CTBL, describes the latter property in a sense. Given this observation, different roles of Re_τ and Re^* in characterizing large turbulent structures in CTBL are perhaps expected and need to be verified.

Therefore, the main objective of the present chapter is to examine the Re_τ and Re^* dependent behavior of large turbulent structures such as LSM or VLSM in order to characterize the role of both Reynolds numbers in determining the behavior of large turbulent structures particularly in the inner layer of CTBL. In the process, implications of the Reynolds number trend in large turbulent structure behaviors as well as cut-off wavelength between small scale and large scale are discussed and analyzed. To achieve this goal, we will make use of CTBL data from Lee et al. [1] and Cogo et al. [2] listed in table 3.4, both of which provide CTBL database with Re_τ ranging from 700 to 2300 and Re^* ranging from 3000 to 55000. A similar pre-multiplied spectra analysis as done in several ITBL studies [49, 75, 76, 99], is performed to determine the characteristic behavior of LSM and VLSM in wavelength space at a given wall normal position. The behaviors of LSM and VLSM identified in present chapter are compared to the Reynolds number dependent trend of VLSM reported in [99, 107] to verify similarities of large turbulent structures between ITBL and CTBL.

5.2 Data Synthesis: Pre-multiplied Energy Spectra

Before proceeding any further in this section, it is important to note that the range of Re_τ and Re^* in Table 3.4 differs from the range in Table 3.1, even though both are based on the same CTBL dataset. This disparity arises because the Reynolds numbers used in this chapter and in Table 3.4 are defined based on momentum-based boundary layer thickness, rather than velocity-based boundary layer thickness. A recent study by Williams et al. [106] has demonstrated that using density-scaled streamwise turbulent intensity results in better outer layer scaling when employing a momentum-based boundary layer thickness (See Fig. 1 in their paper). Therefore, while no additional subscript is employed to indicate this difference for the sake of notation conciseness, references to any Reynolds number or δ in this chapter pertain to momentum boundary layer thickness-based parameters.

Furthermore, in the analysis of large scale motions, this chapter employs pre-multiplied energy spectra based on the $\sqrt{\rho}u''$ velocity signal, which effectively becomes $\rho u''u''$ following the operation of power spectral density. This choice is in line with the approach outlined in section 5.1. Various studies adopt different forms of density-corrected velocity fluctuation signals, such as $(\rho u)'$ [20], $\rho u''u''$ [2, 24], and $\overline{\rho}u''u''$ [21], as representative signals containing such structural information. However, a primary objective of this paper is to investigate parameters relevant to a turbulent kinetic energy prediction model. While the $(\rho u)'$ velocity signal is valuable, it is not directly tied to turbulent kinetic energy. Moreover, Patel et al. [90] proposed that the mean density-scaled turbulent intensity, $\overline{\rho}u''u''$, is approximately equivalent to $\rho u''u''$ when density fluctuations are not strong, based on Morkovin's hypothesis. Nonetheless, the examination of CTBL DNS cases with varying Re^* by Lee et al. [1] revealed that the influence of density fluctuation

terms in CTBL analysis is non-negligible. The use of instantaneous density was also found to accentuate turbulent streaks [23, 90], indicative of large turbulent structures. Consequently, the $\rho u'' u''$ velocity signal takes precedence over $\overline{\rho} u'' u''$ or $(\rho u)'$ in generating pre-multiplied energy spectra within this chapter.

To reconstruct the pre-multiplied energy spectra, Welch's method is employed to calculate power-spectral density (PSD) based on the temporal $\sqrt{\rho} u''$ velocity signal sampled at the outlet yz plane, as provided in Table 3.2. The length of the temporal signal, $t\overline{u}_e/\delta$, and the sampling frequency, $\Delta t\overline{u}_e/\delta$, are documented in Table 3.4. For the PSD calculation, a Hamming window is applied to four segments of the input temporal signal window, with 50% overlap between each window. The resulting PSD is then averaged over the homogeneous spanwise direction for improved convergence. This process is repeated for every wall-normal location. Based on Taylor's frozen turbulence hypothesis, the frequency spectrum in Hz is converted into a wavenumber spectrum using the relationship $k_x = 2\pi f/U_c$, where k_x is the streamwise wavenumber, U_c is the local mean velocity at each wall-normal position, and f is the frequency spectrum. Note that the streamwise wavenumber can be further converted into a wavelength using the relationship $k_x = 2\pi/\lambda_x$, where λ_x represents the streamwise wavelength. This use of the local mean velocity to convect turbulence is akin to the approach outlined by Mathis et al. [99]. The pre-multiplied energy spectra is then reconstructed by multiplying the streamwise wavenumber, k_x, with the power spectral density, $\phi_{\rho u'' u''}$. In the final step, spectral averaging with a width of $0.1 \log(\lambda^*)$ is executed to smooth out the pre-multiplied energy spectra, resulting in the final version used to identify characteristic locations for LSM and VLSM. Sample pre-multiplied spectra from cases M6H and M12T5, which represent the highest Re_τ and Re^* values respectively, are included in Fig. 5.1.

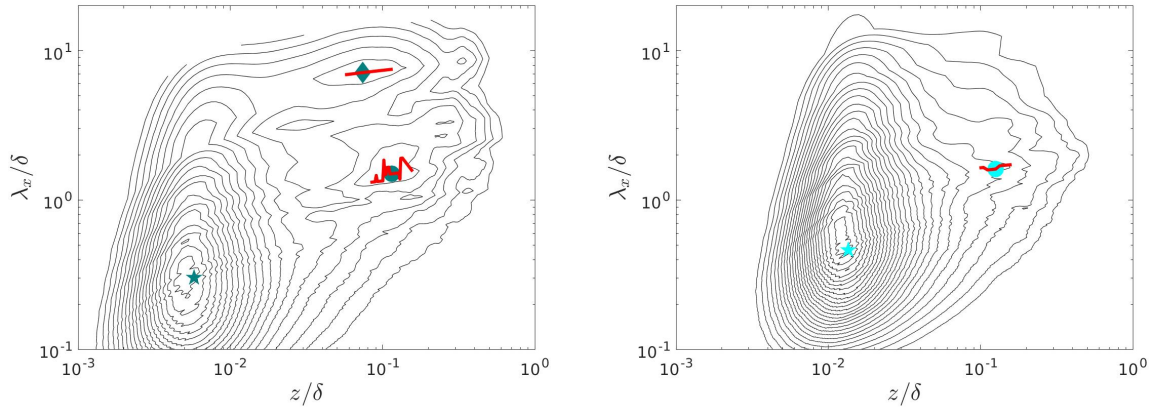

FIGURE 5.1. Contour maps of one-dimensional streamwise pre-multiplied energy spectra of (A) M6H (B) M12T5. x-axis shows wall normal positions normalized by δ. y-axis shows streamwise wavelength normalized by δ. Pentagon, circle and diamond symbols denote ISP, LSP and VLSP, respectively. Solid red line in (B) denote plateau region. Reference for marker color is included in table 3.1

In this study, similar to high Reynolds number ITBL investigations [73,99,107], characteristic locations of LSM and VLSM denoted as LSP and VLSP are identified. To pinpoint these peaks and avoid ambiguity, a peak-finding mechanism is employed as described below. Additionally, an investigation into the inner spectral peak is conducted to further validate the behavior of near-wall turbulence. It is worth noting that the pre-multiplied spectra used in the peak-finding algorithm is constructed from the $\rho u'' u''$ velocity signal, normalized by τ_w in line with convention. To detect the peaks, the pre-multiplied spectra are plotted with respect to the normalized streamwise wavelength (λ_x) and the normalized wall-normal distance (z), both normalized by δ. A map of the related partial derivatives is also utilized in the process. This choice of normalization aligns with the prevailing consensus in the literature that LSM and VLSM are outer scale phenomena. Fig. 5.1 presents samples of pre-multiplied energy spectra for M6H and M12T5, with both x-axis and y-axis normalized by δ. Cases that are not shown in this section are provided in Appendix B.

In the peak search algorithm, a pre-multiplied energy spectra contour plot is divided into

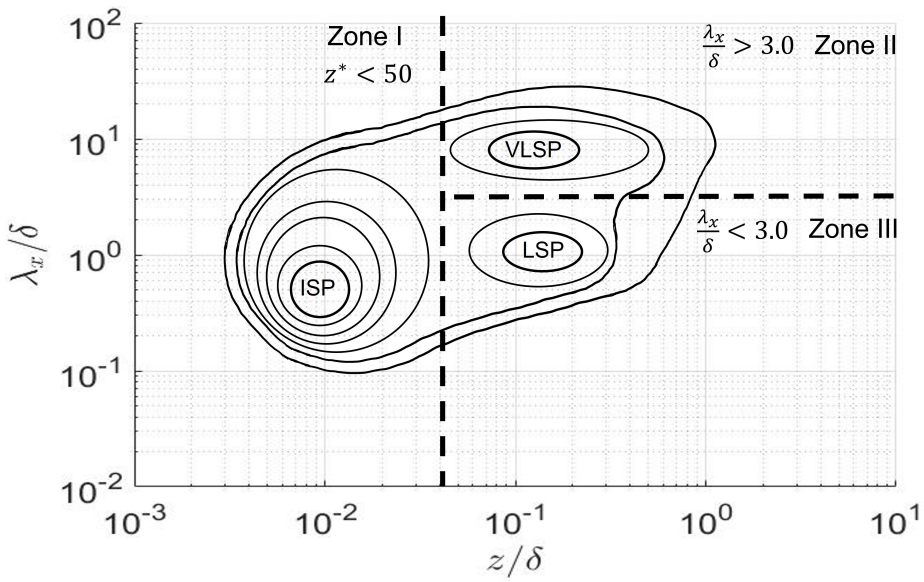

FIGURE 5.2. Generic pre-multiplied spectra used by the peak search algorithm

3 regions where a peak in each region is searched as shown in a generic pre-multiplied spectra in Fig.5.2. The limits of each region are determined as follows. In region I where it searches for the inner spectral peak (ISP), it is determined to be region below z^* of 50 regardless of the wavelength. In region II where it searches for the peak location of VLSM (VLSP), wall normal position bound is set to be the wall normal location between $z^* = 50$ and $z/\delta = 0.4$ (low Re_τ) or 0.2 (high Re_τ). The upper limit is determined by visually inspecting the pre-multiplied spectra so that the possible peak is located well within the prescribed bounds. It is confirmed that the choice of the upper bounds in wall normal direction has no influence in the determination of VLSP location. The spectral bound for VLSP is set to be above λ_x/δ of 3. In region III where it searches for the characteristic location (peak) of LSM (LSP), wall normal position limit is set to be between $z^* = 50$ and $z/\delta = 0.4$ or 0.2 depending on Re_τ similar to region II. The spectral bound for LSP is set to be below λ_x/δ of 3.

With regard to the the search method, there exists an absolute maximum in region I and

therefore, a simple search for a maximum PSD location is sufficient. However, in region II and III, a distinct peak may not exist and LSP & VLSP may exist in a form of a plateau instead. Therefore, a location of the least slope or 'plateau' is searched in region II and III by calculating partial derivatives in the direction of z and λ. The partial derivatives in each direction are normalized by its respective maximum. Then, L2 norm of both partial derivatives are calculated to represent the 'total derivative' at the respective location. If the location corresponds to the point with lowest slope (lowest 'total derivative') and maximum PSD within the respective zone of interest, the location is identified as LSP & VLSP. If no distinctive peak exists, then the location with the lowest slope is first marked and is considered as a portion of a plateau which is further processed as described in the following. A plateau region is defined as the location where the difference in the magnitude of both the slope and PSD value is less than 5% from the marked location. All plateau are marked with red line as shown in Fig. 5.1. Finally, when a plateau is observed, a mid point of a plateau in wall normal direction is selected as LSP & VLSP instead of the location with the least slope. Note that visual inspection of pre-multiplied spectra indicates VLSP exists only in M2H and M6H with high Re_τ and VLSP is not searched in cases with low Re_τ.

5.3 Preliminary Observation

To initially assess the influence of Re^* on the behavior of large turbulent structures, pre-multiplied energy spectra from M3T5 and M12T5 – cases representative of the Re^* range featured in this study – are depicted in Fig. 5.3. Notably, while Re_τ remains constant, Re^* is allowed to vary, enabling an isolated exploration of the independent effect of changing Re^* on large turbulent structures. A comparison of the pre-multiplied spectra from M3T5 and M12T5, as displayed in

Fig. 5.3, underscores a crucial finding: the sizes of the 'outer region', broadly defined as the zone within the log layer and characterized by higher wavelengths (effectively the upper right quadrant in PSD plots), increases with Re^*. This observation gains further significance when aligned with the LSM trend elucidated by Vallikivi et al. [107], hinting at the discernible connection between the increased turbulent energy signature in the 'outer region' and the signatures of Large Scale Motions. It suggests that the semi-local length-scaled variables and Re^* can effectively encapsulate the LSM behavior within the context of CTBL. This insight holds a distinct intrigue, considering that the LSM signature reported by Vallikivi et al. [107] primarily depends on Re_τ and the LSM patterns emerging at z^* and λ^* within the 'outer region' of, say, the M12T5 case, are observed at significantly higher Re_τ in ITBL studies. By revisiting the definition of Re^*, which accounts for the influence of density and viscosity gradients across the boundary layer on Re_τ, we can put forth a postulation. In CTBL, even when Re_τ is low, large turbulent structures behave locally under the influence of thermodynamic property and follow the turbulent behavior described by Re^* at least up to the log layer.

Furthermore, beyond the suggested Re^*-dependent LSM behavior, there is an inherent expectation that varying Re_τ exerts an independent influence on large turbulent structures within CTBL. This stems from the understanding that Re_τ quantifies the physical scale separation between the smallest and largest scales present in turbulent boundary layers. In light of this perspective, attention turns to two pairs of cases cataloged in Table 3.4, each characterized by similar Re^* values yet differing Re_τ. These case pairings offer a unique dataset, enabling the distinct examination of the impact of varying Re_τ. The first pair, comprising M5T5 and M2H, showcases comparable Re^* values around 5000, while exhibiting contrasting Re_τ values. The second pair, M7T5 and M6H, mirrors a similar scenario, with a matching Re^* but varying

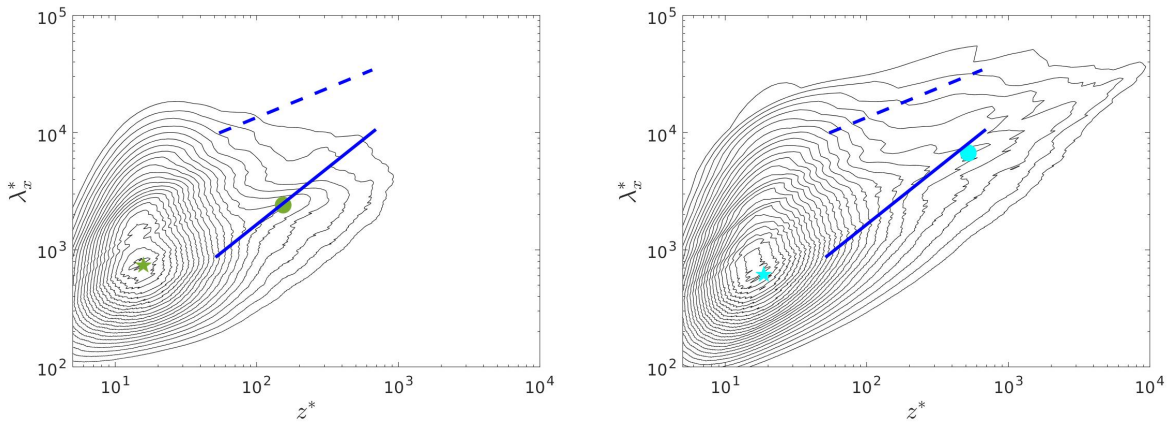

FIGURE 5.3. Contour maps of pre-multiplied spectra of selected cases at approximately constant $Re_\tau \simeq 700$ and varying Re^*. (A) M3T5($Re^* \simeq 2000$) (B) M12T5($Re^* \simeq 54000$) based on $\rho u'' u''/\tau_w$ velocity signal. x-axis shows wall normal position normalized by semi-local scaling. y-axis shows streamwise wavelength normalized by semi-local scaling. Blue solid and dashed lines correspond to LSM trend, $k_x^+ y = 0.4$, and VLSM trend, $k_x \delta = 0.33(\delta/z)^{0.5}$, respectively, reported by Vallikivi et al. [107]. Pentagon and circle markers denote ISP and LSP, respectively. References to the color of markers are included in table 3.4.

Re_τ. It is acknowledged that a notable disparity exists in the magnitudes of Re^* between M7T5 and M6H. However, it is imperative to note that the reported Reynolds number trends in the existing literature [73, 107] often adhere to either a logarithmic or square root relationship with the Reynolds number. As a result, despite the contrasting magnitudes of Re^*, it is reasonable to conclude that the Re^* effect in both M7T5 and M6H is akin in nature. By acknowledging this coherence in the Re^* effect, even across cases with varying magnitudes of Re^*, it is deemed that Re^* effect in M7T5 and M6H is similar.

To explore the influence of Re_τ, the pre-multiplied spectra of $\rho u'' u''$ from the aforementioned case pairs are plotted in Fig.5.4. A comparison of the pre-multiplied energy spectra in Fig.5.4 indicates an enlargement of the 'outer region' in the cases with higher Re_τ. Specifically, while the 'outer region' in the pre-multiplied spectra of high Re_τ cases depicted in Fig.5.4b and Fig. 5.4d

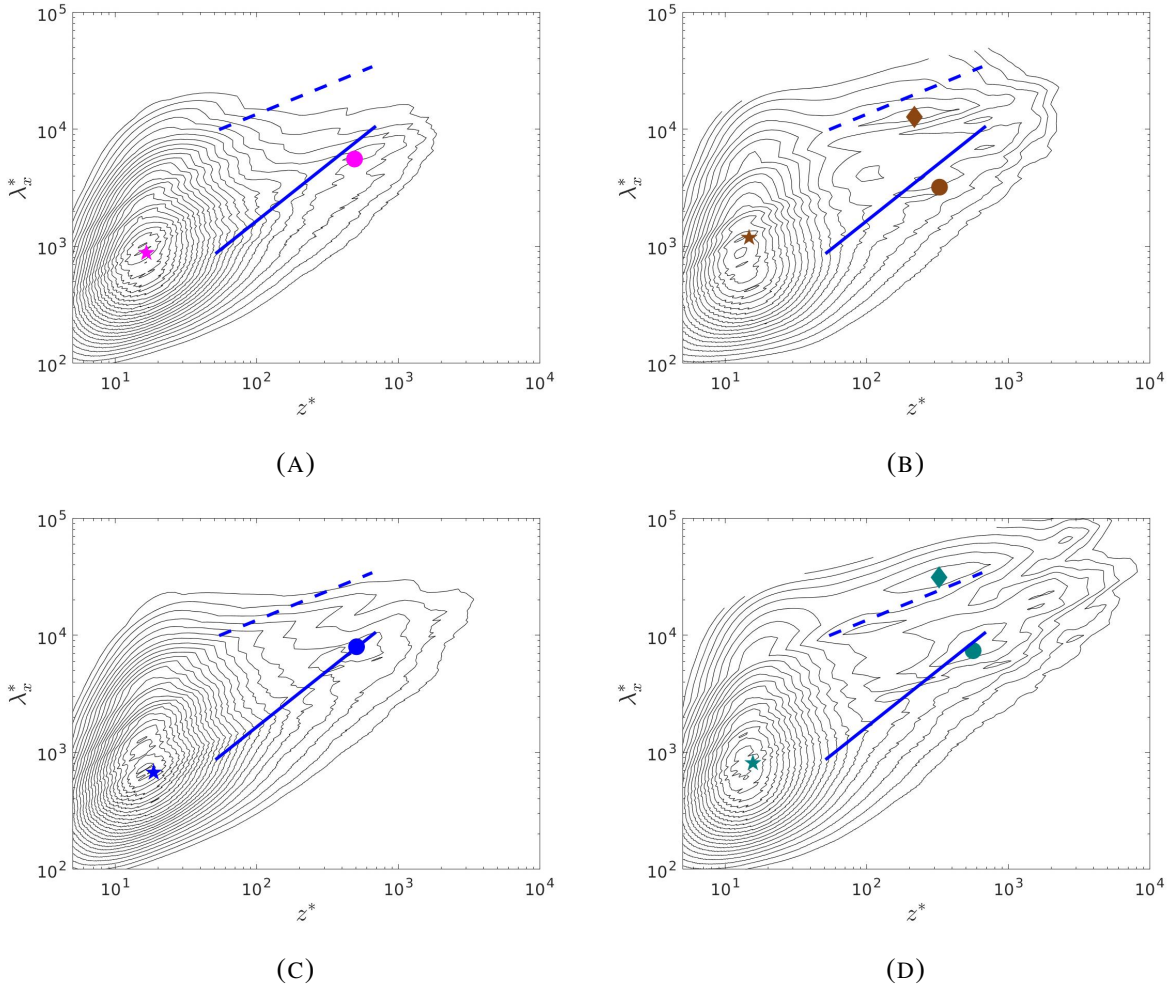

FIGURE 5.4. Contour maps of streamwise pre-multiplied spectra, $k_x PSD$, based on $\rho u'' u''/\tau_w$ velocity signal of selected cases with varying Re_τ and constant Re^*. Cases at $Re^* \simeq 5000$ and varying Re_τ, (A) M5T5 ($Re_\tau \simeq 650$) (B) M2H ($Re_\tau \simeq 2300$); at $Re^* \simeq 20000$ and varying Re_τ, (C) M7T5 ($Re_\tau \simeq 850$) (D) M6H ($Re_\tau \simeq 2300$). x-axis shows wall normal position in viscous length normalization. y-axis shows streamwise wavelength in viscous length normalization. Blue solid and dashed lines correspond to LSM trend, $k_x^+ y = 0.4$, and VLSM trend, $k_x \delta = 0.33(\delta/z)^{0.5}$, respectively, reported by Vallikivi et al. [107]. Pentagon, circle and diamond symbols denote ISP, LSP and VLSP, respectively. Reference for marker color is included in table 3.4.

manifests at relatively similar z^* values as their low Re_τ counterparts, a conspicuously extended region characterized by longer wavelengths emerges in Fig.5.4a and Fig. 5.4c. This elongated wavelength region is notably absent even in the case of M12T5, which boasts the highest Re^*. Significantly, the VLSM trend reported by Vallikivi et al. [107] aligns with this elongated wavelength region within the 'outer region' of high Re_τ cases. This alignment strongly supports the proposition that the lengthened wavelength feature accompanying elevated Re_τ indeed corresponds to the characteristics of VLSM. Notably, the observation of VLSM around $Re_\tau \simeq 2000$ in cases like M2H and M6H closely approaches the proposed threshold of $Re_\tau = 2000$, a value proposed by Hutchins and Marusic [72, 73] as the limit for VLSM observation. Considering that LSM and VLSM are outer scale structures with behaviors closely associated with δ, a reasonable interpretation emerges: the presence and potentially the strength of both LSM and VLSM are primarily governed by Re_τ rather than Re^*, even within CTBL.

Moreover, while the precise roles of Re_τ and Re^* in the growth and behavior of LSM and VLSM are yet to be detailed in the upcoming sections, it it evident that the influence of these two Reynolds numbers on the behavior of large turbulent structures within CTBL is different. This distinction becomes apparent once again when observing the near-wall peak of streamwise turbulent intensities, $\overline{\rho u'' u''}^+$, in Fig.5.5. Following the similar approach in Fig.5.3 and Fig.5.4, Fig.5.5a contrasts cases with a fixed Re_τ while varying Re^*, whereas Fig. 5.5b contrasts cases with a fixed Re^* while varying Re_τ. As documented in various CTBL studies [23, 24], it is apparent from Fig. 5.5a that the amplitude of the near-wall turbulent intensity peak increases as Re^* escalates. Conversely, in Fig. 5.5b, it is evident that the amplitude of the near-wall turbulent intensity peak decreases with increasing Re_τ. It is worth noting that similar decrease in the amplitude of the near-wall turbulent intensity peak is observed as Re_τ is increased when

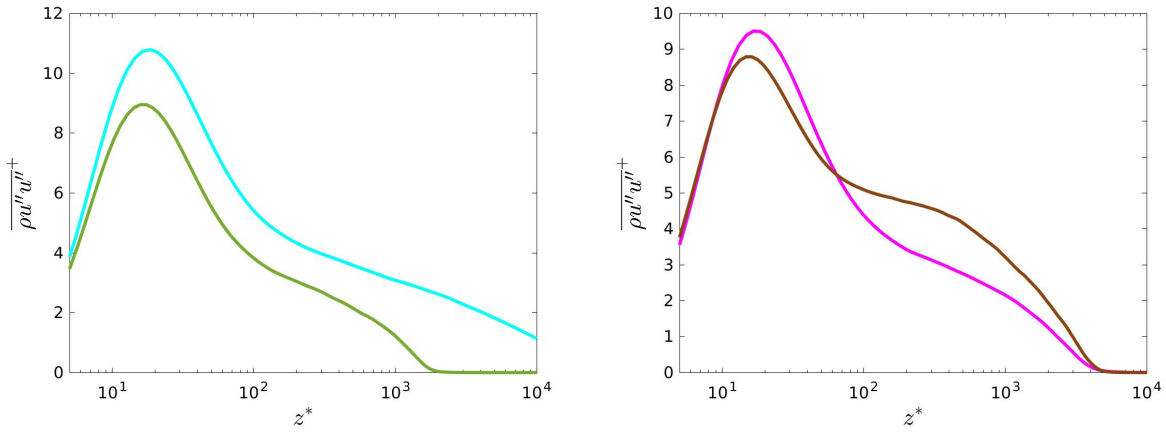

(A) (B)

FIGURE 5.5. Normalized turbulent intensity, $\overline{\rho u'' u''}^+$ versus semi-local wall normal positions, z^* for (A) selected cases (M3T5 & M12T5) at approximately constant $Re_\tau \simeq 700$ and varying Re^* (B) selected cases (M5T5 & M2H) at approximately constant $Re^* \simeq 5000$ and varying Re_τ. Pentagon and circle symbols denote ISP and LSP, respectively. Reference for marker color is included in table 3.4.

comparing M7T5 and M6H cases, which share a similar Re^* but exhibit varying Re_τ. The perplexing reduction of the near-wall turbulent intensity peak with heightened Re_τ challenges our conventional expectation, which associates higher Reynolds numbers with an increase in the near-wall turbulent intensity peak. Notably, the variation in the amplitude of the near-wall turbulent intensity peak is a consequence of the activity of large turbulent structures [99, 108]. While a comprehensive analysis of near-wall turbulent intensity amplitude modulation and its reliance on Re^* and Re_τ lies beyond the present study's scope, the observation in Fig. 5.5 unequivocally underscores that Re^* and Re_τ exert distinct effects on the behavior of large turbulent structures within CTBL.

Before proceeding, the key observations made in this section are summarized. First, the emergence of VLSM with an increase in Re_τ suggests that the presence or intensity of large turbulent structures could potentially be governed by Re_τ. This finding aligns with ITBL results,

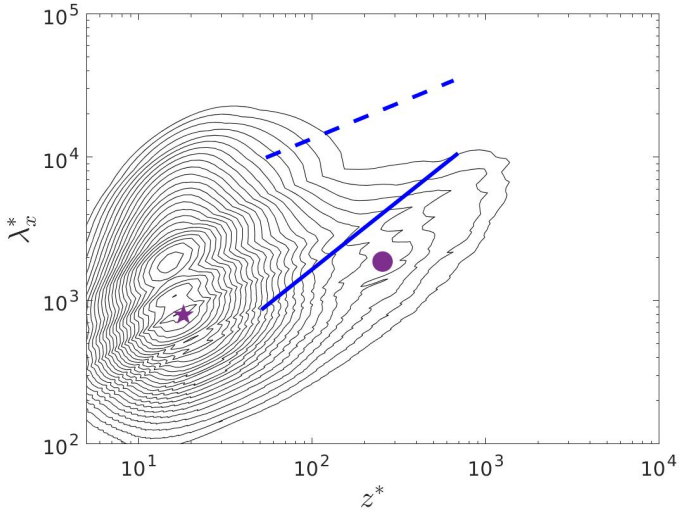

FIGURE 5.6. Pre-multiplied spectra based on $\rho u'' u''/\tau_w$ velocity signal. x-axis shows wall normal location normalized by semi-local scaling. y-axis shows wavelength normalized by semi-local scaling. (A) M10T3. Blue solid and dashed lines correspond to LSM trend, $k_x^+ y = 0.4$, and VLSM trend, $k_x\delta = 0.33(\delta/z)^{0.5}$, respectively, reported in Vallikivi et al. [107]. Pentagon and circle symbols denote ISP and LSP respectively. Reference for marker color is included in table 3.4

where large turbulent structures scale with Re_τ [49, 72, 75, 98, 99, 107, 109]. Secondly, the parameter Re^* exhibits the potential to describe the location and wavelength of large turbulent structures within the log layer of CTBL. However, these initial observations require further analysis to reach definitive conclusions. In the subsequent sections, the identified peak locations of LSM and VLSM, utilizing the algorithm outlined in section 5.2, will be plotted to provide a more detailed exploration of the behavior of large turbulent structures and their dependencies on Re_τ and Re^*.

5.4 Large Turbulent Structures and Reynolds Number Trend

All pre-multiplied spectra, normalized using the semi-local length scale, are featured in Fig.5.3 and Fig.5.4, encompassing all cases except for the cold wall case, M10T3. This latter

case is separately presented in Fig. 5.6. Supplementary pre-multiplied spectra, employing viscous scale and outer scale normalization, are appended in Appendix B. The ISPs across all CTBL cases consistently appear approximately at $\lambda_x^* = 1000$ and $z^* = 15$, matching the values documented in ITBL and CTBL studies [2, 23, 24, 45, 73, 107]. An inspection of pre-multiplied spectra using δ length scale normalization in Fig.5.1 reveals that both LSP and VLSP extend to around $1{\sim}2\delta$ and $\sim 6\delta$ respectively. This is consistent with previous studies that have reported the δ scaled wavelength of LSM [71, 100, 101] and VLSM [21, 73, 107]. Similar trends are upheld for all other cases not included in Fig.5.1. Additionally, it's important to note that the length of VLSM is notably shorter than the reported 20δ, primarily due to the substantial meandering of VLSM in the spanwise direction. This meandering effectively masks the true length of VLSM when solely relying on single-point statistics such as streamwise pre-multiplied spectra [73].

5.4.1 Inner Length Scale

For deeper insights, the wall-normal positions of LSP and VLSP in both viscous (+) and semi-local (*) length scales were calculated using the aforementioned peak-finding mechanism. These positions were computed for the CTBL cases outlined in table 3.4 and plotted against both Re_τ and Re^* in Fig.5.7. In this representation, wall-normal locations in viscous and semi-local length scales are respectively denoted by z^+ and z^*, following conventional nomenclature. An error bar indicates the range of plateau in the wall-normal direction in Fig.5.7. At first glance, the behaviors of z^* and z^+ for LSP and VLSP, when scaled by semi-local and viscous length scales, respectively, appear to display distinct dependencies on Re^* and Re_τ. It is also evident for all CTBL cases that LSP and VLSP occur at approximately similar wall-normal positions.

As demonstrated in Fig. 5.7a and Fig. 5.7b, the Reynolds number trend observed in z^* and z^+ follow similar Re_τ trends reported in ITBL [73,99,107]. In particular, using experimental data with Re_τ ranging from 2800 to 19000, Mathis et al. [99] studied the location where amplitude modulation coefficient between the large scale motion and small scale motion reaches zero and reported that the location aligns with VLSP location which exhibits Reynolds number dependence given by $z^+ = 3.4Re_\tau^{0.5}$. It is seen in Fig. 5.7a that z^* location of LSP and VLSP follows the Re_τ dependent zero amplitude modulation location reported in ITBL study by Mathis et al. [99] up to approximately Re^* of 15000. Note z^* and Re^* is equal z^+ and Re_τ, respectively, in ITBL. However, at higher Re^*, we observe a slight deviation in z^* of LSP & VLSP from the trend by Mathis et al. [99]. Instead, LSP & VLSP start to emerge at a fixed location around 400 z^* similar to the observation made by Vallikvi et al. [107] who reported that the z^+ location of VLSP in ITBL cases above Re_τ of 20000 appeared to be fixed around z^+ of 300.

With regard to the Re_τ trend in CTBL, z^+ locations of LSP in Fig. 5.7b slightly overpredict the ITBL trend given by $z^+ = 3.4Re_\tau^{0.5}$ [99]. However, all of the LSPs emerged as plateau with substantial range denoted by the error bar rather a distinct peak and the plateau occurs within the margin of error for the reported trend. Moreover, z^+ locations of VLSP in M2H and M6H which appear as a distinct peak show minimal difference from the ITBL trend. While it is still inconclusive to determine the Re_τ dependent behavior of VLSP due to a limited range of Re_τ in CTBL database used in present study, evidence suggests that z^+ of LSP and VLSP should exhibit Re_τ trend reported in ITBL study [99].

Streamwise wavenumbers, k_x, associated with LSP & VLSP for CTBL cases are plotted against Re_τ and Re^* in Fig.5.8 where k_x^+ and k_x^* denote streamwise wavenumbers normalized by viscous(+) and semi-local(*) length scale. Note that an error bar is used to denote the range

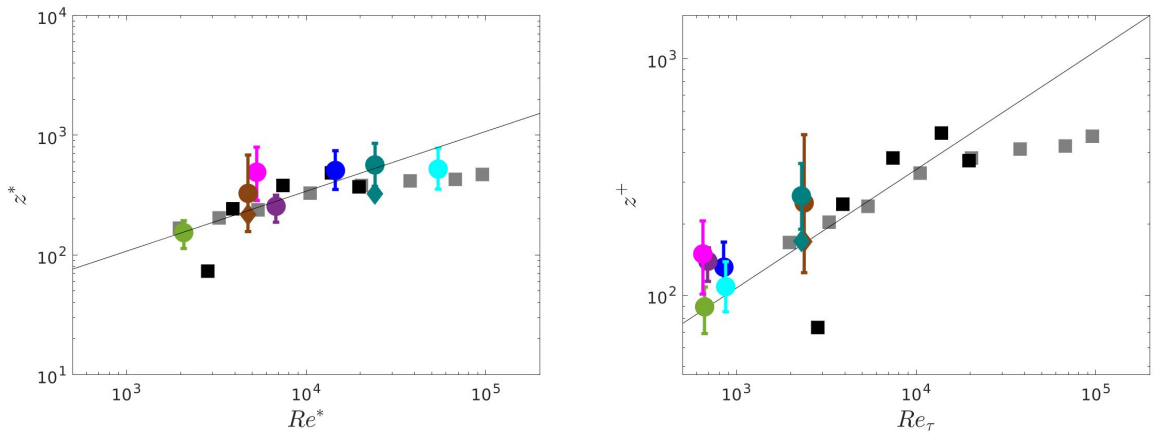

FIGURE 5.7. Wall normal location of LSP and VLSP in (A) semi-local length scale, z^*, vs Re^*. (B) viscous length scale, z^+, vs Re_τ. Grey squares are z^+ location of VLSP reported in ITBL study by Vallikivi et al. [107]. Black squares are z^+ location at $R_m = 0$ in ITBL study by Mathis et al. [99]. Solid black line in (A) and (B) correspond to $3.4Re_\tau^{0.5}$ provided by Mathis et al. [99]. Error bars denote the range of plateau in wall normal direciton. Circles and diamond denote LSP and VLSP, respectively. References to marker colors are included in table 3.4.

of plateau in streamwise wavenumber direction. Similar to the results in Fig. 5.7, k_x^* and k_x^+ in Fig. 5.8a and Fig. 5.8b, respectively, wavenumbers associated with VLSP exhibit a Reynolds number dependence similar to the VLSP trends reported by Vallikivi et al. [107] and Mathis et al. [99] where both k_x^* and k_x^+ associated with VLSP decrease as $0.02Re^{-0.5}$ as a function of Re^* and Re_τ, respectively. Moreover, perhaps without much surprise, a separate Reynolds number trend corresponding to LSP appears at higher wavenumber in k_x^* and k_x^+ as shown in Fig. 5.8. It is seen in Fig. 5.8 that the streamwise wavenumbers associated with LSPs in both inner length scales decrease as $0.12Re^{-0.5}$ where similar to VLSP, k_x^* shows dependency to Re^* and k_x^+ shows dependency to Re_τ.

Results in Fig. 5.7 and in Fig. 5.8 allow us to elaborate on the preliminary observation in section 5.3. The observation of Re_τ trend in both z^+ and k_x^+ reconfirms the consensus that Re_τ defines the separation of scale also for CTBL as expected. On the other hand, the Re^* trend in

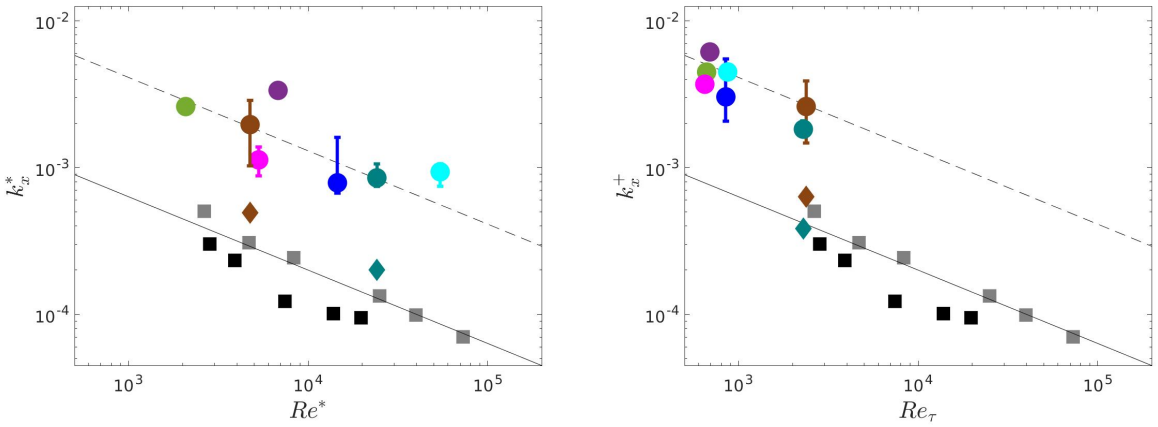

(A) (B)

FIGURE 5.8. Wavenumber of LSP and VLSP (A) k^* vs Re^*. (B) k^+ vs Re_τ. Grey squares and black squares are z^+ location of VLSP reported in ITBL study by Vallikivi et al. [107] and Mathis et al. [99], respectively. Solid black line in (A) and (B) correspond to $0.02Re_\tau^{-0.5}$ provided by Vallikivi et al. [107]. Dashed black line in (A) and (B) correspond to $0.12Re^{-0.5}$(Regardless of Re_τ or Re^*). Circles and diamond denote LSP and VLSP,respectively. References to marker colors are included in table 3.4.

both z^* and k_x^* similar to the ITBL Re_τ trend is confirmed up to Re^* of 55000. This observation suggests that the turbulence in the inner layer of CTBL with high Re^* behaves like high Re_τ flow under the effect of thermodynamic property gradient at least up to the wall normal position corresponding to LSP & VLSP even at low Re_τ condition.

It is also interesting to note that R34KM15 case with $Re_\tau \simeq 1900$ in a paper by Yao and Hussain [23] displays a second peak corresponding to the streamwise wavelength of VLSP (Fig.11c in Yao and Hussain [23]) while other cases in their study with lower Re_τ do not exhibit such peak. Together with results in Fig. 5.8 where VLSP only appears in cases with Re_τ larger than $Re_\tau = 2000$, this Reynolds number criteria support the Re_τ limit for VLSP to emerge suggested by Hutchins and Marusic [72] as discussed in section 5.3.

Moreover, a slight deviation of the k^* for M10T3 case from the expected trend is observed in Fig. 5.8a where M10T3 is a case with non-zero wall heat transfer rate, $-B_q$. It is seen that k^*

for M10T3 case results in a slightly higher k^* value than the predicted values from the ITBL trend. Higher cooling rate has been reported to attenuate the redistribution of near-wall streamwise turbulent kinetic energy to the other two directions [40, 45, 89, 90]. Recent paper by Cheng and Fu [104] demonstrated that there is high coupling between large turbulent structures in velocity and temperature fields in cases with high wall cooling where the turbulent structures in both fields behave as attached eddies affecting the near wall fluctuations. These results suggest that beyond the Re^* dependency, the additional heat transfer effect by the wall boundary condition also plays an important role in the determination of turbulence dynamics.

5.4.2 Outer Length Scale

While there is a general consensus that large turbulent structures are an outer scale phenomena and observed LSP and VLSPs are representative of LSM and VLSM, Vallikivi et al. [107] noted that the streamwise wavenumber of VLSP does not scale with neither a viscous length scale, z_τ, nor an outer length scale, δ. Based on this observation, they suggested that a new length scale for large turbulent structures may exist between z_τ and δ. Similar to their observation, it is clearly demonstrated in section 5.4.1 that when normalized by either inner length scale, the wall normal position and the streamwise wavenumbers of LSP and VLSP show Reynolds number dependency without showing a sign of scaling. Therefore, to confirm the observation of Vallikivi et al. [107], wall normal positions and streamwise wavenumbers of LSP and VLSP normalized by δ are plotted against Re_τ in Fig. 5.9a and Fig. 5.9b. Note that wall normal positions and streamwise wavenumbers normalized by δ are denoted by z/δ and $k_x\delta$. It is first seen in Fig. 5.9a that z/δ of both LSP and VLSP decreases with increasing Re_τ where the Re_τ trend follows

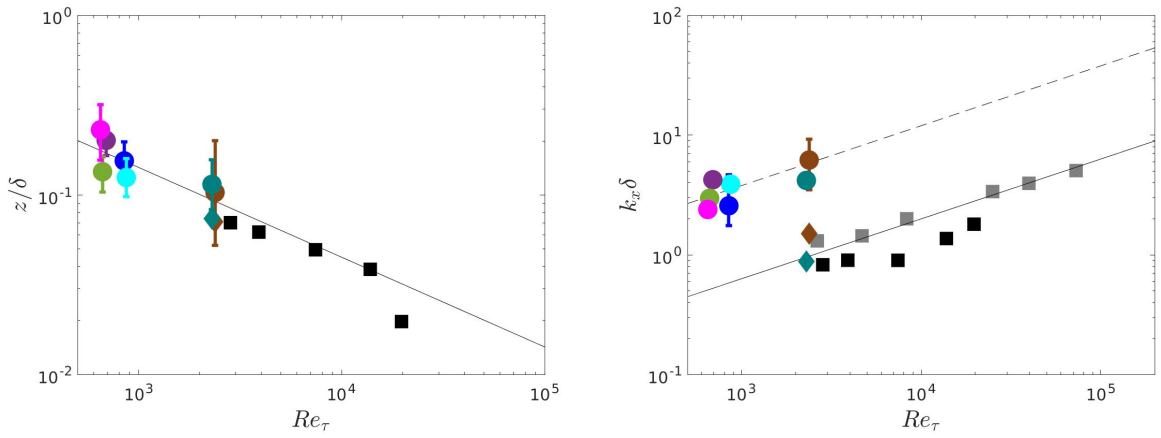

(A) (B)

FIGURE 5.9. (A) Wall normal location normalized by δ, z/δ (B) streamwise wavenumber normalized k_x/δ plotted against Re_τ. Grey squares and black squares in (A) and (B) are z/δ and $k_x\delta$ location of VLSP reported in ITBL study by Vallikivi et al. [107] and Mathis et al. [99], respectively. Solid black line in (A) correspond to $4.5Re_\tau^{-0.5}$. Solid black line in (A) correspond to $0.02Re_\tau^{0.5}$ given by Vallikivi et al. [107]. Dashed black line in (B) correspond to $0.12Re_\tau^{0.5}$. Circles and diamond denote LSP and VLSP,respectively. References to marker colors are included in table 3.4.

$4.5Re_\tau^{-0.5}$. On the other hand, $k_x\delta$ of VLSP is seen to increase with the trend line given by $0.02Re_\tau^{0.5}$ while $k_x\delta$ of LSP is seen to increase with the trend line given by $0.12Re_\tau^{0.5}$. The Re_τ trend for $k_x\delta$ of VLSP in Fig. 5.9b is identical to the Re_τ reported by Vallikivi et al. [107]. Therefore, it can be concluded that none of the length scales, i.e. outer length scale, viscous length scale and semi-local length scale is capable of scaling LSP or VLSP in present CTBL examination as well, supporting the notion that there should exist a new length scale capable of scaling the wavelength of LSM and VLSM as suggested by Vallikivi et al. [107]. Re^* trend based on outer length scale was not observed and is not plotted here. More discussion on the absence of Re^* trend is included in section 5.5.1.

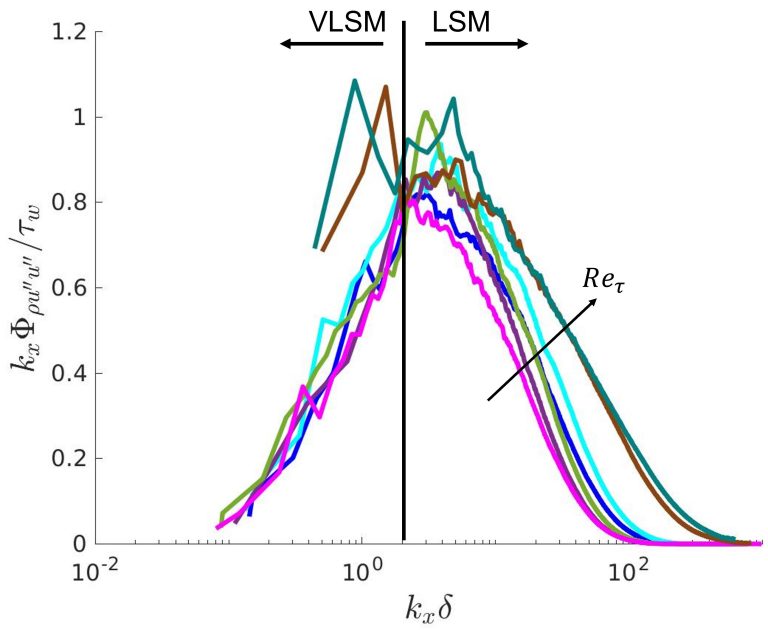

FIGURE 5.10. Pre-multiplied spectra normalized by wall shear stress, $k_x \phi_{\rho u'' u''} / \tau_w$, vs $k_x \delta$. References to line colors are included in table 3.4.

5.4.3 Turbulent Intensity in Large Turbulent Structures

While LSP & VLSP analysis in section 5.4.1 and section 5.4.2 are useful in the examination of the characteristic behaviors of wall normal locations and wavenumbers of LSM & VLSM, there exists a third dimensional information involving the magnitude of the pre-multiplied energy spectra in LSM & VLSM in which the area under the 2-D contour plot represents the magnitude of streamwise turbulent intensity. Therefore, to examine the energy content of large turbulent structures, the pre-multiplied spectra, $k_x \Phi_{\rho u'' u''} / \tau_w$, at wall normal locations of LSP & VLSP are plotted in Fig. 5.10 to showcase the typical behavior of pre-multiplied energy spectra involving LSM & VLSM across the wavenumber space. It is clearly visible in Fig. 5.10 that VLSP emerges in low wavenumber range for high Re_τ cases as discussed previously. More importantly, it is observed that the relative size of the area under the pre-multiplied spectra curve scales with

Re_τ rather than Re^*. This implies that the strength of large turbulent structures and therefore, the magnitude of the streamwise turbulent intensity near LSP & VLSP locations exhibit Re_τ dependence, not Re^*_τ. This agrees with an observation of streamwise turbulent intensity in Fig. 5.5b where an increase in Re_τ elevates the magnitude of the streamwise turbulent intensity in the log layer.

5.5 Implication of Reynolds Number Trend

5.5.1 The Role of Reynolds Numbers in the Inner Layer

In section 5.4, the Re_τ trend is exhibited when the wall-normal locations and wavenumbers of LSP and VLSP are normalized by viscous length scale. This is perhaps expected because Re_τ measures the separation of scale that is present in both realm of incompressible and compressible turbulent boundary layers. However, it was also demonstrated that when normalized by semi-local length scales, the wall-normal locations and wavenumbers of LSP and VLSP exhibit a Re^* trend akin to the Re_τ trend observed in ITBL studies [99, 107]. This observation is consistent with the new observations discussed in section 5.3, where the emergence of longer wavelength features in the log layer at higher Re^* CTBL cases corresponded with the LSM and VLSM trends reported in ITBL studies [107]. Moreover, it was repeatedly demonstrated that the near-wall turbulent statistics are better collapsed by the use of the semi-local length scale especially when cold wall CTBL cases are present. Therefore, it can be deduced that Re^* is expected to be a relevant parameter in describing the behavior or influence of large turbulent structures down to the wall from the wall normal location of VLSP. That is, the success of semi-local length scales in describing large turbulent structures in CTBL and their dependence on Re^* indicates that closer

to the wall, large turbulent structure behaves more locally under the influence of thermodynamic properties and allows CTBL to exhibit high Re_τ characteristics at high Re^*. On the other hand, the use of viscous length scale to scale near-wall turbulent statistics is widely reported to be less successful [2, 22, 23, 45]. It can then be deduced that, while Re_τ and the viscous length scale are relevant near the location of LSP and VLSP, Re_τ is expected to lose its relevance in describing the influence of large turbulent structures in the near-wall region. This notion is partly supported by the observation that the near-wall logarithmic growth of the turbulent intensity peak is only dependent on Re^* [2, 22, 23, 45]. Interestingly, when plotting z/δ and $k_x\delta$ at LSP and VLSP, a discernible Reynolds number trend is only observed for Re_τ but not for Re^*. This observation further reinforces the suggestion that Re^* cannot adequately describe the δ-scale motion of the large turbulent structures in the outer layer near the freestream. Rather, closer to the freestream, large turbulent structure behaves more in accordance with the Re_τ scaling observed in ITBL.This distinction might help explain why no strong outer peak in streamwise turbulence intensity is observed in high Re^* cases with low Re_τ, as is typically seen in incompressible flows.

Furthermore, it is observed that the magnitude of the turbulent intensity at LSP and VLSP grows as Re_τ increases, as demonstrated in Fig. 5.10. This suggests that the strength of large turbulent structures remains constant at the same Re_τ. This observation introduces more questions more than answers. That is, in ITBL, near-wall high Re_τ trends in turbulent intensities are associated with amplitude modulation of the near-wall turbulence by the large turbulent scales in the log layer. Therefore, the results presented here in Fig. 5.10 would suggest that the near-wall turbulent intensity peak and Re_τ are positively correlated in CTBL. However, as demonstrated in Fig. 5.5b, the turbulent intensity peak in CTBL actually decreases as Re_τ is increased. Rather, the near-wall turbulent intensity peak increases with Re^* as demonstrated in Fig. 5.5a and several

CTBL studies [23, 24, 45, 106]. Therefore, the correct interpretation of the results would be that the the large turbulent scales in the log layer of which the strength scales with Re_τ, are modified through the changes in local fluid properties such that the scale interaction near the wall increases as Re^*.

Summarizing the implications of the results provided so far, it is then possible to draft an instructive map as shown in Fig. 5.11 which entails generic regions of influence by Re_τ and Re^* in the determination of large turbulent structure behavior. It is provided to easily visualize the summary of all implications of results provided so far. First, closer to the wall denoted by yellow region, the location, wavelength and strength of large turbulent structures or turbulent motions modulated by large turbulent structures are determined by Re^* and semi-local length scale. Second, closer to the freestream denoted by blue region, the location, wavelength and strength of large turbulent structures are determined by Re_τ and outer length scale. There also exists the overlap layer denoted by green region where the location, wavelength of large turbulent structures are determined by both Re^* and Re_τ, and all three length scales (Re^* with semi-local length scale and Re_τ with viscous and outer length scales). The strength of large turbulent structures in the overlap region is solely determined by Re_τ. Note that while onset location (lower bound) of the overlap region is not precisely determined, the upper limit can be determined to be the location of LSP & VLSP. The determination of the lower bound requires a further analysis which is not within the scope of this study.

To further understand why LSP and VLSP exhibit these Reynolds number behaviors, it is worth discussing the concept of a boundary layer region referred to as the mesolayer. The mesolayer is defined as the region below the logarithmic layer, where viscous effects become more pronounced for turbulent length scales. This region is also where interactions between all

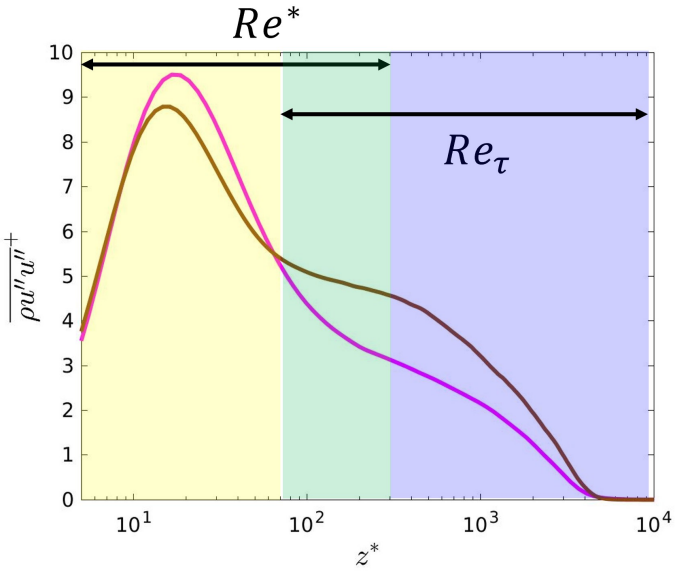

FIGURE 5.11. Generic turbulent intensity map that represents the locations of Re^* and Re_τ influence in the description of large turbulent structures. Yellow region denotes the near-wall region with Re^* influence, blue region denotes the outer region with Re_τ influence and green region denotes the overlap region with both Re^* and Re_τ influence.

turbulent length scales, from the smallest to the largest, are the most significant. The existence of the mesolayer has been associated with O($\sqrt{Re}$) behaviors in various studies [110, 111]. Based on the observed $\sqrt{Re_\tau}$ trend of z^+ at VLSP, Vallikivi et al. [107] suggested that z^+ at VLSP could mark the outer boundary of a mesolayer-like region. However, it's important to note that this observed $\sqrt{Re_\tau}$ trend stems from different arguments in previous studies [110, 111].

As demonstrated throughout section 5.4, z^+ and z^* at LSP & VLSP exhibit $\sqrt{Re}$ trend regardless of which Reynolds number is used with an exception of the Re^* range above 20000 very similar to the results in Vallikivi et al. [107]. Recently, Lee et al. [1] developed a mean velocity transformation (U_G) for CTBL based on total momentum equation that successfully scaled CTBL cases. Results of their mean velocity transformation for CTBL cases representative of the Re^* range and Re_τ range used in the present study are displayed together with streamwise turbulent kinetic energy, and wall normal locations of LSP and VLSP in Fig. 5.12. Similar to

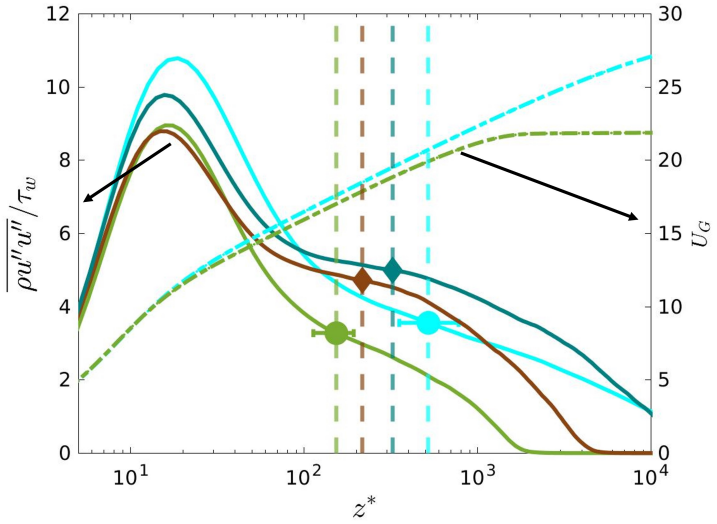

FIGURE 5.12. Normalized streamwise turbulent intensity,$\overline{\rho u'' u''}/\tau_w$ on the left y-axis and generalized mean velocity transformation proposed by Lee et al. [1] on the right y-axis. x-axis shows semi-local wall normal position, z^*. Error bars denote the size of plateau in wall normal direction. Circle and diamond denote wall normal position of LSP and VLSP, respectively. References to line and marker colors are included in table 3.4.

the results of Vallikivi et al. [107], z^* at LSP & VLSP in Fig. 5.12 corresponds to the center of the logarithmic region in the transformed mean velocity profile. With regard to the turbulence intensity, it can be seen that the locations of VLSP in M2H and M6H case in Fig. 5.12 correspond to the start of the logarithmic layer in streamwise turbulent kinetic energy as suggested by Vallikivi et al. [107]. Given that z^* in Fig. 5.7 also follows O($\sqrt{Re^*}$), it may be inferred that even cases with low Re_τ and high Re^* retain the intermediate layer akin to the layer Vallikivi et al. [107] referred to. Also, the suggested intermediate layer is approximately consistent with the overlap layer in Fig. 5.11.

Based on these findings, it is then possible to modify the logarithmic tangent line to the intermediate region of turbulent intensity (approximately the mesolayer according to the definition of Vallikivi et al. [107]) proposed by Samie et al. [98] to be suitable for CTBL. Samie et al. [98] suggested a Re_τ based relationship in their ITBL study to predict the location ($z^+_{p,int}$),

magnitude ($\overline{u'u'}^{+}_{p,int}$) and slope ($S_{int}$) at the 'intersection' point between the intermediate region and the logarithmic outer layer of turbulent intensity. These quantities were then used to derive a logarithmic tangent line to the intermediate region. They argued, while the intersection point is not exactly equal to the VLSP location, it is an outer bound for VLSP. In CTBL, z^* is demonstrated to be a useful variable to show self similar behavior of $\overline{\rho u'' u''}$ [2, 23, 24, 106]. Therefore, based on our finding that wall normal location of LSP & VLSP are closely linked with Re^* in semi-local length scaling, it is proposed to replace Re_τ with Re^* to predict the z^* location of the 'intersection' point, $z^*_{p,int}$, as shown in Eq. 5.1. On other hand, the slope, S_{int}, and the magnitude of the turbulence intensity at the intersection, $\overline{\rho u'' u''}^{+}_{p_{int}}$ are unchanged from the original relationship to be functions of Re_τ as shown in Eq. 5.3 and Eq. 5.2. The use of Re_τ in quantities related to the magnitude of the turbulent intensity is supported by the observation we have made above and Fig. 5.10. Resulting modified equations of Samie et al. [98] which describes the logarithmic tangent line to the intermediate region in CTBL are presented in Eq. 5.4. Note that the same constants proposed by Samie et al. [98] are used.

$$z^*_{p_{int}} = 32.66(Re^*)^{0.27} \tag{5.1}$$

$$\overline{\rho u'' u''}^{+}_{p_{int}} = -3.06 + 0.99 \log(Re_\tau) \tag{5.2}$$

$$S_{int} = -2.74 + 0.28 \log(Re_\tau) \tag{5.3}$$

$$\overline{\rho u'' u''}^{+} = \overline{\rho u'' u''}^{+}_{p_{int}} + S_{int} \log\left(\frac{z^*}{z^*_{p_{int}}}\right) \tag{5.4}$$

Fig. 5.13 shows CTBL cases representative of the Re^* range and Re_τ range used in the

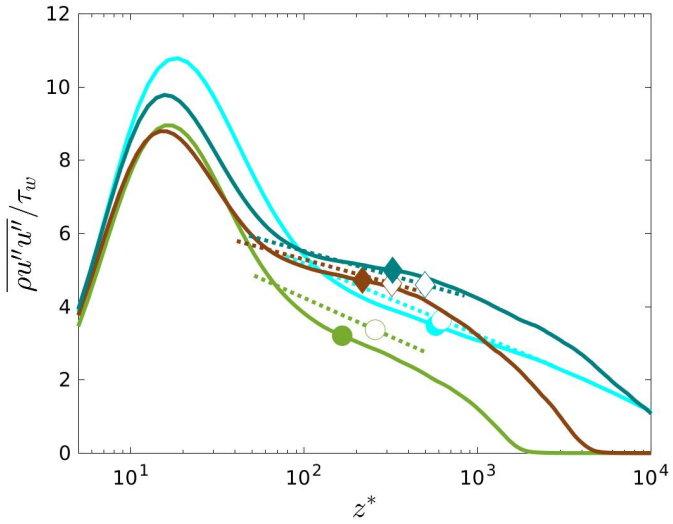

FIGURE 5.13. Normalized streamwise turbulent intensity,$\overline{\rho u'' u''}/\tau_w$ denoted by solid line and logarithmic tangent line to the intermediate region denoted by dotted line. x-axis shows semi-local wall normal position, z^*. Filled circle and diamond denote LSP and VLSP locations, respectively. Empty circle and diamond denote intersection point for the corresponding LSP and VLSP with the same color. References to colors are included in table 3.4.

study. While not perfect, the tangent lines predicted by Eq. 5.4 capture the intermediate region of streamwise turbulent intensity as shown in Fig. 5.13 except for M3T5 which is the lowest Re^* case used present study. Samie et al. [98] calibrated the constants based on ITBL cases that exhibit a clear intersection point, i.e. cases with $Re_\tau > 6000$. Therefore, the performance is expected to deteriorate for low Reynolds number cases. A calibration of coefficients including the CTBL cases in the present study is expected to improve the prediction capability of the modified Samie model for higher Reynolds number cases. Furthermore, the success of the modified model supports that Re^* and semi-local length scale are capable of describing the location and the wavelength of turbulence while the magnitude is determined by Re_τ in this intermediate region (approximately the overlap region in Fig. 5.11) below LSP & VLSP wall normal location.

5.5.2 Length Scales Between Small Scale and Large Scale

To determine the length scale between small turbulent scales and large turbulent scales, the relative contribution of large turbulent structures (effectively combining the influence of both LSM and VLSM) to streamwise turbulent intensity in the buffer layer and the intermediate region is examined. For this analysis, we utilize integrated variable Γ_T given in Eq. 5.5 similar to the one given by Balakumar and Adrian [100].

$$\Gamma_T = \frac{\int_{\Delta z} \int_{\Delta k_x} k_x \Phi_{\rho u'' u''} \, d\left(\ln k_x\right) \, dz}{\int_{\Delta z} \int_0^{\infty} k_x \Phi_{\rho u'' u''} \, d\left(\ln k_x\right) \, dz} \tag{5.5}$$

In particular, we are interested in the relative contribution of LSM and VLSM to streamwise TKE between the buffer layer (i.e. $z^* > 50$) and wall normal locations of LSP and VLSP. Furthermore, the respective spectral limits between the small turbulent scales and large turbulent scales are determined in terms of all three length scales available, i.e. viscous length scale, semi-local length scale and outer length scale where each wavelength cut-off are given by $\lambda_x^+ = 1000$, $\lambda_x^* = 2000$ and $\lambda_x/\delta = 1.0$. The wavelength between the small scale and the large scale are determined by visually inspecting the pre-multiplied energy spectra plots in each scaling so that the wavelength lies between the ISP and LSP. Therefore, Δk_x in Eq. 5.5 is measured from the lowest k_x to the k_x corresponding to the predetermined wavelength in each length scale. Based on these predetermined bounds, Γ_T with different wavelengths are plotted in Fig.5.14 using the CTBL dataset in table 3.4. Note that M10T3 has not been included in this analysis due to cold wall effect. It should also be clarified that the wavelengths used here does not necessarily represent the exact wavelength that divides the small scale and large scale as will be discussed below.

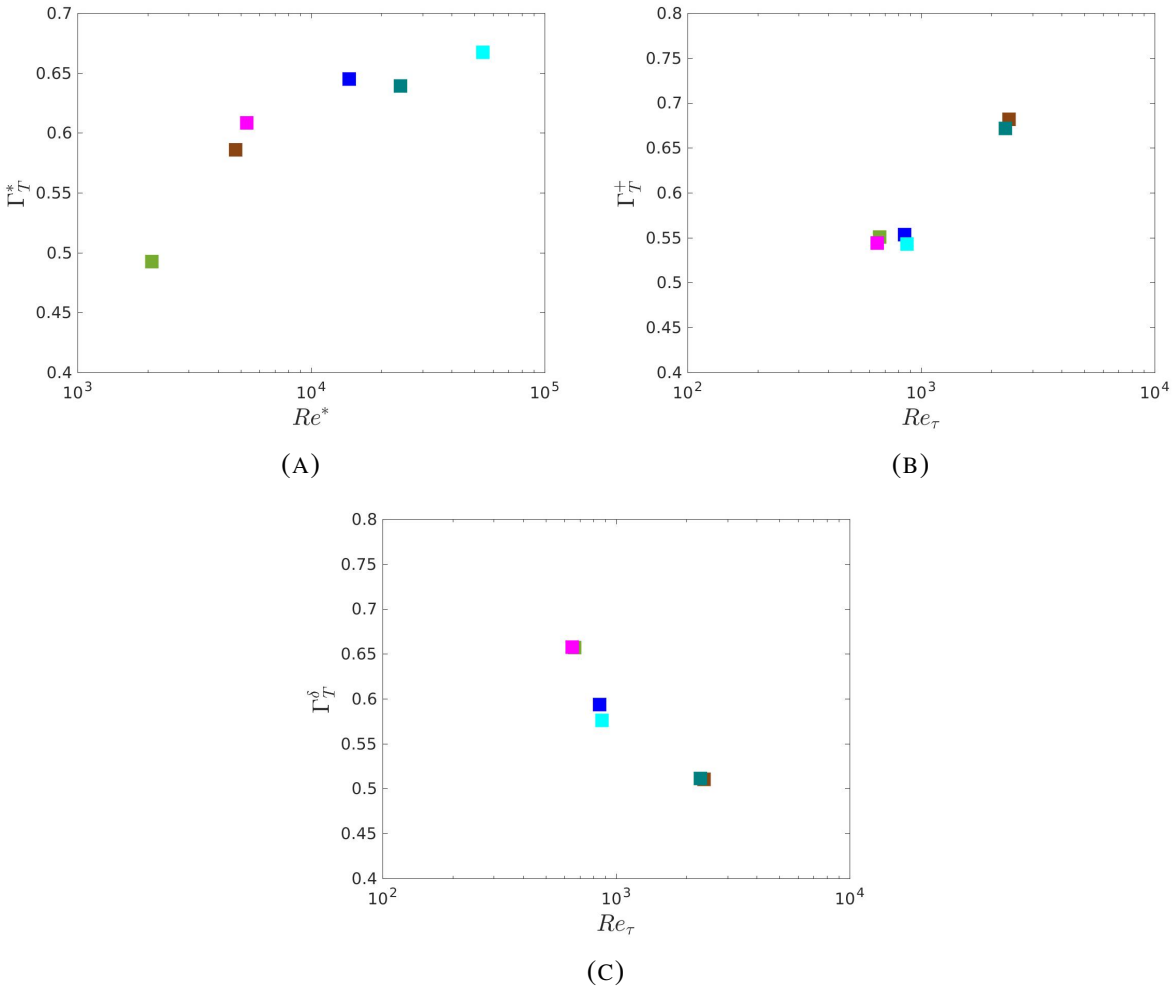

FIGURE 5.14. Relative contribution of large turbulent structures with (A) semi-local length scale wavelength cut-off, Γ_T^* vs Re^* (B) viscous length scale wavelength cut-off, Γ_T^+, vs Re_τ (C) outer length scale wavelength cut-off, Γ_T^δ, vs Re_τ. Reference to colors is included in table 3.4.

Nonetheless, because the spectral location of the wavelength used here lies between the ISP and LSP&VLSP, the Reynolds number dependent trend observed remains intact, corroborated by additional sensitivity study included in Appendix C that examined the effect of changing the wavelength in each length scales. Moreover, it is also seen that increasing the outer wall normal position bound to the edge of the boundary layer does not change the Reynolds number trend observed in Fig. 5.14.

Fig. 5.14 includes the relative contribution of large turbulent structures to streamwise

turbulent intensity using wavelength cut-offs based on the three length scales available denoted by Γ_T^*, Γ_T^+ and Γ_T^δ in Fig. 5.14a, Fig. 5.14b and Fig. 5.14c,respectively. Both Γ_T^* and Γ_T^+ which use wavelength cutoffs based on inner length scales, are seen to increase with Re^* and Re_τ, respectively, while Γ_T^δ is seen to decrease with Re_τ. As Marusic et al. [109] noted, an absolute magnitude of the contribution of small turbulent scales to turbulent intensities should remain relatively constant across a range of Reynolds numbers while an absolute magnitude of the contribution of large turbulent scales to turbulent intensities should grow with Reynolds number. It would suggest that Γ_T increases with Reynolds numbers. With this in mind, however, it is perhaps possible to conclude from Fig. 5.14 that the use of both inner length scale defined wavelength cut-offs is supported while the use of outer length scale defined wavelength cut-offs is not. However, we argue that such interpretation is misguided and the results presented here are simple ramifications of the previously provided assertion in section 5.4.2 and by Vallikivi et al. [107] that all three length scales are not capable of scaling LSP & VLSP. That is, since the wavelength of LSP & VLSP scaled by δ decreases as Re_τ increases as can be inferred from Fig. 5.9b, the use of a singular δ scaled wavelength cutoff causes Γ_T^δ to neglect a portion of LSM & VLSM as Re_τ increases, resulting in the decrease of Γ_T^δ. It is then possible to infer that Γ_T^* and Γ_T^+ are overpredicted as Re^* and Re_τ are increased, respectively, when singular wavelength cutoffs are used. Therefore, a wavelength based on a new length scale that scales LSP & VLSP or Reynolds number dependent wavelength (Re^* when using semi-local length scale or Re_τ when using viscous or outer length scale) should be used to separate the small scales and the large scales.

5.6 Summary

In this chapter, the Reynolds number trends of large turbulent structures in CTBL are examined using pre-multiplied energy spectra of $\rho u''u''$ velocity signal calculated from CTBL database with Re^* ranging from 3000 to 55000 [1] and Re_τ ranging form 600 to 2300 [2]. Reynolds number dependence of wall normal positions, wavenumbers and magnitudes of pre-multiplied energy spectra at LSP and VLSP normalized by the viscous, semi-local and outer length scales have been observed. The ITBL result that Re_τ determines the separation of scale also for CTBL is confirmed. More importantly, z^* and k_x^* at LSP & VLSP are demonstrated to be a function of Re^* up to 55000. It is also seen that the strength of large turbulent structures at LSP & VLSP scales with Re_τ with an direct implication that the magnitude of turbulent intensity in the log layer grows with Re_τ. This result and its possible implication from ITBL theories collide with an observation that the near-wall turbulent intensity peak grows with Re^*. However, based on the observed Re^* trend of z^* and k_x^* at LSP and VLSP, it is argued that the large turbulent scales in the log layer are modified through the changes in local fluid properties such that the scale interaction near the wall increases as Re^*. Furthermore, while components of Re_τ, i.e. viscous length scale and outer length scale, measure the separation of scale in CTBL, the thermodynamic properties influence the turbulence in the inner layer so that turbulence behaves locally and like a high Reynolds number flow dictated by Re^* even when Re_τ is low. This local thermodynamic effect is suggested to attenuate as freestream is approached where Re_τ is important.

The observed Reynolds number trends in both wall normal location and wavenumbers at LSP & VLSP follow $\mathcal{O}\left(\sqrt{Re}\right)$ behavior similar to the ITBL Re_τ trend [99, 107]. Vallikivi et al. [107] noted that an $\mathcal{O}\left(\sqrt{Re}\right)$ behavior is linked with the characteristics of mesolayer and

suggested that an intermediate layer bounded by VLSP to be similar to the mesolayer suggested by others [110, 111] despite being derived from a different approach. The intermediate layer is also observed in z^* even for CTBL cases with low Re_τ but high Re^*. In this layer, semi-local length scale as well as the viscous length scale and outer scale, all remain relevant as demonstrated by the $\mathcal{O}\left(\sqrt{Re}\right)$ behavior of LSP & VLSP seen in section 5.4.1 and section 5.4.2.

Based on these findings, a modified relationship from Samie et al. [98] has been proposed to predict a logarithmic tangent line to turbulent intensity in the intermediate layer based on parameters at 'intersection' location (analogous to VLSP location). In the modified relationship, all parameters are unchanged from the original relationship except for the prediction of intersection of semi-local wall normal location where Re_τ in the original equation is replaced by Re^*. This change reflects the Reynolds number trend observed in CTBL. While the prediction results from the modified relationship are not perfect especially for low Re^* data, the difference emerges from the constants used in the model were calibrated using high Re_τ ITBL cases ($Re_\tau > 6000$). A partial success of the modified Samie model supports the conclusion made on the role of Re^* and Re_τ in describing the turbulence in the inner of CTBL.

The length scales between the small turbulent scale and large turbulent structures based on all three different length scales available have also been examined and discussed by calculating a relative contribution of large turbulent structures to turbulent intensity, Γ_T. By comparing the Reynolds number trend of wavelength scaled by different length scales and the results from Γ_T analysis, the use of a singular value of λ_x^* and λ_x^+ cut-off with varying Reynolds numbers is determined to be inadequate of accurately differentiating the small scales and the large scales. Based on these results, it is determined that a new length scale is derived to scale LSP & VLSP or Reynolds number dependent length scale is used to separate the large turbulent scales and the

small turbulent scales.

Chapter 6: Conclusions

6.1 Key Results & Contributions

A CTBL DNS CRoCCo Lab dataset [1] presented in Chapter 3 has been used to investigate the effect of a wall temperature and freestream Mach number to CTBL in hypersonic regime. To examine these effects, the database consists of CTBL cases incorporating wall-cooling, semi-local Reynolds numbers ranging from 800 to 34000, and Mach numbers up to 12. The CRoCCo code uses low storage 3rd order Runge-Kutta method by [81] for time marching, 4th order central scheme for numerical representation of the diffusion term and 4th order bandwidth optimized WENO scheme for the numerical representation of the convection term. The generation of the inflow conditions is handled by utilizing the rescaling method by Xu & Martin [87]. The boundary conditions and initialization procedures used to create the high-fidelity CRoCCo Lab CTBL database for this study are documented and have been verified in previous studies [9, 79, 86, 87].

In Chapter 4, the impact of density and viscosity fluctuations on the overall stress balance is identified in order to develop a new method for transforming mean velocity in compressible boundary layers. In the process, the significance of density and viscosity fluctuations in relation to momentum balance and various types of stresses (viscous, turbulent, and total) is highlighted. Moreover, two important properties that have been overlooked in previous velocity transformation

derivations are discussed: (1) the Mach-invariance of near-wall momentum balance for the generalized total stress, and (2) the Mach-invariance of the relative contributions of generalized viscous and Reynolds stresses to the total stress. Our proposed velocity transformation combines these properties into a single equation, resulting in the successful convergence of all considered compressible cases to the incompressible law of the wall. The parameters of mean velocity transformation for all cases fall within the reported range of log layer slope and intercept values for incompressible data. The success of our newly proposed transformation can be attributed to its incorporation of the effects of viscous stress, turbulent stresses, and mean and fluctuating density viscosity into a unified transformation form, based on the underlying physics of these two scaling properties.

In Chapter 5, the Reynolds number trends of large turbulent structures in CTBL are investigated. Using CTBL database with Reynolds numbers ranging from Re^* = 3000 to 55000 and Re_τ = 600 to 2300 (with momentum based boundary layer thickness), pre-multiplied energy spectra based on $\rho u'' u''$ velocity signal are analyzed. The results show that z^* and k_x^* at LSP and VLSP vary with Re^* up to 55000, exhibiting a very similar high Re_τ trend observed in ITBL studies [99, 107]. Additionally, the strength of large turbulent structures at LSP and VLSP are seen to increase with Re_τ. This result is arguably inconsistent with the observation of near-wall turbulent intensity peak growing with Re^*. This discrepancy as well as observed Re^* behavior at LSP & VLSP are attributed to modifications in local fluid properties, leading to increased scale interaction near the wall as Re^* rises. That is, it is argued that closer to the wall, i.e. inner layer, CTBL flow behaves like Re^* flow while closer to the freestream,i.e. outer layer, flow behaves like Re_τ flow.

The study also examines the Reynolds number dependency of the length scale between small and large turbulent scales. An analysis using relative contributions of large turbulent

structures to turbulent intensity indicates that using a uni-variate wavelength cut-offs based on viscous, semi-local and outer length scales to separate the small scales and the large scales are inappropriate. Instead, a derivation of a new length scale that scales the large turbulent structures or the use of Reynolds number-dependent wavelength cut-offs are suggested. Overall, the study provides insights into the Reynolds number trends of large turbulent structures in CTBL, highlighting the role of both Re^* and Re_τ on turbulence characteristics.

This thesis has made contributions in several important aspects to the state of art in the analysis of physics and modelling pertaining to compressible turbulent boundary layer. In particular, this advancement is expected to contribute to the development of WMLES. Listed below are a summary of main contributions of this thesis.

- The analysis of the CTBL DNS database presents a broadening of our understanding of CTBL in the hypersonic regime across a wide range of wall cooling and hypersonic freestream velocity conditions that represent realistic hypersonic flight conditions.

- An investigation of the important physics in CTBL using TSL momentum equations has revealed a departure from the conventional consensus in that thermodynamic property fluctuations, such as density and viscosity fluctuations, are not negligible in the consideration of CTBL.

- A thermodynamic property fluctuation-corrected total stress is demonstrated to be mach-invariant in magnitude and ratio, enabling the development of an accurate description of the transformed mean velocity across a wide range of freestream Mach numbers and wall cooling conditions.

- The investigation regarding the role of Re^* and Re_τ in the description of the behavior

of LSM and VLSM in the log layer confirms Reynolds number trends and reveals the dependence of the characteristic wall-normal positions and wavenumbers on Re^* and the semi-local length.

- It is demonstrated that throughout the inner layer, CTBL flow is characterized by Re^*. In contrast and similar to ITBL, it is found that Re_τ characterizes the flow in the outer layer. In agreement with the description of different layers in ITBL, there also exists an overlap layer characterized by both Re^* and Re_τ in CTBL.

6.2 Future Investigations

While the examination of different turbulent quantities in CTBL provided in this dissertation is pivotal in the development of turbulence models, there is still much work to build upon present findings to achieve this goal. One research immediately applicable to the results presented in this dissertation is the development of a transformation kernel to relate law of the wall and the suggested mean velocity transformation. Such study will provide a missing piece in providing an accurate mean velocity profile in physical units.

Moreover, the examination of large turbulent structures and their Reynolds number trend is a precursor study that provides necessary information in order to develop a near-wall turbulence prediction model. Therefore, a development of a turbulent intensity prediction model for CTBL would be a natural next step in continuing with the results provided in this study.

Appendix A: Derivation of Thin Shear Layer Momentum Equation

A.1 Reynolds-Averaged TSL Equation with density fluctuation

The derivation of Reynolds-averaged TSL equation with density fluctuation starts from a two-dimensional momentum equation with homogeneous spanwise direction assumption provided below,

$$\frac{\partial \rho u}{\partial t} + \frac{\partial}{\partial x}\left[\rho u u\right] + \frac{\partial}{\partial z}\left[\rho u w\right] = -\frac{\partial P}{\partial x} + \frac{\partial}{\partial x}\left[\frac{2}{3}\mu\left(2\frac{\partial u}{\partial x} - \frac{\partial w}{\partial z}\right)\right] + \frac{\partial}{\partial z}\left[\mu\left(\frac{\partial u}{\partial z} + \frac{\partial w}{\partial x}\right)\right]$$

Assuming steady state, fully-developed, zero-pressure gradient flow, above equation reduces to,

$$\frac{\partial}{\partial z}\left[\rho u w\right] = \frac{\partial}{\partial z}\left[\mu\left(\frac{\partial u}{\partial z} + \frac{\partial w}{\partial x}\right)\right]$$

Then, Reynolds-averaged decomposition operation is performed as shown below,

$$\rightarrow \frac{\partial}{\partial z}\left[\left(\overline{\rho} + \rho'\right)\left(\overline{u} + u'\right)\left(\overline{w} + w'\right)\right] = \frac{\partial}{\partial z}\left[\left(\overline{\mu} + \mu'\right)\left(\frac{\partial\left(\overline{u} + u'\right)}{\partial z} + \frac{\partial\left(\overline{w} + w'\right)}{\partial x}\right)\right]$$

$$\rightarrow \frac{\partial}{\partial z}\left[\overline{\rho u w} + +\cancel{\overline{\rho' u w}} + \overline{\rho u}\cancel{\overline{w'}} + \overline{\rho' w' u} + \overline{\rho w}\cancel{\overline{u'}} + \overline{\rho' u' w} + \overline{\rho u' w'} + \overline{\rho' u' w'}\right] =$$
$$\frac{\partial}{\partial z}\left[\overline{\mu}\frac{\partial \overline{u}}{\partial z} + \overline{\mu}\cancel{\frac{\partial \overline{w}}{\partial x}} + \overline{\mu}\cancel{\frac{\partial \overline{u'}}{\partial z}} + \cancel{\overline{\mu}\frac{\partial \overline{w'}}{\partial x}} + \cancel{\overline{\mu'}\frac{\partial \overline{u}}{\partial z}} + \cancel{\overline{\mu'}\frac{\partial \overline{w}}{\partial x}} + \overline{\mu'}\frac{\partial \overline{u'}}{\partial z} + \cancel{\overline{\mu'}\frac{\partial \overline{w'}}{\partial x}}\right]$$

In the next step, apply TSL assumption and the resulting equation is identical to Eq. 4.3

$$\rightarrow \frac{\partial}{\partial z}\left[\overline{\rho u w}+\overline{\rho' w' \overline{u}}+\overline{\rho' u' \overline{w}}+\overline{\rho} \overline{u' w'}+\overline{\rho' u' w'}\right]=\frac{\partial}{\partial z}\left[\overline{\mu} \frac{\partial \overline{u}}{\partial z}+\overline{\mu'} \frac{\partial \overline{u'}}{\partial z}\right]$$

A.2 Favre-Averaged TSL Equation with density fluctuation

The derivation of Favre-averaged TSL equation follows an identical procedure as in the previous section for Reynolds-averaged TSL equation. Assuming steady, fully-developed, zero-pressure gradient flow, two-dimensional momentum equation is reduced to,

$$\frac{\partial}{\partial z}[\rho u w]=\frac{\partial}{\partial z}\left[\mu\left(\frac{\partial u}{\partial z}+\frac{\partial w}{\partial x}\right)\right]$$

Then, Favre-averaged decomposition operation is performed as shown below,

$$\rightarrow \frac{\partial}{\partial z}\left[(\overline{\rho}+\rho')\left(\tilde{u}+u''\right)\left(\tilde{w}+w''\right)\right]=\frac{\partial}{\partial z}\left[(\overline{\mu}+\mu')\left(\frac{\partial\left(\tilde{u}+u''\right)}{\partial z}+\frac{\partial\left(\tilde{w}+w''\right)}{\partial x}\right)\right]$$

$$\rightarrow \frac{\partial}{\partial z}\left[\overline{\rho} \tilde{u} \tilde{w}+\cancel{+\overline{\rho}} \tilde{u} \tilde{w}+\cancel{\overline{\rho} \tilde{u} \overline{w''}+\overline{\rho' w''} \tilde{u}}+\cancel{\overline{\rho} \tilde{w} \overline{u''}+\overline{\rho' u''} \tilde{w}}+\overline{\rho} \overline{u'' w''}+\overline{\rho' u'' w''}\right]=$$
$$\frac{\partial}{\partial z}\left[\overline{\mu} \frac{\partial \overline{u}}{\partial z}+\cancel{\overline{\mu} \frac{\partial \overline{w}}{\partial x}}+\overline{\mu} \frac{\partial \overline{u''}}{\partial z}+\cancel{\overline{\mu} \frac{\partial \overline{w''}}{\partial x}}+\cancel{\overline{\mu'}} \frac{\partial \overline{u}}{\partial z}+\cancel{\overline{\mu'} \frac{\partial \overline{w}}{\partial x}}+\overline{\mu'} \frac{\partial \overline{u''}}{\partial z}+\cancel{\overline{\mu'} \frac{\partial \overline{w''}}{\partial x}}\right]$$

Resulting equation is shown below and is a pre-cursor equation to Eq. 4.6.

$$\rightarrow \frac{\partial}{\partial z}\left[\overline{\rho} \tilde{u} \tilde{w}+\widetilde{+\overline{\rho} u'' w''}\right]=\frac{\partial}{\partial z}\left[\overline{\mu} \frac{\partial \overline{u}}{\partial z}+\overline{\mu} \frac{\partial \overline{u''}}{\partial z}+\overline{\mu'} \frac{\partial \overline{u''}}{\partial z}\right]$$

Appendix B: Pre-multiplied Spectra

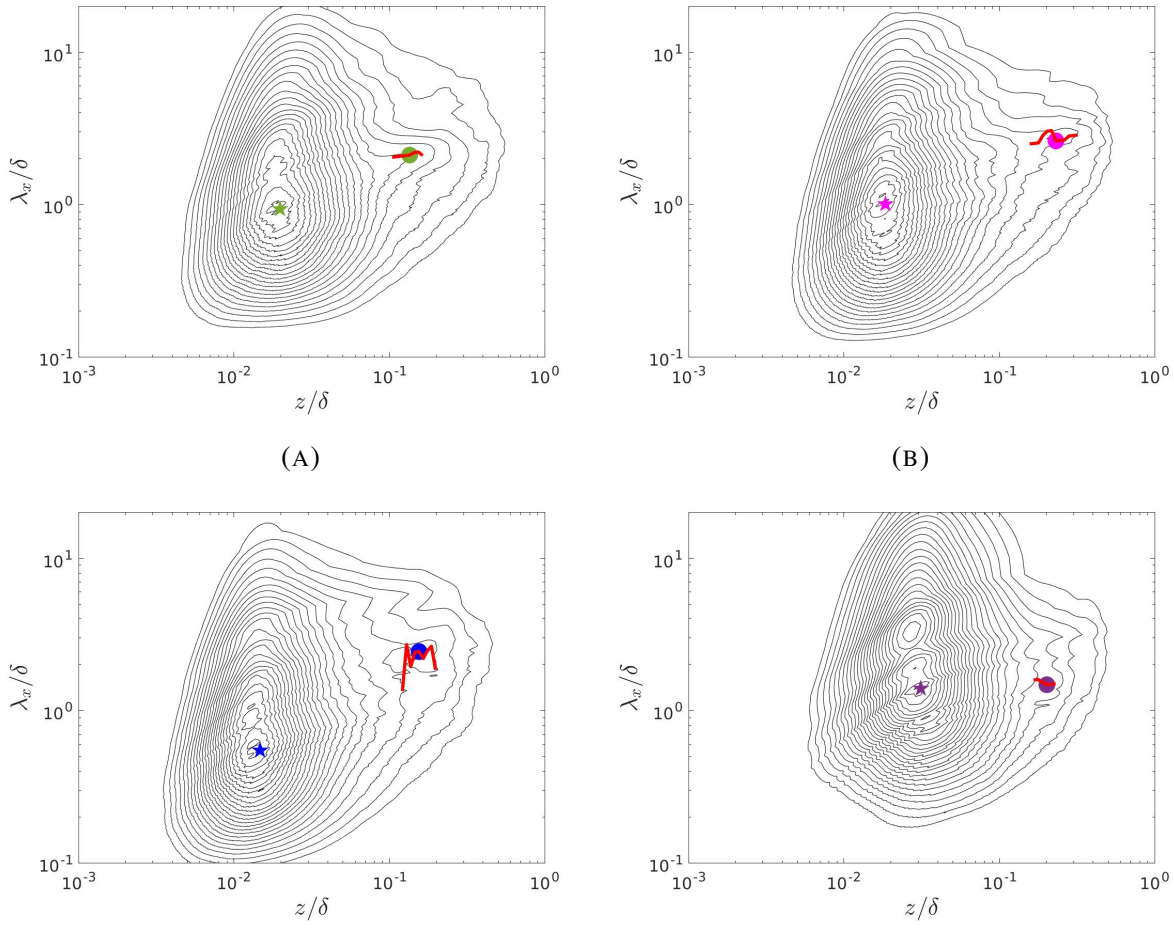

FIGURE B.1. Pre-multiplied energy spectra based on $\rho u'' u''/\tau_w$ velocity signal plotted against wall normal position, z, in x-axis and streamwise wavelength, λ_x, in y-axis. Wall normal position and wavelength are normalized by the outer scale, δ. (A) M3T5 (B) M5T5 (C) M7T5 (D) M10T3

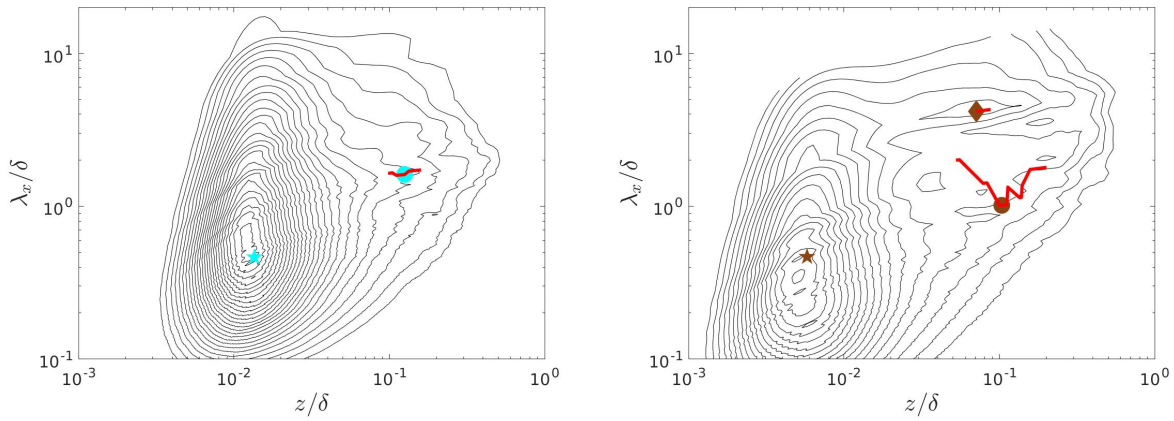

(A)

(B)

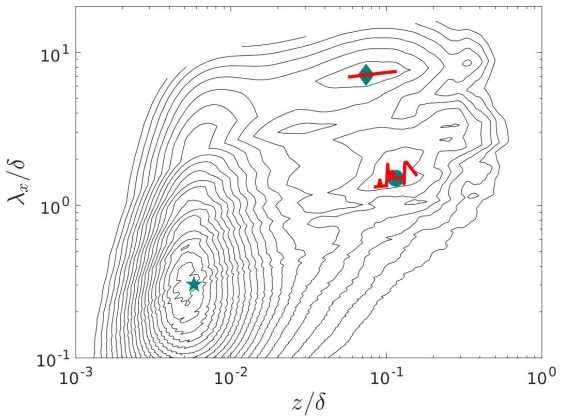

(C)

FIGURE B.2. Pre-multiplied energy spectra based on $\rho u'' u''/\tau_w$ velocity signal plotted against wall normal position, z, in x-axis and streamwise wavelength, λ_x, in y-axis. Wall normal position and wavelength are normalized by the outer scale, δ. (A) M12T5 (B) M2H (C) M6H

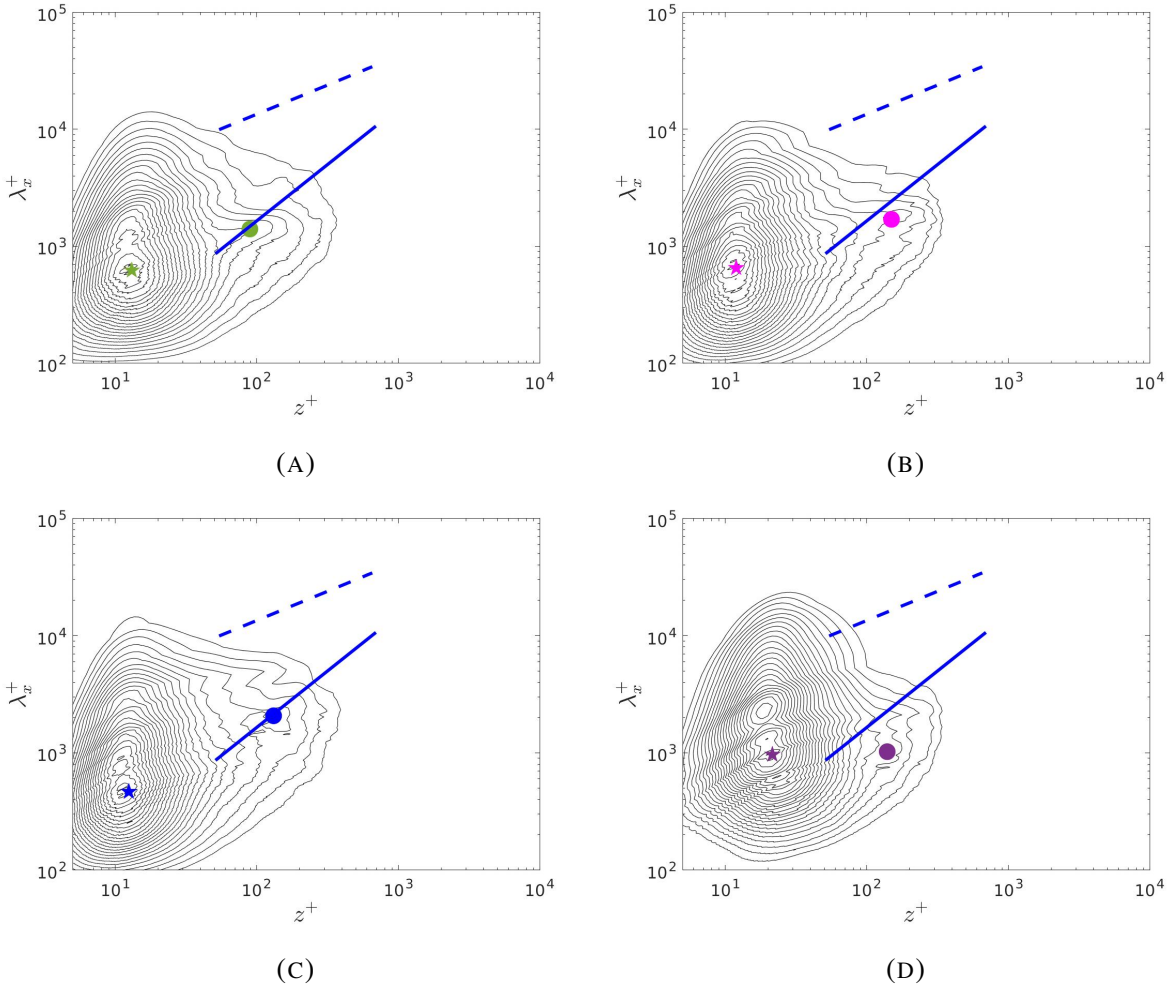

FIGURE B.3. Pre-multiplied energy spectra based on $\rho u'' u''/\tau_w$ velocity signal plotted against wall normal position, z, in x-axis and streamwise wavelength, λ_x, in y-axis. Wall normal position and wavelength are normalized by the viscous length scale. (A) M3T5 (B) M5T5 (C) M7T5 (D) M10T3

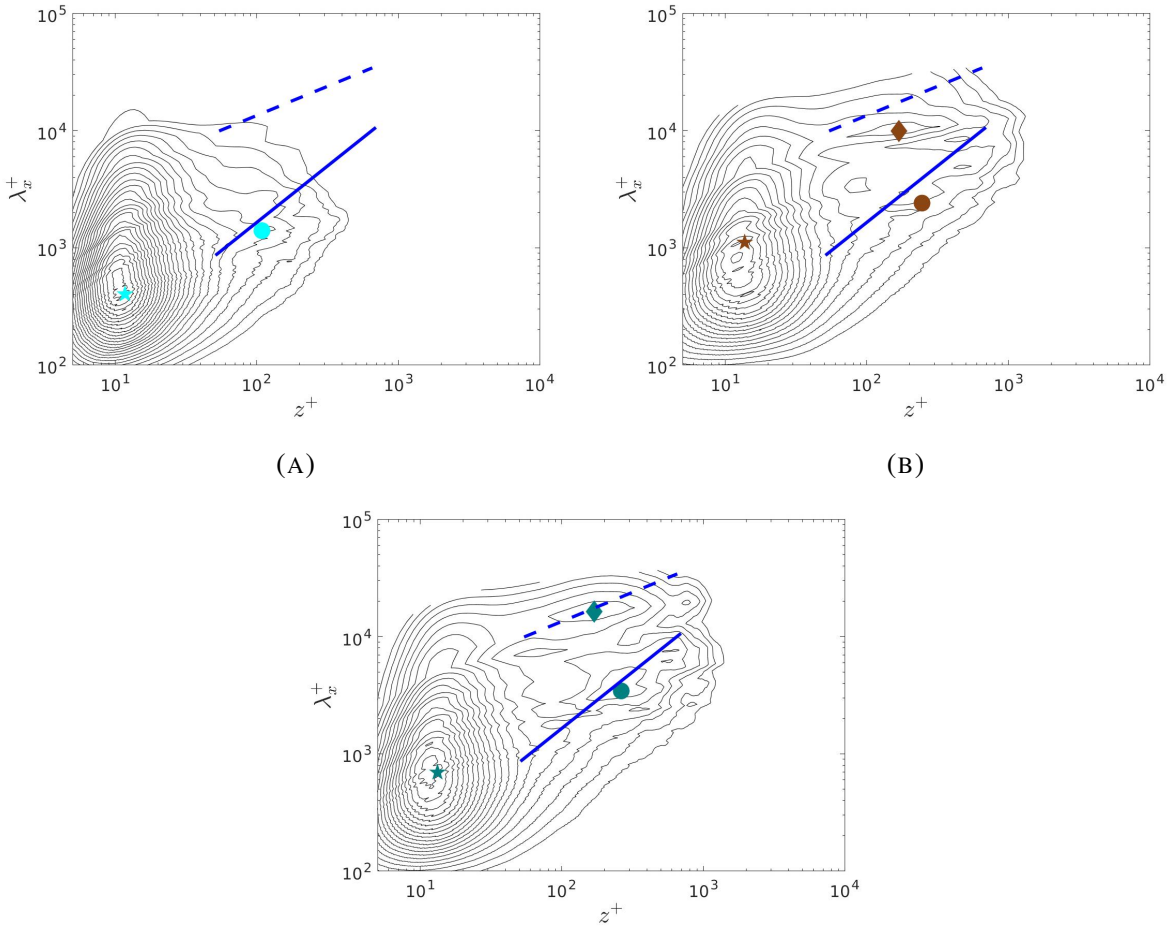

(A) (B)

(C)

FIGURE B.4. Pre-multiplied energy spectra based on $\rho u'' u''/\tau_w$ velocity signal plotted against wall normal position, z, in x-axis and streamwise wavelength, λ_x, in y-axis. Wall normal position and wavelength are normalized by the viscous length scale. (A) M12T5 (B) M2H (C) M6H

Appendix C: Parametric Study on Cut-off Length Scale

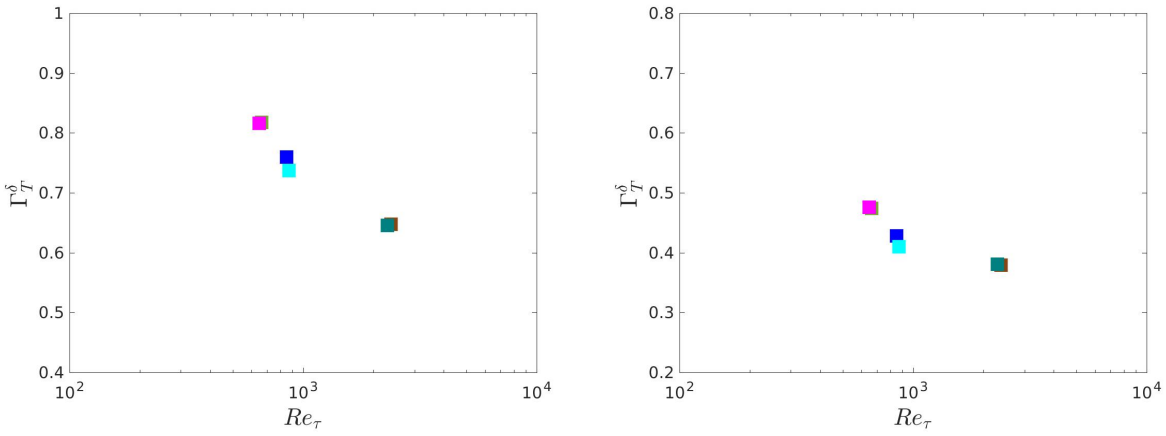

(A) (B)

FIGURE C.1. Relative contribution of large turbulent structures using wavelength cut-off based on outer scaling at (A) $\lambda_x/\delta = 0.5$ (B)$\lambda_x/\delta = 2.0$

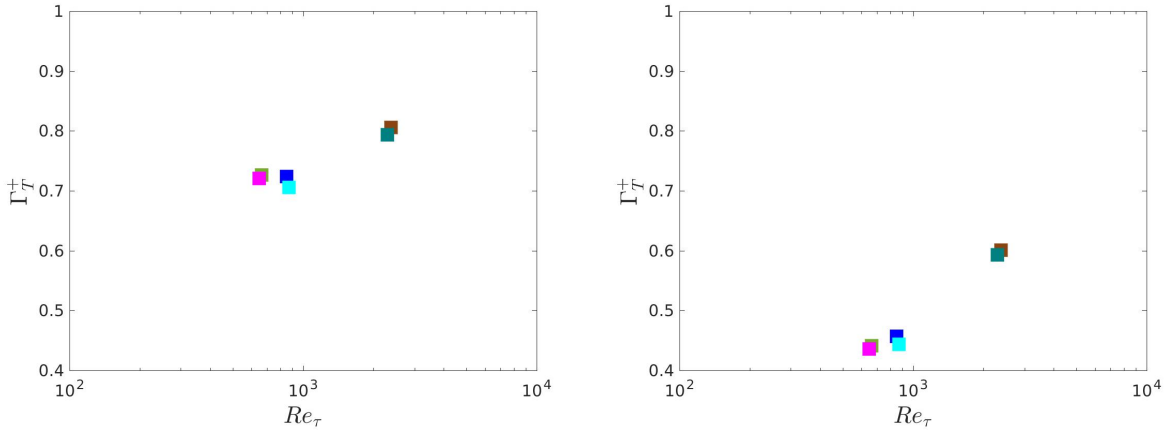

(A) (B)

FIGURE C.2. Relative contribution of large turbulent structures using wavelength cut-off based on outer scaling at (A) $\lambda_x^+ = 500$ (B) $\lambda_x^+ = 1500$

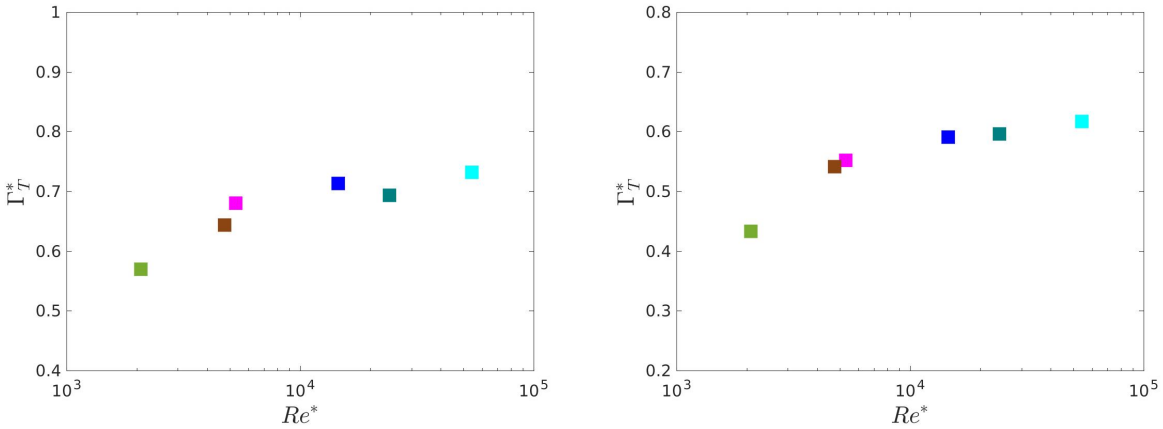

(A) (B)

FIGURE C.3. Relative contribution of large turbulent structures using wavelength cut-off based on outer scaling at (A) λ_x^* = 1500 (B) λ_x^* = 2500

Bibliography

[1] Han Lee, Clara Helm, Pino Martin, and Owen Williams. Compressible boundary layer velocity transformation based on a generalized form of the total stress. *Physics Review Fluids*, 2023.

[2] Michele Cogo, Francesco Salvadore, Francesco Picano, and Matteo Bernardini. Direct numerical simulation of supersonic and hypersonic turbulent boundary layers at moderate-high reynolds numbers and isothermal wall condition. *Journal of Fluid Mechanics*, 945:A30, 2022.

[3] You-Sheng Zhang, Wei-Tao Bi, Fazle Hussain, and Zhen-Su She. A generalized reynolds analogy for compressible wall-bounded turbulent flows. *Journal of Fluid Mechanics*, 739:392–420, 2014.

[4] Kevin Patrick Griffin, Lin Fu, and Parviz Moin. Velocity transformation for compressible wall-bounded turbulent flows with and without heat transfer. *Proceedings of the National Academy of Sciences*, 118(34), 2021.

[5] A. E. Perry and M. S. Chong. On the mechanism of wall turbulence. *Journal of Fluid Mechanics*, 119:173–217, 1982.

[6] A. E. Perry, S. Henbest, and M. S. Chong. A theoretical and experimental study of wall turbulence. *Journal of Fluid Mechanics*, 165:163–199, 1986.

[7] K. C. Kim and R. J. Adrian. Very large-scale motion in the outer layer. *Physics of Fluids*, 11(2):417–422, 1999.

[8] SK Robinson. The kinematics of turbulent boundary layer structure. Technical report, NASA Technical Memorandum, 1991.

[9] M. P. Martín, E. M. Taylor, M. Wu, and V. G. Weirs. A bandwidth-optimized WENO scheme for the effective direct numerical simulation of compressible turbulence. *Journal of Computational Physics*, 220(1):270–289, 2006.

[10] Alexander J. Smits and Jean Paul Dussauge. *Turbulent shear layers in supersonic flow: Second edition*. Springer New York, United States, 2006.

[11] P Bradshaw. Compressible turbulent shear layers. *Annual Review of Fluid Mechanics*, 9(1):33–52, 1977.

[12] E. R. Van Driest. Turbulent boundary layer in compressible fluid. *J. Aeronaut. Sci.*, 18:145—-216, 1951.

[13] Andrew Trettel and Johan Larsson. Mean velocity scaling for compressible wall turbulence with heat transfer. *Physics of Fluids*, 28(2):026102, 2016.

[14] L. CROCCO. Sulla trasmissione del calore da una lamina piana a un fluido scorrente ad alta velocita. *L Aerotecnica*, 18:181–197, 1932.

[15] A BUSEMANN. Handbuch der experimentalphysi. *Geest und Portig*, 4.

[16] J. Gaviglio. Reynolds analogies and experimental study of heat transfer in the supersonic boundary layer. *International Journal of Heat and Mass Transfer*, 30(5):911–926, 1987.

[17] P. Huang, Gary Coleman, and P. Bradshaw. Compressible turbulent channel flows: Dns results and modelling. *Journal of Fluid Mechanics*, 305, 12 1995.

[18] A. Walz and H.J. Oser. *Boundary Layers of Flow and Temperature*. M.I.T. Press, 1969.

[19] A.A. Townsend. *The Structure of Turbulent Shear Flow*. Cambridge University Press, 1976.

[20] MATTHEW J. RINGUETTE, MINWEI WU, and M. PINO MARTÍN. Coherent structures in direct numerical simulation of turbulent boundary layers at mach 3. *Journal of Fluid Mechanics*, 594:59–69, 2008.

[21] Matthew Bross, Sven Scharnowski, and Christian J. Kähler. Large-scale coherent structures in compressible turbulent boundary layers. *Journal of Fluid Mechanics*, 911:A2, 2021.

[22] L. DUAN, I. BEEKMAN, and M. P. MARTÍN. Direct numerical simulation of hypersonic turbulent boundary layers. part 3. effect of mach number. *Journal of Fluid Mechanics*, 672:245–267, 2011.

[23] Jie Yao and Fazle Hussain. Turbulence statistics and coherent structures in compressible channel flow. *Phys. Rev. Fluids*, 5:084603, Aug 2020.

[24] Junji Huang, Lian Duan, and Meelan M. Choudhari. Direct numerical simulation of hypersonic turbulent boundary layers: effect of spatial evolution and reynolds number. *Journal of Fluid Mechanics*, 937:A3, 2022.

[25] C. Mockett, M. Fuchs, and F. Thiele. Progress in des for wall-modelled les of complex internal flows. *Computers & Fluids*, 65:44–55, 2012. Sixth International Conference on Computational Fluid Dynamics (ICCFD6).

[26] Johan Larsson, Soshi Kawai, Julien Bodart, and Ivan Bermejo-Moreno. Large eddy simulation with modeled wall-stress: Recent progress and future directions. *Mechanical Engineering Reviews*, 3, 11 2015.

[27] Sanjeeb T. Bose and George Ilhwan Park. Wall-modeled large-eddy simulation for complex turbulent flows. *Annual Review of Fluid Mechanics*, 50(1):535–561, 2018.

[28] Owen J. H. Williams, Dipankar Sahoo, Mark L. Baumgartner, and Alexander J. Smits. Experiments on the structure and scaling of hypersonic turbulent boundary layers. *Journal of Fluid Mechanics*, 834:237–270, 2018.

[29] N. R. Tichenor, R. A. Humble, and R. D. W. Bowersox. Response of a hypersonic turbulent boundary layer to favourable pressure gradients. *Journal of Fluid Mechanics*, 722:187–213, 2013.

[30] Robert M. Latin and Rodney D. W. Bowersox. Flow properties of a supersonic turbulent boundary layer with wall roughness. *AIAA Journal*, 38(10):1804–1821, 2000.

[31] H. FOYSI, S. SARKAR, and R. FRIEDRICH. Compressibility effects and turbulence scalings in supersonic channel flow. *Journal of Fluid Mechanics*, 509:207–216, 2004.

[32] E F Spina, A J Smits, and S K Robinson. The physics of supersonic turbulent boundary layers. *Annual Review of Fluid Mechanics*, 26(1):287–319, 1994.

[33] M. W. RUBESIN. Extra compressibility terms for favre-averaged two-equation models of inhomogeneous turbulent flow. Technical report, NASA STI/Recon Tech, 1990.

[34] PETROVAN BOIARCIUC. M. BRUN. C. Large eddy simulation of compressible channel flo. *Theor. Comput. Fluid Dyn*, 22:189–212., 2008.

[35] You-Sheng Zhang, Wei-Tao Bi, Fazle Hussain, Xin-Liang Li, and Zhen-Su She. Mach-number-invariant mean-velocity profile of compressible turbulent boundary layers. *Phys. Rev. Lett.*, 109:054502, Jul 2012.

[36] Helmut Eckelmann. The structure of the viscous sublayer and the adjacent wall region in a turbulent channel flow. *Journal of Fluid Mechanics*, 65(3):439–459, 1974.

[37] C.B. Millikan and Guggenheim Aeronautical Laboratory. *A Critical Discussion of Turbulent Flows in Channels and Circular Tubes*. GALCIT/P-114. Guggenheim Aeronautical Laboratory, 1938.

[38] Christophe Brun, Margareta Boiarciuc, Marie Haberkorn, and Pierre Comte. Large eddy simulation of compressible channel flow. arguments in favour of universality of compressible turbulent wall bounded flows. *Theoretical and Computational Fluid Dynamics*, 22, 05 2008.

[39] Bin Wu, Weitao Bi, Fazle Hussain, and Zhen-Su She. On the invariant mean velocity profile for compressible turbulent boundary layers. *Journal of Turbulence*, 18(2):186–202, 2017.

[40] Ashish Patel, Bendiks J. Boersma, and Rene Pecnik. The influence of near-wall density and viscosity gradients on turbulence in channel flows. *Journal of Fluid Mechanics*, 809:793–820, 2016.

[41] STEPHEN E. GUARINI, ROBERT D. MOSER, KARIM SHARIFF, and ALAN WRAY. Direct numerical simulation of a supersonic turbulent boundary layer at mach 2.5. *Journal of Fluid Mechanics*, 414:1–33, 2000.

[42] M. Lagha, J. Kim, J. D. Eldredge, and X. Zhong. A numerical study of compressible turbulent boundary layers. *Physics of Fluids*, 23(1):015106, 2011.

[43] S. Pirozzoli, F. Grasso, and T. B. Gatski. Direct numerical simulation and analysis of a spatially evolving supersonic turbulent boundary layer at m=2.25. *Physics of Fluids*, 16(3):530–545, 2004.

[44] G. N. Coleman, J. Kim, and R. D. Moser. A numerical study of turbulent supersonic isothermal-wall channel flow. *Journal of Fluid Mechanics*, 305:159–183, 1995.

[45] Chao Zhang, Lian Duan, and Meelan M. Choudhari. Direct numerical simulation database for supersonic and hypersonic turbulent boundary layers. *AIAA Journal*, 56(11):4297–4311, 2018.

[46] Davide Modesti and Sergio Pirozzoli. Reynolds and mach number effects in compressible turbulent channel flow. *International Journal of Heat and Fluid Flow*, 59:33–49, 2016.

[47] M. Hultmark, M. Vallikivi, S. C. C. Bailey, and A. J. Smits. Turbulent pipe flow at extreme reynolds numbers. *Phys. Rev. Lett.*, 108:094501, Feb 2012.

[48] M. Hultmark, M. Vallikivi, S. C. C. Bailey, and A. J. Smits. Logarithmic scaling of turbulence in smooth- and rough-wall pipe flow. *Journal of Fluid Mechanics*, 728:376–395, 2013.

[49] M. Vallikivi, M. Hultmark, and A. J. Smits. Turbulent boundary layer statistics at very high reynolds number. *Journal of Fluid Mechanics*, 779:371–389, 2015.

[50] Henry Ng, Jason Monty, N. Hutchins, Megan Chong, and I. Marusic. Comparison of turbulent channel and pipe flows with varying reynolds number. *Experiments in Fluids*, 51:1261–1281, 11 2011.

[51] JAVIER JIMÉNEZ and SERGIO HOYAS. Turbulent fluctuations above the buffer layer of wall-bounded flows. *Journal of Fluid Mechanics*, 611:215–236, 2008.

[52] Myoungkyu Lee and Robert D. Moser. Direct numerical simulation of turbulent channel flow up to $Re_\tau \approx 5200$. *Journal of Fluid Mechanics*, 774:395–415, 2015.

[53] H. L. Grant, R. W. Stewart, and A. Moilliet. Turbulence spectra from a tidal channel. *Journal of Fluid Mechanics*, 12(2):241–268, 1962.

[54] T. B. Nickels, I. Marusic, S. Hafez, and M. S. Chong. Evidence of the k_1^{-1} law in a high-reynolds-number turbulent boundary layer. *Phys. Rev. Lett.*, 95:074501, Aug 2005.

[55] Ulf Högström, Julian Charles Roland Hunt, and Ann Sofi Smedman. Theory and measurements for turbulence spectra and variances in the atmospheric neutral surface layer. *Boundary-Layer Meteorology*, 103:101–124, 2002.

[56] T Theodorsen. Mechanism of turbulence. In *Proceedings of the 2nd Midwestern Conference on Fluid Mechanics*, pages 1–19, 1952.

[57] Spina E.F. *Organized structures in a supersonic turbulent boundary layer*. PhD thesis, Princeton University, 1988.

[58] S. J. Kline, W. C. Reynolds, F. A. Schraub, and P. W. Runstadler. The structure of turbulent boundary layers. *Journal of Fluid Mechanics*, 30(4):741–773, 1967.

[59] Jr. Bakewell, Henry P. and John L. Lumley. Viscous Sublayer and Adjacent Wall Region in Turbulent Pipe Flow. *The Physics of Fluids*, 10(9):1880–1889, 09 1967.

[60] M. R. Head and P. Bandyopadhyay. New aspects of turbulent boundary-layer structure. *Journal of Fluid Mechanics*, 107:297–338, 1981.

[61] JAVIER JIMÉNEZ and ALFREDO PINELLI. The autonomous cycle of near-wall turbulence. *Journal of Fluid Mechanics*, 389:335–359, 1999.

[62] R. J. ADRIAN, C. D. MEINHART, and C. D. TOMKINS. Vortex organization in the outer region of the turbulent boundary layer. *Journal of Fluid Mechanics*, 422:1–54, 2000.

[63] SERGIO PIROZZOLI, MATTEO BERNARDINI, and FRANCESCO GRASSO. Characterization of coherent vortical structures in a supersonic turbulent boundary layer. *Journal of Fluid Mechanics*, 613:205–231, 2008.

[64] Carl D. Meinhart and Ronald J. Adrian. On the existence of uniform momentum zones in a turbulent boundary layer. *Physics of Fluids*, 7(4):694–696, 1995.

[65] S. S. Lu and W. W. Willmarth. Measurements of the structure of the reynolds stress in a turbulent boundary layer. *Journal of Fluid Mechanics*, 60(3):481–511, 1973.

[66] W. W. Willmarth and S. S. Lu. Structure of the reynolds stress near the wall. *Journal of Fluid Mechanics*, 55(1):65–92, 1972.

[67] R. F. Blackwelder and R. E. Kaplan. On the wall structure of the turbulent boundary layer. *Journal of Fluid Mechanics*, 76(1):89–112, 1976.

[68] C. D. TOMKINS and R. J. ADRIAN. Spanwise structure and scale growth in turbulent boundary layers. *Journal of Fluid Mechanics*, 490:37–74, 2003.

[69] J. ZHOU, R. J. ADRIAN, S. BALACHANDAR, and T. M. KENDALL. Mechanisms for generating coherent packets of hairpin vortices in channel flow. *Journal of Fluid Mechanics*, 387:353–396, 1999.

[70] R. Baidya, J. Philip, N. Hutchins, J. P. Monty, and I. Marusic. Distance-from-the-wall scaling of turbulent motions in wall-bounded flows. *Physics of Fluids*, 29(2), 02 2017. 020712.

[71] M. GUALA, S. E. HOMMEMA, and R. J. ADRIAN. Large-scale and very-large-scale motions in turbulent pipe flow. *Journal of Fluid Mechanics*, 554:521–542, 2006.

[72] Nicholas Hutchins and Ivan Marusic. Large-scale influences in near-wall turbulence. *Philosophical Transactions of the Royal Society A: Mathematical, Physical and Engineering Sciences*, 365(1852):647–664, 2007.

[73] N. HUTCHINS and IVAN MARUSIC. Evidence of very long meandering features in the logarithmic region of turbulent boundary layers. *Journal of Fluid Mechanics*, 579:1–28, 2007.

[74] J. P. MONTY, J. A. STEWART, R. C. WILLIAMS, and M. S. CHONG. Large-scale features in turbulent pipe and channel flows. *Journal of Fluid Mechanics*, 589:147–156, 2007.

[75] B. J. Rosenberg, M. Hultmark, M. Vallikivi, S. C. C. Bailey, and A. J. Smits. Turbulence spectra in smooth- and rough-wall pipe flow at extreme reynolds numbers. *Journal of Fluid Mechanics*, 731:46–63, 2013.

[76] M. Vallikivi, M. Hultmark, and A. J. Smits. Turbulent boundary layer statistics at very high reynolds number. *Journal of Fluid Mechanics*, 779:371–389, 2015.

[77] B. GANAPATHISUBRAMANI, N. T. CLEMENS, and D. S. DOLLING. Large-scale motions in a supersonic turbulent boundary layer. *Journal of Fluid Mechanics*, 556:271–282, 2006.

[78] L. DUAN, I. BEEKMAN, and M. P. MARTÍN. Direct numerical simulation of hypersonic turbulent boundary layers. part 3. effect of mach number. *Journal of Fluid Mechanics*, 672:245–267, 2011.

[79] Ellen M. Taylor, Minwei Wu, and M. Pino Martín. Optimization of nonlinear error for weighted essentially non-oscillatory methods in direct numerical simulations of compressible turbulence. *J. Comput. Phys.*, 223(1):384–397, April 2007.

[80] M.P. Martín, E.M. Taylor, M. Wu, and V.G. Weirs. A bandwidth-optimized weno scheme for the effective direct numerical simulation of compressible turbulence. *Journal of Computational Physics*, 220(1):270–289, 2006.

[81] J.H Williamson. Low-storage runge-kutta schemes. *Journal of Computational Physics*, 35(1):48–56, 1980.

[82] William Sutherland. Lii. the viscosity of gases and molecular force. *The London, Edinburgh, and Dublin Philosophical Magazine and Journal of Science*, 36(223):507–531, 1893.

[83] Guang-Shan Jiang and Chi-Wang Shu. Efficient implementation of weighted eno schemes. *Journal of Computational Physics*, 126(1):202–228, 1996.

[84] Joseph L Steger and R.F Warming. Flux vector splitting of the inviscid gasdynamic equations with application to finite-difference methods. *Journal of Computational Physics*, 40(2):263–293, 1981.

[85] P. Orlandi M. Bernardini, S. Pirozzoli. Velocity statistics in turbulent channel flow up to retau=4000. *Journal of Fluid Mechanics*, 742:171–191, March 2014.

[86] M. MARTIN. Direct numerical simulation of hypersonic turbulent boundary layers. part 1. initialization and comparison with experiments. *Journal of Fluid Mechanics*, 570:347 – 364, 01 2007.

[87] Sheng Xu and M. Pino Martin. Assessment of inflow boundary conditions for compressible turbulent boundary layers. *Physics of Fluids*, 16(7):2623–2639, 2004.

[88] L. Duan and M. Martín. Direct numerical simulation of hypersonic turbulent boundary layers. part 4. effect of high enthalpy. *Journal of Fluid Mechanics*, 684:25 – 59, 10 2011.

[89] L. Duan, I. Beekman, and M. P. Martín. Direct numerical simulation of hypersonic turbulent boundary layers. part 2. effect of wall temperature. *Journal of Fluid Mechanics*, 655:419–445, 2010.

[90] Ashish Patel, Jurriaan W. R. Peeters, Bendiks J. Boersma, and Rene Pecnik. Semi-local scaling and turbulence modulation in variable property turbulent channel flows. *Physics of Fluids*, 27(9):095101, 2015.

[91] Tianyi Bai, Kevin P. Griffin, and Lin Fu. Compressible velocity transformations for various noncanonical wall-bounded turbulent flows. *AIAA Journal*, 0(0):1–13, 0.

[92] L. Prandtl. Bericht über untersuchungen zur ausgebildeten turbulenz. *Z. Angew. Math. Mech.*, 5:136–139, 1925.

[93] Lian Duan, Meelan M. Choudhari, and Chao Zhang. Pressure fluctuations induced by a hypersonic turbulent boundary layer. *Journal of Fluid Mechanics*, 804:578–607, 2016.

[94] Ming Yu, Chun-Xiao Xu, and Sergio Pirozzoli. Genuine compressibility effects in wall-bounded turbulence. *PHYSICAL REVIEW FLUIDS*, 4(12), DEC 5 2019.

[95] Hassan M. Nagib and Kapil A. Chauhan. Variations of von kármán coefficient in canonical flows. *Physics of Fluids*, 20(10):101518, 2008.

[96] David B. de Graaff and John K. Eaton. Reynolds-number scaling of the flat-plate turbulent boundary layer. *Journal of Fluid Mechanics*, 422(1):319–346, November 2000.

[97] Christian E. Willert, Julio Soria, Michel Stanislas, Joachim Klinner, Omid Amili, Michael Eisfelder, Christophe Cuvier, Gabriele Bellani, Tommaso Fiorini, Alessandro Talamelli, and et al. Near-wall statistics of a turbulent pipe flow at shear reynolds numbers up to 40 000. *Journal of Fluid Mechanics*, 826:R5, 2017.

[98] M. Samie, I. Marusic, N. Hutchins, M. K. Fu, Y. Fan, M. Hultmark, and A. J. Smits. Fully resolved measurements of turbulent boundary layer flows up to retau = 20000. *Journal of Fluid Mechanics*, 851:391–415, 2018.

[99] Romain Mathis, Nicholas Hutchins, and Ivan Marusic. Large-scale amplitude modulation of the small-scale structures in turbulent boundary layers. *Journal of Fluid Mechanics*, 628:311–337, 2009.

[100] B.J Balakumar and R.J Adrian. Large- and very-large-scale motions in channel and boundary-layer flows. *Philosophical Transactions of the Royal Society A: Mathematical, Physical and Engineering Sciences*, 365(1852):665–681, 2007.

[101] Garry L. Brown and Andrew S. W. Thomas. Large structure in a turbulent boundary layer. *The Physics of Fluids*, 20(10):S243–S252, 10 1977.

[102] Romain Mathis, Nicholas Hutchins, and Ivan Marusic. A predictive inner–outer model for streamwise turbulence statistics in wall-bounded flows. *Journal of Fluid Mechanics*, 681:537–566, 2011.

[103] Lionel Agostini and Michael Leschziner. Predicting the response of small-scale near-wall turbulence to large-scale outer motions. *Physics of Fluids*, 28(1):015107, 01 2016.

[104] Cheng Cheng and Lin Fu. Large-scale motions and self-similar structures in compressible turbulent channel flows. *Phys. Rev. Fluids*, 7:114604, Nov 2022.

[105] Bharathram Ganapathisubramani, Ellen K. Longmire, and Ivan Marusic. Characteristics of vortex packets in turbulent boundary layers. *Journal of Fluid Mechanics*, 478:35–46, 2003.

[106] Owen Williams, Clara Helm, Han Lee, and Pino Martin. Influences of outer layer friction reynolds number on near-wall hypersonic boundary layer turbulence. *In Preparation*.

[107] M. Vallikivi, B. Ganapathisubramani, and A. J. Smits. Spectral scaling in boundary layers and pipes at very high reynolds numbers. *Journal of Fluid Mechanics*, 771:303–326, 2015.

[108] Ivan Marusic and Jason P. Monty. Attached eddy model of wall turbulence. *Annual Review of Fluid Mechanics*, 51(1):49–74, 2019.

[109] I. Marusic, R. Mathis, and N. Hutchins. Predictive model for wall-bounded turbulent flow. *Science*, 329(5988):193–196, 2010.

[110] Martin Wosnik, Luciano Castillo, and Wialliam K. George. A theory for turbulent pipe and channel flows. *Journal of Fluid Mechanics*, 421:115–145, 2000.

[111] T. Wei, P. Fife, J. Klewicki, and P. McMurtry. Properties of the mean momentum balance in turbulent boundary layer, pipe and channel flows. *Journal of Fluid Mechanics*, 522:303–327, 2005.